SEPARATION AND COLLECTIVE PHENOMENA OF COLLOIDAL PARTICLES IN BROWNIAN RATCHETS

ANDREJ GRIMM

NATIONAL UNIVERSITY OF SINGAPORE

2010

SEPARATION AND COLLECTIVE PHENOMENA OF COLLOIDAL PARTICLES IN BROWNIAN RATCHETS

ANDREJ GRIMM

(Diplom Physiker, University of Konstanz)

A THESIS SUBMITTED

FOR THE DEGREE OF DOCTOR OF PHILOSOPHY

DEPARTMENT OF PHYSICS

NATIONAL UNIVERSITY OF SINGAPORE

2010

Acknowledgements

For supervising my graduate studies, I thank Prof. Johan R.C. van der Maarel. In his group, he generates an academic environment that allowed me to follow my research ideas freely while receiving his valuable advice.

For his continuous support, I thank Prof. Holger Stark from the Technical University of Berlin. During my various visits at his group, I have enormously benefitted from the discussions with him and his students.

For our productive collaboration, I thank Oliver Gräser from the Chinese University of Hong Kong. Our frequent mutual visits were memorable combinations of science and leisure.

For initiating the experimental realization of the proposed microfluidic devices proposed in this thesis, I thank Simon Verleger from University of Konstanz. I further thank Tan Huei Ming and Prof. Jeroen A. van Kan from NUS for supporting the experiments with high-quality channel prototypes.

For their support in various administrative issues during my research stays overseas, I thank Binu Kundukad an Ng Siow Yee. In particular, I thank Dai Liang for supporting me during the submission process.

Contents

Summary

In this thesis, we introduce novel mechanisms for the separation of colloidal particles based on the ratchet effect. It is further demonstrated that hydrodynamic interactions among colloidal particles are able to enhance the ratchet effect and cause interesting collective phenomena. The research has been done by means of theoretical modeling and numerical simulations. The thesis can be divided into three projects.

In the first project, we propose a ratchet-based separation mechanism that results in microfluidic devices with significantly reduced size. For this purpose, we introduce a ratchet model that switches cyclically between two distinct ratchet potentials and a zero-potential state. The applied potentials are chosen such that Brownian particles exhibit reversal of the direction of their mean displacement when relevant parameters such as the on-time of the potentials are varied. This direction reversal offers us new opportunities for the design of microfluidic separation devices. Based on the results of our ratchet model, we propose two new separation mechanisms. Compared to the conventional microfluidic devices, the proposed devices can be made of significantly smaller sizes without sacrificing the resolution of the separation process. In fact, one of our devices can be reduced to a single channel. We study our ratchet model by Brownian dynamics simulations and derive analytical and approximative

expressions for the mean displacement. We show that these expressions are valid in relevant regions of the parameter space and that they can be used to predict the occurrence of direction reversal. Furthermore, the separation dynamics in the proposed channel device are investigated by means of Brownian dynamics simulations.

In the second project, we introduce a mechanism that facilitates efficient ratchet-based separation of colloidal particles in pressure-driven flows. Here, the particles are driven through a periodic array of obstacles by a pressure gradient. We propose an obstacle design that breaks the symmetry of fluid flows and therefore fulfills the crucial requirement for ratchet-based particle separation. The proposed mechanism allows a fraction of the flow to penetrate the obstacles, while the immersed particles are sterically excluded. Based on Lattice-Boltzmann simulations of the fluid flow, it is demonstrated that this approach results in highly asymmetrical flow pattern. The key characteristics of the separation process are estimated by means of Brownian ratchet theory and validated with Brownian dynamics simulations. For the efficient simulation of fluid flows we introduce novel boundary conditions for the Lattice-Boltzmann method exploiting the full periodicity of the array.

In the third project, we investigate how hydrodynamic interactions between Brownian particles influence the performance of a fluctuating ratchet. For this purpose, we perform Brownian dynamics simulations of particles that move in a toroidal trap under the influence of a sawtooth potential which fluctuates between two states (on and off). We first consider spatially constant transition rates between the two ratchet states and observe that hydrodynamic interactions significantly increase the mean velocity of the particles but only when they are allowed to change their ratchet states individually. If in addition the

transition rate to the off state is localized at the minimum of the ratchet potential, particles form characteristic transient clusters that travel with remarkably high velocities. The clusters form since drifting particles have the ability to push but also pull neighboring particles due to hydrodynamic interactions.

List of Publications

- A. Grimm and H. Stark, *Hydrodynamic interactions enhance the performance of Brownian ratchets*, Soft Matter **7** (2011), 3219

- A. Grimm and O. Gräser, *Obstacle design for pressure-driven vector chromatography in microfluidic devices*, Europhysics Letters **92** (2010), 24001

- O. Gräser and A. Grimm, *Adaptive generalized periodic boundary conditions for lattice Boltzmann simulations of pressure-driven flows through confined repetitive geometries*, Physical Review E **82** (2010), 16702

- A. Grimm, H. Stark and J.R.C. van der Maarel, *Model for a Brownian ratchet with improved characteristics for particle separation*, Physical Review E **79** (2009), 61102

List of Figures

List of Tables

Chapter 1

Introduction

Transport phenomena of colloidal particles in Brownian ratchets are the central topic of this thesis. Brownian ratchets are systems far from equilibrium with broken spatial symmetry. In such a system, the Brownian motion of colloidal particles is rectified such that directed transport occurs. Within the framework of Brownian ratchets, we address questions in the field of microfluidic particle separation and hydrodynamic interactions. To be precise, we introduce novel mechanisms for continuous separation of colloidal particles based on the ratchet effect. Further, we demonstrate that hydrodynamic interactions among colloidal particles are able to enhance the ratchet effect and cause interesting collective phenomena.

1.1 Brownian ratchets

The ratchet effect has attracted growing interest after it has been discussed by Feynman in his famous mind experiment - Ratchet and pawl [42]. Here a rotational mechanical ratchet mechanism is connected through a belt to a

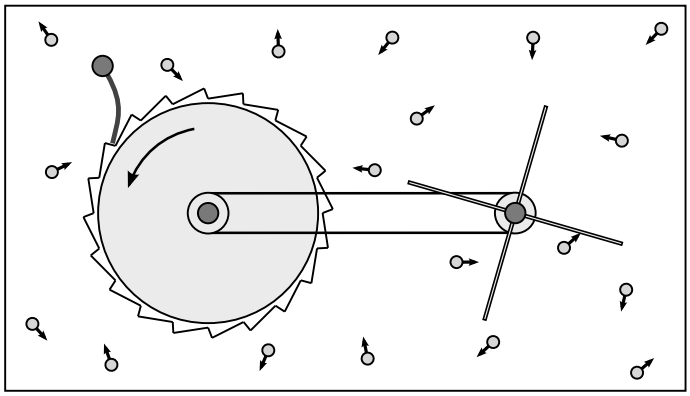

Figure 1.1: Schematic depiction of the device discussed in Feynman's mind experiment. A wheel with paddles is connected to a wheel with a sawtooth profile through a belt. An elastic pawl allows rotation in forward direction as indicated by the arrow, but prevents backward rotation. The whole device is surrounded by gas molecules moving with thermal velocities corresponding with a temperature T of the system.

wheel with paddles as depicted in Fig. 1.1. The ratchet mechanism consists of a wheel with a sawtooth profile and an elastic pawl. The pawl is installed such that it allows the wheel to rotate easily in one direction (forward) and blocks the other direction (backward). The whole device is surrounded by gas in thermal equilibrium at temperature T. The idea is that the gas molecules drive the wheel by random collisions with the paddles. The ratchet mechanism is supposed to rectify the resulting random rotations of the wheel. Given such rectification, the device could even rotate against an external load and perform work. Although the functioning of such device seems to be plausible, it breaks the second law of thermodynamics. The latter forbids the existence of periodically working machines driven only by cooling a *single* heat bath.

A subtle effect prevents the described ratchet to function as intended. In order to push the wheel over the next tooth of the profile, the pawl needs to be bent which requires a certain amount of energy ϵ. The probability that the

collisions at the paddle accumulate this amount of energy during a certain time is proportional to $\mathrm{e}^{-\epsilon/(k_\mathrm{B}T)}$. However, the pawl is also exposed to molecular collisions of the same strength and hence fluctuates randomly. The probability that the pawl is bent by collisions such that backward rotation is possible is also given by $\mathrm{e}^{-\epsilon/(k_\mathrm{B}T)}$. Eventually both processes balance and the intended rectification of the rotational motion is impeded.

Feynman describes how to overcome this issue. The surrounding heat bath needs to be split into two parts with distinct temperatures. One part contains the ratchet mechanism and is set to the temperature T_1 while the other part contains the paddles and is kept at T_2. This difference in the temperatures breaks the balance of the probabilities. For $T_1 < T_2$, the probability for the wheel being pushed forward by random collisions is larger than the probability for the pawl being bent by fluctuations; to be precise $\mathrm{e}^{-\epsilon/(k_\mathrm{B}T_2)} > \mathrm{e}^{-\epsilon/(k_\mathrm{B}T_1)}$. As a consequence, the device functions as intended and the wheel rotates in forward direction.[1] The second law of thermodynamics is not violated any longer, since two heat baths are required for the functioning of the device. By adding the second heat bath Feynman introduced the concept of Brownian ratchets, *i.e.*, devices that transform unbiased Brownian motion into directed motion.

It is crucial to the understanding of Brownian ratchets that the use of two heat baths with distinct temperatures results in a non-equlibrium system.[2] Further, the forward-bias of the ratchet mechanism imposes a spatial

[1] If the temperature of the pawl is higher than the temperature of the wheel, the device will rotate in backward direction. In this case the pawl is not able to prevent backward rotation. It rather drives the wheel in backward direction by elastic force each time it reaches the top of a tooth after a fluctuation.

[2] Due to dissipation at the ratchet mechanism, continuous supply of energy is required to maintain the desired temperature difference between both heat baths. Note that dissipation is crucial, in order to avoid oscillations of the pawl.

asymmetry to the system. The new understanding that both features, non-equilibrium and asymmetry, are necessary to rectify Brownian motion can be considered as the merits of Feynman's mind experiment.

Three decades after Feynman's discussion, the first quantitative ratchet models have been introduced independently by Ajdari *et al.* [2, 3] and Magnasco *et al.* [88]. Here, a sawtooth potential is switched on and off periodically and stochastically, respectively. It is the switching that drives the system far from equilibrium, while the sawtooth potential provides the spatial asymmetry. In the proposed systems, Brownian motion is rectified such that the particles travel with non-zero mean velocities towards a direction that is defined by the asymmetry of the potential.

These articles initiated an avalanche of further ratchet models, which can be distinguished mainly by the particular way of breaking the spatial symmetry or driving the system out of equilibrium [4, 6, 17, 75, 101, 107]. It turned out that quantitative prediction of the mean velocity for a given ratchet system is far from trivial. In most cases, numerical methods are required, as only few limiting cases have analytical solutions. Not only the magnitude, even the direction of the induced mean velocity can be difficult to predict and might change several times while varying a single system parameter. The investigation of such direction reversal attracted a lot of interest within the community [9, 15, 18, 72]. Successively, a vast number of further aspects and extensions have been investigated leading to remarkable diversity within the field of ratchet systems. Those models include for example ratchets with spatially dependent friction coefficients [26], inertial effects [62], internal degrees of freedom [63], and active Brownian particles [117]. One branch of studies focussed on collective effects among groups of particles. It has been shown

that coupling among particles has significant effect on the magnitude as well as the direction of the induced mean velocities [1, 21, 25, 28, 30, 55, 69]. In recent studies, feedback controlled ratchet systems gained considerable interest [13, 41, 40]. Here, the ratchet potential is a function of the spatial configuration of the particles. It was demonstrated that the induced mean velocities can be significantly enhanced by certain feedback mechanisms.

Soon after the first ratchet models were introduced, the ratchet effect was demonstrated experimentally by Rousselet *et al.* [109]. In this experiment, colloidal particles were subjected to a spatially asymmetric and periodic a.c. electric field, which was cyclically switched on and off. The field was generated by interdigitated electrodes. Directed motion of the particles was observed in agreement with the predictions of ratchet theory. Further demonstrations of the ratchet effect used colloidal particles in linear and planar optical tweezer setups [39]. The direction reversal effect has been demonstrated experimentally for the first time in such a setup [79, 80].

Already in the early contributions the enormous implication of ratchet theory on the description of molecular motors has been recognized [4, 60, 101]. Molecular motors, *e.g.*, kinesin proteins carrying cargo along tubulin filaments within cells, perform reliably work in an environment with significant thermal fluctuations. Hence, their functioning has to vary significantly from macroscopic motors, which run in strict periodic cycles. Various ratchet models have been introduced to explain the principle mechanism of molecular motors [84]. Those models usually neglect the complexity of the proteins and focus on the question how chemical energy can be transformed into directional motion through the ratchet effect [83, 118]. Within the field of molecular motors the investigation of collective effects has established as a prominent branch.

Such collective behavior is particularly interesting, as *in vivo* molecular motors act in groups. Various coupling schemes, ranging from harmonically coupled dimers to groups of particles connected to a backbone, have been studied in this context [7, 10, 60, 61]. Traffic effects of large numbers of motors along the filaments have been studied with coarse-grained lattice models, revealing non-equilibrium phase transitions among several phases of traffic modes [14, 70, 68, 95].

1.2 Ratchet-based separation of micron-sized particles

In the early theoretical studies on Brownian ratchets, it already became apparent that one promising application is the separation of particles in microfluidic devices. The reason is that the motion of micron-sized particles is strongly influenced by thermal fluctuations. In this context it becomes an intriguing feature of the ratchet effect that diffusion is a requirement to the process rather than a hindrance.

The first designs that were proposed for this purpose were periodic arrays of asymmetric obstacles [36, 38]. In such a device the particles to be separated are driven through the device by an external force, *e.g.*, an electrophoretic force. Each time the particles pass a row of obstacles the ratchet effect induces a mean displacement in the direction perpendicular to the external force. Due to this displacement the mean trajectory of the particles is inclined to the direction of the external force. Distinct types of particles with different properties such as their radii have different inclination angles. This eventually leads to a separation of the particles. Compared to conventional

technologies, like gel electrophoresis, such devices offer some advantages. For example they can be operated in continuous mode. Once installed, the separated particles can be collected continuously at different outputs. In contrast, conventional separation devices run in batch mode. First they need to be loaded, and after the separation process the particles need to be extracted from the device either at different locations or at different times. Continuous separation allows ratchet-based devices to be used within integrated microfluidic devices denoted as "lab-on-a-chip", which promise new levels of efficiency and convenience to researchers in the biological sciences by automating many laborious experimental procedures [98].

A device for ratchet-based particle separation was realized by Chou *et al.* [19]. In their experiment they separated two types of DNA in a microfabricated array of asymmetric obstacles. The two types of DNA with distinct numbers of base pairs were driven by an electrophoretic force. It was observed that different types of DNA travel with distinct inclination angles through the device. Although this result demonstrates the applicability of the concept of the Brownian ratchet to the problem of particle separation, there were significant quantitative deviations between the experimental results and the theoretical predictions. The deviations made apparent that a complete theoretical understanding of the process was not achieved and that the early ratchet model had to be extended for specific separation scenarios. It was pointed out by Austin *et al.* [5], that the used ratchet model only holds if the external force is homogenous and unperturbed by the presence of the obstacles. Deviations from that assumption lead to a reduced efficiency of the separation process and hence smaller inclination angles. If the obstacles are completely impermeable for the external field, the separation process will be inhibited. Li *et*

al. [82] confirmed this effect by thorough numerical studies. It was further shown by Huang *et al.* [54] that particles can be separated even for completely impermeable obstacles if their size is similar to the width of the gap between the obstacles. Such finite-size effects have been neglected previously as particles have been assumed to be point-like in their interaction with the obstacles. Still a comprehensive theory providing quantitative predictions for the effect of impermeable obstacles on the separation process is missing.

A similar ratchet-based separation device has been realized by van Oudenaarden *et al.* [115]. In their work, phospholipids with distinct size were successfully separated. Again, the particles were driven by an electrophoretic force through an array of asymmetric obstacles. In contrast to the experiment by Chou *et al.* [19], the particles were not immersed in an aqueous solution but rather moved within an lipid bilayer.[3] A quantitative comparison of the results with the predictions of ratchet theory is difficult, because of the additional effects of the lipid bilayer.

Another approach, denoted as drift ratchet, has been followed by Kettner *et al.* [64] and Matthias *et al.* [92]. They use a microfabricated macroporous silicon membrane containing a huge number of etched parallel pores, which feature periodic and asymmetric cross-sections. The suspension is pumped back and forth with no net bias through such a membrane. Due to a subtle ratchet effect, the immersed particles move with certain mean velocities through the pores.[4] Further, the direction of the observed mean velocities depends on the

[3] A small fraction of the phospholipids were labeled with a fluorescent dye such that their motion could be captured by fluorescence microscopy. It is also the dye that added a net charge to the phospholipids and therefore enabled electrophoresis.

[4] The required spatial asymmetry arises from two effects. First, the particles undergo diffusion among flow layers with distinct velocities. This diffusion in combination with the asymmetric cross-section of the pores breaks the symmetry. Second the particles are reflected asymmetrically from the walls of the pore. Both processes depend crucially on the

particle size. This size dependence allows the separation of a suspension with two distinct particle types across the membrane. It is an intriguing feature of this approach that it can be parallelized massively resulting in a significantly increased throughput.

1.3 Hydrodynamic interactions in colloidal systems

Hydrodynamic interactions are ubiquitous in colloidal systems, as particles moving in a viscous fluid induce a flow field that affects other particles in their motion [49, 66, 31]. Since many ratchet systems have been realized in the colloidal domain, it is surprising that only two numerical studies addressed the question to what extent hydrodynamic interactions influence the performance of ratchet systems. In the first study, hydrodynamic coupling was included in the asymmetric simple exclusion process (ASEP) as a model for the dynamics of Brownian motors [51]. In the second study, hydrodynamic interactions were taken into account in Brownian dynamics simulations of a harmonically coupled dimer in a ratchet potential [43]. Both studies reported increased mean velocities of the Brownian motors and dimers, respectively, due to hydrodynamic coupling. However, the mechanism causing the enhanced velocities has not been studied in detail.

In contrast, the effect of hydrodynamic interactions on colloidal systems in general has been investigated in great detail. In this sense, early experimental and theoretical studies mostly investigated macroscopic rheological or transport properties of colloidal suspensions, where hydrodynamic interactions only

size of the particle.

appear in ensemble averages over the complete configuration space [96]. Recent advances in experimental techniques such as video microscopy and optical tweezers [46] have made it possible to monitor and manipulate single particles.

In order to systematically investigate the role of hydrodynamic coupling, studies were performed on the diffusion of an isolated pair of particles or the correlated thermal fluctuations of two colloidal beads held at a fixed distance by an optical tweezer [22, 94, 104, 90]. Several interesting collective phenomena were identified that originate from the long-range nature of hydrodynamic interactions. For instance, they give rise to periodic or almost periodic motions or even transient chaotic dynamics in sedimenting clusters of a few spherical particles [12, 111, 59]. Hydrodynamic interactions also lead to pattern formation through self-assembly of rotating collodial motors or in arrays of microfluidic rotors [47, 81, 113]. Synchronization induced by hydrodynamic interactions is particulary important in microbiology. Metachronal waves occur in arrays of short filaments that cover, for example, a paramecium. In order to shed light on the origin of these waves, synchronization in model systems consisting of a few particles was studied [76, 116, 97, 73]. Rotating helices such as bacterial flagella but also eukaryotic flagella synchronize through hydrodynamic interactions [65, 105, 45] and even microscopic swimmers are hydrodynamically coupled [58, 99].

Toroidal trap setups have proven to be useful for investigating hydrodynamic interactions among a limited number of particles [103, 87]. The toroidal trap is realized by means of a circling optical-tweezer that forces particles to move along a circle. For a cluster of particles, each driven by a constant force, theory has demonstrated highly non-linear drafting behavior [103] which was then observed in experiments [87]. Modulating the laser intensity during one

cycle, one can apply additional tangential driving forces to the particles so that a tilted sawtooth potential results. Here, hydrodynamic interactions help the particles to leave the local minima of the potential and thereby create caterpillar-like motion patterns. As a result, the particle cluster moves with a significantly increased mean velocity compared to a single particle in the same potential [87].

1.4 Outline

In chapter 2, the theoretical background of colloidal dynamics and Brownian ratchets is introduced. Starting from the hydrodynamics of a single sphere, we derive the relevant time scales and subsequently specify the hydrodynamic regime by means of the dimensionless Reynolds number. Based on the Langevin equation, we discuss the Brownian motion of colloidal particles. In particular, we show that diffusion in periodic potentials is not able to cause net transport of particles. This directly leads us to the so-called on-off ratchet model in which a periodic sawtooth potential is switched on and off cyclically. We show that in such a ratchet system directed transport occurs and derive a calculation scheme for the induced mean velocity. Subsequently, we introduce the concept of ratchet-based particle separation and map the separation process onto the on-off ratchet model. Eventually the Langevin equation is extended to three dimensions, incorporating the Rotne-Prager approximation for hydrodynamic interactions among the particles. Furthermore, a numerical integration scheme is introduced.

In chapter 3, a novel ratchet-based mechanism for microfluidic particle separation is proposed. The major advantage of the mechanism is that it allows

the reduction of the device to a single channel. The proposed device exploits the direction reversal effect, such that particles to be separated move towards opposite directions along the channel. For derivation of the separation mechanism we introduce an extension of the on-off ratchet that features direction reversal and subsequently translate the model parameters into design parameters of the device. Further we demonstrate by means of Brownian dynamic simulations that particle separation in the proposed channel design is feasible.

In chapter 4, a novel design for pressure-driven vector chromatography is proposed. Based on Lattice-Boltzmann simulations of the fluid flow through an periodic array of obstacles we demonstrate that conventional solid obstacles are not able to break the symmetry of the flow field. As a result, particle separation is not possible in arrays of conventional obstacles. We overcome this problem by making the obstacle partially permeable to the fluid flow. Subsequently, we map the dynamics of the separation process onto the on-off ratchet model. By means of Brownian dynamic simulations we demonstrate that the proposed obstacle design facilitates pressure-driven vector-chromatography and validate the predictions of ratchet theory.

In chapter 5, we investigate the effect of hydrodynamic interactions on the dynamics of colloidal particles in fluctuating ratchets by means of numerical simulations. It is shown that the ratchet effect is significantly enhanced under certain conditions. Further, the spontaneous formation of transient clusters travelling with remarkable velocities is observed. We explain how such cluster formation is induced by hydrodynamic coupling.

Chapter 2

Concepts, theoretical background and simulation methods

2.1 Colloidal particles and their environment

Colloidal particles are the main agents of this thesis. Before we introduce the theoretical methods to describe their motion, we briefly discuss some of their properties and specify the characteristics of the colloidal systems that we will investigate in the following chapters.

2.1.1 Properties of colloidal particles

Colloids are solid particles that are usually suspended in a solvent. They are mainly defined by their size. Although there is no exact definition for the size of colloidal particles, a rough range can be derived from two physical assumptions. First, a colloidal particle should be sufficiently large, such that

many solvent molecules interact simultaneously with the surface of the particle. Hence, the size of the particle has to be few orders of magnitude larger than the size of the solvent molecules. A particle size of about 10 nm gives a reasonable lower bound for most solvents. Second, thermal motion should significantly affect the dynamics of the particle. This requirement limits the particle size to a maximum of about 10 μm.

The two most widely used colloids are latex and amorphous silica particles which are available in a wide range of sizes. Latex particles consist of polymethylmethacrylate (PMMA) chains. Those chains form compact rigid spheres in water, which is a poor solvent for PMMA.[1] Silica particles have a rigid amorphous core, while the surface is often chemically modified to influence the solubility of the particles. The mass density of those particles is roughly 5% heavier than water. As a consequence, they are prone to sedimentation. Particles significantly larger than the estimated upper bound of 10 μm would sink to the bottom and remain very close to it. Smaller particles undergo stronger thermal fluctuations and can hence also be found at some distance to the bottom.

Next to size and mass density, the interaction among the particles needs to be specified. Two forces that are always present are the attractive van der Waals force and the repulsive hard-core interaction. Van der Waals forces are caused by the interaction of permanent or induced electric dipole moments. Due to their attractive nature, van der Waals forces cause aggregation of particles and therefore destabilize colloidal solutions. Since van der Waals forces are relatively short-ranged (r^{-6}) they can be masked by longer ranged repulsive

[1] For colloids based on polymer chains, the solvent significantly affects the shape. For example PMMA particles in a good solvent, like benzene, swell to soft and deformable spheres.

forces. Silica particles in water, for example, are relatively insensitive to van der Waals interactions, since they are surrounded by a 3 nm thick structured layer of water molecules. The repulsive hard-core interaction is caused by the enormous increase in energy when two particles overlap. For a pair of spherical particles, the corresponding potential is zero if the inter-particle distance is more than the sum both radii and virtually infinite for smaller distances [31].

For colloidal particles that carry an electrical charge, electrostatic interaction becomes relevant. Due to the presence of free ions and counterions in the solvent, the pair-interaction potential between charged colloids is not of the $1/r$ Coulomb form, but is screened to some extent by the formation of the so-called double-layer. For moderate potential energies and long distances, the screened Coulomb potential is given by the Yukawa potential of the form $\sim \exp(-\kappa r)/r$ with κ being the screening length. The latter is strongly influenced by the amount of free ions. As a consequence, the significance of the electrostatic interaction among the particles can experimentally be tuned by the addition of salt [114].

Besides the potential interactions, there is another type of interaction which is unique to colloidal systems. As colloidal particles move, they induce fluid flow in the solvent. This induced flow affects the motion of other colloidal particles. This effect is denoted as hydrodynamic interactions or hydrodynamic coupling. The character of this interaction is long-ranged and highly nonlinear. Hydrodynamic interactions will be discussed in detail in Sec. 2.5.

According to our definition, DNA molecules can also be considered as colloidal particles to some extent, as they form random coils in solution. The typical radius of the DNA coils depends on the number of base pairs (bp) and

the buffer conditions.[2] The DNA of λ-phage with 48.5 kbp, for example, has a typical radius of approximately $0.1\mu\text{m} - 1\mu\text{m}$. Rather than forming rigid particles, DNA coils are elastic and deformable under most buffer conditions.

2.1.2 Hydrodynamics of a single sphere

In this section, we consider the flow induced by a translating sphere in order to specify the relevant time scales and the hydrodynamic regime of colloidal systems. As discussed in the previous chapter, a colloidal particle is several orders of magnitude larger than the molecules of the solvent. We therefore consider the solvent as a continuous fluid with mass density ρ and viscosity η. The colloidal particle are treated as a boundary condition for the fluid. The flow field $\boldsymbol{u}(\boldsymbol{r}, t)$ of an incompressible fluid is governed by the well-known Navier-Stokes equation

$$\rho \left(\frac{\partial}{\partial t} + \boldsymbol{u} \cdot \nabla \right) \boldsymbol{u} = \eta \nabla^2 \boldsymbol{u} - \nabla p + \boldsymbol{f}_{\text{ext}} \tag{2.1}$$

and the incompressibility condition

$$\nabla \cdot \boldsymbol{u} = 0, \tag{2.2}$$

given a sufficient definition of the boundary conditions [31]. The terms $\boldsymbol{f}_{\text{ext}}$ and ∇p refer to the external force density acting on the fluid and the pressure gradient, respectively. In the following, bold symbols will indicate three-

[2] The radius of gyration strongly depends on the ion concentration since, screened electrostatic interactions strongly influence the statistics of the configuration. Low concentrations result in more swollen coils, as electrostatic repulsion among segments of the DNA molecule increases. Higher concentrations, in contrast, lead to more compact coils. Above a critical concentration, the loose coil collapses to a dense globule. [114]

dimensional vectors.

We consider a spherical particle with radius $\sigma = 1\,\mu\text{m}$ translating with velocity $v = 1\,\mu\text{m/s}$ in water with viscosity $\eta = 10^{-3}\,\text{Pa s}$. The particle radius and the velocity are used to introduce the rescaled variables $\bar{\boldsymbol{r}} = \boldsymbol{r}/\sigma$ and $\bar{\boldsymbol{u}} = \boldsymbol{u}/v$. Further we introduce a time-scale τ to rescale the time variable $\bar{t} = t/\tau$. Using the rescaled variables in Eq. 2.1 we obtain the dimensionless Navier-Stokes equation

$$\frac{\rho\sigma^2}{\eta\tau}\frac{\partial}{\partial\bar{t}}\bar{\boldsymbol{u}} + \text{Re}\,\bar{\boldsymbol{u}}\cdot\bar{\nabla}\bar{\boldsymbol{u}} = \bar{\nabla}^2\bar{\boldsymbol{u}} - \bar{\nabla}\bar{p} + \bar{\boldsymbol{f}}_{\text{ext}}, \tag{2.3}$$

with the rescaled pressure $\bar{p} = p/(\eta v/\sigma)$ and the rescaled force $\bar{\boldsymbol{f}} = \boldsymbol{f}/(\eta v/\sigma^2)$. The dimensionless factor Re is the Reynolds number which is defined as [31]

$$\text{Re} = \frac{\rho\, v\, \sigma}{\eta}. \tag{2.4}$$

The Reynolds number determines the hydrodynamic regime of the system, as it measures the ratio between inertial and viscous forces. For our translating particle, the Reynolds number is $\text{Re} \approx 10^{-6}$. As a consequence, the non-linear convection term $\boldsymbol{u}\cdot\nabla\boldsymbol{u}$ in the Navier-Stokes equation can be neglected, and we obtain the linear equation

$$\frac{\rho\sigma^2}{\eta\tau}\frac{\partial}{\partial\bar{t}}\bar{\boldsymbol{u}} = \bar{\nabla}^2\bar{\boldsymbol{u}} - \bar{\nabla}\bar{p} + \bar{\boldsymbol{f}}_{\text{ext}}. \tag{2.5}$$

Due to the linearity at low Reynolds numbers, the corresponding flows are laminar and no turbulence occurs. In contrast, a boat with a size of 10 m and a velocity of 1 m/s has a Reynolds number of $\text{Re} \approx 10^7$, which is in the non-linear, turbulent regime. This example makes clear that the hydrodynamic

regime is not solely determined by the viscosity of the fluid.

In order to determine the flow field around the translating sphere, the boundary conditions need to be specified. The fluid is unbound and at rest in infinity. On the surface of the particle, we apply the so-called stick-boundary condition

$$\boldsymbol{u}(\boldsymbol{r}) = \boldsymbol{v}, \quad \boldsymbol{r} \in \delta V, \tag{2.6}$$

with δV being the surface of the particle. For these boundary conditions the steady state solution of Eq. (2.5) is given by

$$\boldsymbol{u}(\boldsymbol{r}, t) = \boldsymbol{A}(\boldsymbol{r} - \boldsymbol{v}t) \cdot \boldsymbol{v}, \tag{2.7}$$

with

$$\boldsymbol{A}(\boldsymbol{r}) = \frac{3}{4}\frac{\sigma}{r}\left(\mathbf{1} + \hat{\boldsymbol{r}} \otimes \hat{\boldsymbol{r}}\right) + \frac{1}{4}\left(\frac{\sigma}{r}\right)^3 \left(\mathbf{1} - 3\,\hat{\boldsymbol{r}} \otimes \hat{\boldsymbol{r}}\right). \tag{2.8}$$

The integration of the stress tensor over the particles surface gives the force $\boldsymbol{F}$ that is required to balance the hydrodynamic drag and to drive the particle with a constant velocity $\boldsymbol{v}$ [77]. For the flow around a translating sphere in Eq. (2.8), the required force is proportional to the velocity

$$\boldsymbol{F} = \gamma\,\boldsymbol{v}. \tag{2.9}$$

The corresponding expression for the friction coefficient γ is given by the famous Stokes' law

$$\gamma = 6\pi\eta\sigma, \tag{2.10}$$

relating the friction coefficient of a spherical particle to its radius and the viscosity of the solvent. The inverse of the friction coefficient is the mobility

of a particle $\mu = 1/\gamma$, which relates the velocity of a particle to the driving force through $\boldsymbol{v} = \mu \boldsymbol{F}$.

Using Stokes' law, we can now specify the time τ_m for the particle to lose its momentum after the driving force $\boldsymbol{F}$ stops. Subsequently we compare the result to the previously unspecified time scale τ in Eq. (2.5). As soon as the force stops, the absolute value of the velocity v is governed by the following equation of motion

$$m\dot{v} + \gamma v = 0. \tag{2.11}$$

The solution of this differential equation is an exponential decay with the typical momentum relaxation time

$$\tau_\mathrm{m} = \frac{m}{\gamma}. \tag{2.12}$$

For the considered particle, the momentum decays approximately $0.1\,\mu$s after the force stops, *i.e.*, virtually instantaneously. Using the mass density of the particle $\rho_\mathrm{p} = 3m/(4\pi\sigma^3)$ in Eq. (2.5) we obtain

$$\frac{9}{2}\frac{\rho}{\rho_\mathrm{p}}\frac{\tau_\mathrm{m}}{\tau}\frac{\partial}{\partial \bar{t}}\,\bar{\boldsymbol{u}} = \bar{\nabla}^2\bar{\boldsymbol{u}} - \bar{\nabla}\bar{p} + \bar{\boldsymbol{f}}_\mathrm{ext}. \tag{2.13}$$

The mass density of fluid and particle are comparable. As a consequence, at low Reynolds numbers and on time scales $t > \tau_\mathrm{m}$ the inertial terms in Eq. (2.5) can be neglected. The resulting overdamped dynamics are hence fully described by the stationary Stokes equation

$$\eta\nabla^2\boldsymbol{u} - \nabla p + \boldsymbol{f}_\mathrm{ext} = 0, \tag{2.14}$$

and the incompressibility equation in Eq. (2.2).

For the colloidal systems discussed in this thesis, the overdamped Stokes equation (2.14) governs the fluid dynamics and is the stepping stone to the description of hydrodynamic interactions in Sec. 2.5. In the next section, we firstly consider the effect of thermal fluctuations on the dynamics of a single colloidal particle.

2.2 Brownian motion

Already in the 19th century it has been observed that suspended colloidal particles perform erratic motion. This phenomenon is caused by the interaction with the molecules of the surrounding fluid. Since the full time dependence of these interactions cannot be resolved experimentally, the resulting motion of the suspended particles seems to be random. The effect of the fluid on the particle can be described by a random force, keeping in mind that such a random force is the result of a vast number of collisions with fluid molecules.

2.2.1 Langevin equation

The Langevin equation is a stochastic description of Brownian motion. It can be considered as Newton's equation of motion including stochastic interactions with the molecules of the solvent. Thus, a frictional force $-\gamma\dot{x}$ and a fluctuating force $\xi(t)$ are added. The one-dimensional trajectory of a particle $x(t)$ is hence described by [110]

$$m\ddot{x}(t) = -\gamma\dot{x}(t) + \xi(t). \tag{2.15}$$

The random force is unbiased

$$\langle \xi(t) \rangle = 0. \tag{2.16}$$

The strength of the fluctuations in the random force $\xi(t)$ are not arbitrary. Since they are caused by interactions with the fluid molecules, they are dependent on the temperature T of the fluid. This is because the average velocity of the molecules and hence the strength of the collisions depend on the temperature. Furthermore, the random force must be related to the friction coefficient γ of the particle, because friction and random force have the same physical origin. The time-correlation of the random force therefore obeys the fluctuation-dissipation theorem

$$\langle \xi(t)\xi(t') \rangle = 2\gamma k_{\mathrm{B}} T \delta(t - t'), \tag{2.17}$$

with $k_{\mathrm{B}}T$ being the thermal energy. We will show in the following that the coefficient $2\gamma k_{\mathrm{B}}T$ is neccesary to fulfill the equipartion theorem for thermal equilibrium.

The Langevin equation is a stochastic differential equation. Any realization of the stochastic process $\xi(t)$ leads to unique particle trajectory $x(t)$ for a certain initial condition. In velocity space $\dot{x}(t) = v(t)$, the Langevin equation has the solution [110]

$$v(t) = v_0 e^{-\gamma t/m} + \frac{1}{m} \int_0^t dt' e^{-\gamma(t-t')/m} \xi(t'). \tag{2.18}$$

The first term of the right-hand side is due to the initial velocity v_0, which decays exponentially in agreement with the discussion about the momentum

relaxation in the previous section. The second term gives the contribution of the random force.

In thermal equilibrium, the equipartition theorem demands $\langle v^2 \rangle_{\mathrm{eq}} = k_{\mathrm{B}}T/m$. Hence the particle velocities have to obey

$$\lim_{t\to\infty} \langle v^2(t) \rangle = k_{\mathrm{B}}T/m. \tag{2.19}$$

Using Eq. (2.18), we get the following expression

$$\langle v^2(t) \rangle = \frac{e^{-2\gamma t}}{m^2} \int_0^t dt' \int_0^t dt'' e^{-\gamma(t'+t'')/m} \langle \xi(t')\xi(t'') \rangle, \tag{2.20}$$

where all mixed terms with the initial velocity contribution are ignored, due to their exponential decay. Using the correlation function of the random force defined in Eq. (2.17), the integral can be written as follows

$$\begin{aligned} \langle v^2(t) \rangle &= \frac{2\gamma k_{\mathrm{B}}T}{m^2}\, e^{-2\gamma t/m} \int_0^t dt' e^{-2\gamma t'/m} \\ &= \frac{k_{\mathrm{B}}T}{m} \left(1 - e^{-2\gamma t/m}\right). \end{aligned} \tag{2.21}$$

In the long time limit, this result resembles Eq. (2.19) and hence validates the chosen coefficient in the fluctuation-dissipation theorem in Eq. (2.17).

In order to investigate the diffusion of a particle, we consider its displacement during a certain time interval t, which is related to the velocity trajectory $v(t)$ as follows

$$\Delta x(t) = x(t) - x(0) = \int_0^t dt'\, v(t'). \tag{2.22}$$

Using Eqs. (2.16, 2.18), we derive that the mean displacement for a particle

with zero initial velocity is

$$\langle \Delta x(t) \rangle = 0. \tag{2.23}$$

In other words, the diffusion of the particle is unbiased. The mean square displacement, however, writes as

$$\begin{aligned} \langle (\Delta x(t))^2 \rangle &= 2 \int_0^t dt' (t - t')' \, \langle v(t') v(0) \rangle \\ &= \frac{2 m k_\mathrm{B} T}{\gamma^2} \left(e^{-\gamma t/m} - 1 + \frac{\gamma t}{m} \right). \end{aligned} \tag{2.24}$$

Here we used the velocity auto-correlation function

$$\langle v(t) v(t+\tau) \rangle = \frac{k_\mathrm{B} T}{m} \, e^{-\gamma \tau / m}, \tag{2.25}$$

which can be calculated from Eq. (2.18). The correlation time m/γ is equivalent to the typical momentum relaxation time τ_m in Eq. (2.12). For time lags $\tau \gg m/\gamma$, the velocity $v(t+\tau)$ is uncorrelated to the velocity $v(t)$ due to fluctuations and dissipation.

For the mean square displacement in Eq. (2.24), two regimes are demarcated by the correlation time scale. For $t \ll m/\gamma$, the expansion of the exponential term up to the second order gives the following expression for the mean square displacement

$$\langle (\Delta x(t))^2 \rangle = \frac{k_\mathrm{B} T}{m} \, t^2. \tag{2.26}$$

In this regime, the mean square displacement is independent on the friction coefficient γ. The particle can be considered to move freely with its thermal velocity. This regime is known as the ballistic regime. For $t \gg m/\gamma$, the mean

square displacement is given by

$$\langle(\Delta x(t))^2\rangle = \frac{2k_\mathrm{B}T}{\gamma}\,t = 2Dt, \tag{2.27}$$

which gives the famous Einstein relation for the diffusion constant

$$D = \frac{k_\mathrm{B}T}{\gamma}. \tag{2.28}$$

In this so-called diffusional regime, the diffusion of a Brownian particle features no mean displacement, but the mean square displacement increases linearly in time.

In this thesis we are interested in the dynamics of particles on time scales that are several orders of magnitude larger than the momentum relaxation time τ_m and the equivalent correlation time. The mean square displacement is hence described by the diffusion regime. Further, inertial effects are neglected and the motion of the particles can be described by the overdamped Langevin equation

$$\gamma\dot{x}(t) = \xi(t), \tag{2.29}$$

which is the stepping stone to most numerical methods in this thesis. Although we limited the discussion in this section to the case without external forces f_ext, such forces can simply be added

$$\gamma\dot{x}(t) = f_\mathrm{ext}(x,t) + \xi(t), \tag{2.30}$$

since they only cause additional terms in the previous discussion. In Sec. 2.5, the latter equation is extended to three dimensions and to many-particle

systems.

2.2.2 Smoluchowski equation

An alternative approach to diffusional motion is to consider the probability density $\mathcal{P}(x,t)$ to find a particle at a certain position x for the time t. The equation that governs the time evolution of $\mathcal{P}(x,t)$ can be derived from the overdamped Langevin equation (2.30) [110]. For that purpose we define the probability density as

$$\mathcal{P}(x,t) = \langle \delta(x - x(t)) \rangle. \tag{2.31}$$

Here we have to distinguish carefully between the position x and the trajectory $x(t)$. The average is taken over an ensemble of particle trajectories. For the time evolution we get the following expression

$$\begin{aligned} \frac{\partial}{\partial t}\mathcal{P}(x,t) &= -\frac{\partial}{\partial x}\langle \delta(x - x(t))\, \dot{x}(t) \rangle \\ &= -\frac{\partial}{\partial x}\langle \delta(x - x(t))\, \gamma^{-1}(f_{\text{ext}}(x,t) + \xi(t)) \rangle \\ &= -\gamma^{-1}\frac{\partial}{\partial x}\left[f_{\text{ext}}(x,t)\mathcal{P}(x,t)\right] - \gamma^{-1}\frac{\partial}{\partial x}\langle \delta(x - x(t))\, \xi(t) \rangle \end{aligned} \tag{2.32}$$

The overdamped Langevin equation (2.29) has been plugged in for $\dot{x}(t)$. For the ensemble average in the second term on the right-hand side, a thorough calculation reveals [110]

$$\langle \delta(x - x(t))\, \xi(t) \rangle = -k_{\text{B}}T\frac{\partial}{\partial x}\mathcal{P}(x,t). \tag{2.33}$$

Using the latter equation, the relation $\mu = 1/\gamma$ and the Einstein relation $D = k_{\mathrm{B}}T/\gamma$ in Eq. (2.32), we get the well-known Smoluchowski equation

$$\frac{\partial}{\partial t}\mathcal{P}(x,t) = -\frac{\partial}{\partial x}\left[\mu f_{\mathrm{ext}}(x,t)\,\mathcal{P}(x,t)\right] + D\,\frac{\partial^2}{\partial x^2}\mathcal{P}(x,t). \tag{2.34}$$

The Smoluchowski equation can be written in the form of a continuity equation

$$\frac{\partial}{\partial t}\mathcal{P}(x,t) = \frac{\partial}{\partial x}j(x,t), \tag{2.35}$$

with the probability density current

$$j(x,t) = \mu f_{\mathrm{ext}}(x,t)\,\mathcal{P}(x,t) + D\frac{\partial}{\partial x}\mathcal{P}(x,t). \tag{2.36}$$

Two contributions to the probability density current can be identified. The first term corresponds with a deterministic drift current caused by the external force. The second term corresponds with a diffusional current caused by gradients in the probability density function according to Fick's law.

With the introduction of the probability density $\mathcal{P}(x,t)$ we transformed the Langevin equation, a stochastic differential equation, to the Smoluchowski equation, a second-order partial differential equation. In contrast to the particle trajectories, the evolution of the probability density is not of stochastic nature.

2.2.3 Diffusion equation

For the special case with no external force, the Smoluchowski equation becomes the famous diffusion equation

$$\frac{\partial}{\partial t}\mathcal{P}(x,t) = D\,\frac{\partial^2}{\partial x^2}\mathcal{P}(x,t). \tag{2.37}$$

The diffusion equation can be written in dimensionless form by using rescaled variables. We therefore introduce the distance L as a length scale. The typical time for the particle to cover the distance L by diffusion t_{diff} gives a time scale. According to the mean square displacement in Eq. (2.27) the diffusion time t_{diff} is defined by

$$t_{\text{diff}} = \frac{L^2}{D}. \tag{2.38}$$

Using the rescaled position $\bar{x} = x/L$ and the rescaled time $\bar{t} = t/t_{\text{diff}}$ in Eq. (2.37) we get

$$\frac{\partial}{\partial \bar{t}}\mathcal{P}(\bar{x},\bar{t}) = \frac{\partial^2}{\partial \bar{x}^2}\mathcal{P}(\bar{x},\bar{t}). \tag{2.39}$$

For the initial condition $\mathcal{P}(\bar{x},\bar{t}=0) = \delta(\bar{x})$, *i.e.*, for a particle starting at $\bar{x} = 0$, the solution of the diffusion equation is

$$\mathcal{P}(\bar{x},\bar{t}) = \frac{1}{\sqrt{4\pi\,\bar{t}}}\,\exp\left(-\frac{\bar{x}^2}{4\bar{t}}\right). \tag{2.40}$$

This is a Gaussian bell function with a variance of $2\bar{t}$, which is in agreement with the mean square displacement of Brownian particles in Eq. (2.27). The probability density function has been plotted for three values of the rescaled time in Fig. 2.1. The distribution becomes wider as time elapses but the mean position remains unbiased with $\langle \Delta\bar{x} \rangle = 0$.

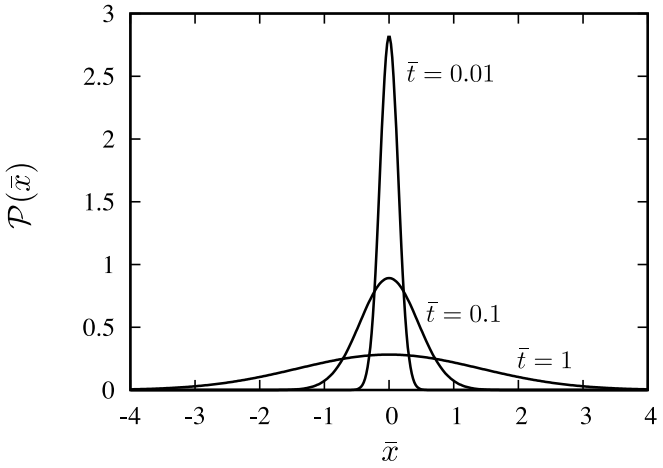

Figure 2.1: Probability density function $\mathcal{P}(x)$ as a function of the rescaled position $\bar{x}$ for three values of the rescaled times $\bar{t}$. The initial condition is $\mathcal{P}(\bar{x}, \bar{t} = 0) = \delta(\bar{x})$.

2.2.4 Diffusion in static periodic potentials

Based on the Smoluchowski equation we can discuss the diffusion in periodic potentials $V(x)$. The potential is related to the external force through $f_{\text{ext}} = -(\partial/\partial x)V(x)$. The spatial period is given by L such that $V(x) = V(x + L)$. For the stationary solution of the Smoluchowski equation (2.35) with $(\partial/\partial t)\mathcal{P}(x,t) = 0$, we get the condition

$$-\frac{\partial}{\partial x}\left[\mu\left(\frac{\partial}{\partial x}V(x)\right)\mathcal{P}(x,t)\right] = D\,\frac{\partial^2}{\partial x^2}\mathcal{P}(x,t). \tag{2.41}$$

In other words, the deterministic drift has to be balanced by the diffusion due to probability gradients. The solution is given by the Boltzmann distribution

$$\mathcal{P}_{\text{B}}(x) \sim \exp\left(-\frac{V(x)}{k_{\text{B}}T}\right), \tag{2.42}$$

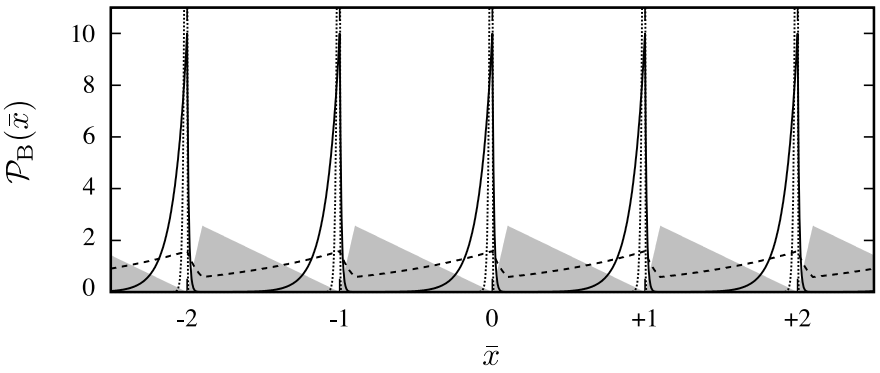

Figure 2.2: Boltzmann distribution $\mathcal{P}_{\mathrm{B}}(x)$ as a function of the rescaled position $\bar{x}$ for three different rescaled potential amplitudes $\bar{V} = V/(k_{\mathrm{B}}T)$: $\bar{V} = 1$ (dashed line), $\bar{V} = 10$ (solid line) and $\bar{V} = 100$ (dotted line). The distribution for $\bar{V} = 100$ is not fully shown. The underlying sawtooth potential has been added with arbitrary unit for its amplitude.

with the proportionality constant determined by normalization over a single period, such that $\int_0^L \mathrm{d}x\, \mathcal{P}_{\mathrm{B}}(x) = 1$. The probability density function $\mathcal{P}_{\mathrm{B}}(x)$ features the same periodicity as the potential. As an example we consider an asymmetric, piecewise linear sawtooth potential with the amplitude $\hat{V}$.[3] The corresponding probability density is depicted in Fig. 2.2 as a function of the rescaled position $\bar{x} = x/L$ for three different rescaled potential amplitudes $\bar{V} = V/(k_{\mathrm{B}}T)$. For larger values of $\bar{V}$, the distribution becomes more localized at the minima of the sawtooth potential. In the limiting case with $\bar{V} \to \infty$, the probability density becomes a sequence of delta-peaks $\mathcal{P}_{\mathrm{B}}(\bar{x}) = \delta(\bar{x})$ at the positions of the minima.

When the system reaches the Boltzmann distribution the probability current density vanishes

$$j(x) = 0, \tag{2.43}$$

which can be verified by using $\mathcal{P}_{\mathrm{B}}(x)$ in Eq. (2.36).[4] We are interested in the

[3] The sawtooth potential will be defined in Eq. (2.47).

[4] For non-periodic potentials, the probability density current $j(x)$ might not vanish for

mean velocity $\langle \dot{x} \rangle$ of a particle in the periodic potential. The latter is related to the probability current density through [106]

$$\langle \dot{x} \rangle = \int_{-\infty}^{\infty} \mathrm{d}x \, j(x,t). \tag{2.44}$$

Since the probability current vanishes in equilibrium, the mean velocity of a particle also vanishes

$$\langle \dot{x} \rangle = 0 \tag{2.45}$$

independent of the actual potential $V(x)$. This is an implication of the 2nd law of thermodynamics, which forbids any system to perform work only driven by a single heat bath.

2.3 Brownian ratchets

In the previous section, we have demonstrated that static periodic potentials are not able to induce directed motion to Brownian particles, even in the case of spatially asymmetric potentials. In this section, we will show how non-equilibrium perturbations induce non-zero mean velocities in Brownian ratchets. In the beginning, we discuss a well-known example for such perturbations. This example introduces the ratchet effect in an instructive way and is, at the same time, particularly relevant for this thesis. Later we discuss the general characteristics of Brownian ratchets and distinguish different types of ratchets.

the steady state solution. For example in a tilted sawtooth potential, a constant probability density current occurs in steady state.

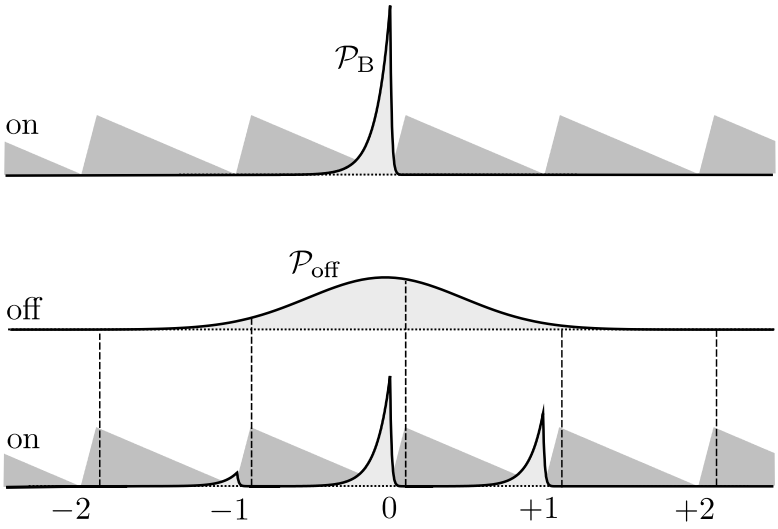

Figure 2.3: The rectification of Brownian motion due to non-equilibrium perturbation of an asymmetric, periodic potential. When the potential is switched off, the probability density function evolves from the Boltzmann distribution $\mathcal{P}_\mathrm{B}$ to a wider Gauss-like distribution $\mathcal{P}_\mathrm{off}$. When the potential is switched on again, a net probability flow to the right occurs due to the asymmetry of the potential.

2.3.1 The ratchet effect

We consider a single particle in an asymmetric sawtooth potential. Assume that the potential has been switched on for sufficient time so that the system reached equilibrium and the probability density function has relaxed to the corresponding Boltzmann distribution $\mathcal{P}_\mathrm{B}$, as defined in Eq. (2.42). The peak of that distribution is localized at the minimum of the potential.[5] In the next step, the potential is switched off and the particle diffuses freely. Due to the diffusion of the particle, the Boltzmann distribution will evolve into a wider distribution $\mathcal{P}_\mathrm{off}$. When the potential is switched on again, the probability

[5]Note that the mean position of the particle is shifted towards the middle of the period the weaker the potential is. For $V \ll k_\mathrm{B}T$, the asymmetry of the potential is effectively not sensed by the particle any longer. We hence consider the case with $V \gg k_\mathrm{B}T$, such that the mean position of the particle within a spatial period is significantly shifted towards the minimum of the potential.

density will again relax towards the Boltzmann distribution. A certain part of the probability density function will now relax to the neighboring minima. Here, the asymmetry of the potential has a crucial effect on the result, *i.e.*, the part that reaches the minimum to the right is larger than the part that reaches the minimum to the left. As consequence, a net probability flow to the right occurs. If this cycle is repeated continuously, the particle will move on average to the right such that

$$\langle \dot{x} \rangle > 0. \tag{2.46}$$

This is a remarkable result given that the average force due to the sawtooth potential vanishes with $\int_0^L \mathrm{d}x\, V(x) = 0$. By switching the potential on and off, a cyclic non-equilibrium perturbation has been applied to the potential. The described system is an example for a Brownian ratchet. If the switching of the sawtooth potential happens periodically, it is denoted as on-off ratchet.

2.3.2 The On-Off ratchet model

The on-off ratchet is a two state system: The off-state in which the particle diffuses freely, and the on-state in which the particle moves under the influence of the ratchet potential $V(x)$. The state of the ratchet potential switches periodically. For the times t_{on} and t_{off} the potential is in the on- and off state respectively. A complete cycle of the ratchet potential hence has the period $T = t_{\mathrm{on}} + t_{\mathrm{off}}$. The sawtooth potential $V(x)$ is characterized by a spatial period

L, asymmetry a, and amplitude $\hat{V}$

$$V(x) = \hat{V} \begin{cases} \frac{x}{aL} & \text{for } 0 < x \leq aL \\ 1 - \frac{x-aL}{(1-a)L} & \text{for } aL < x \leq L \end{cases}, \tag{2.47}$$

and periodicity is taken into account by $V(x) = V(x + L)$. The asymmetry parameter a determines the shape of the potential and has a value in the range from zero to one.

According to Eq. (2.30), the motion of a Brownian particle with a friction coefficient γ is described by the following overdamped Langevin equation

$$\gamma\, \dot{x} = -\frac{\partial}{\partial x}\, V(x,t) + \xi(t), \tag{2.48}$$

where x denotes the position of the particle at the time t. As discussed in Sec. 2.2.1, the random force $\xi(t)$ is unbiased, so that $\langle \xi(t) \rangle = 0$, and its time-correlation function obeys the fluctuation-dissipation theorem

$$\langle \xi(t)\xi(t') \rangle = 2\,\gamma\, k_{\mathrm{B}} T\, \delta(t - t'). \tag{2.49}$$

Dimensionless parameters

Writing the Langevin equation in dimensionless form reveals the relevant parameters of the system. The spatial period L provides a length scale, whereas the time t_{diff} in Eq. (2.38) gives a time scale. Another time scale is given by the drift time t_{drift}, which is the required time for the particle to drift the distance L under the constant force $\hat{V}/L$. With the drift velocity $v_{\mathrm{drift}} = \hat{V}/(\gamma\, L)$, the

drift time takes the following form

$$t_{\mathrm{drift}} = \frac{L}{v_{\mathrm{drift}}} = \frac{t_{\mathrm{diff}}}{\bar{V}}, \tag{2.50}$$

with the rescaled potential amplitude $\bar{V} = \hat{V}/(k_{\mathrm{B}}T)$. The Langevin Eq. (2.48) and the correlation function Eq. (2.49) can now be expressed in reduced form

$$\dot{\bar{x}} = \bar{V}\, f_a(\bar{x}, \bar{t}) + \bar{\xi}(\bar{t}), \tag{2.51}$$

$$\langle \bar{\xi}(\bar{t})\, \bar{\xi}(\bar{t}') \rangle = 2\, \bar{\delta}(\bar{t} - \bar{t}'), \tag{2.52}$$

where we have used the rescaled position $\bar{x} = x/L$, time $\bar{t} = t/t_{\mathrm{diff}}$, random force $\bar{\xi}(\bar{t}) = \xi(t)\, L/(k_{\mathrm{B}}T)$, and δ-function $\bar{\delta}(\bar{t}) = t_{\mathrm{diff}}\, \delta(t)$. The function f_a describes the rescaled force exerted on the Brownian particle. When the potential is switched off, $f_a = 0$ and Eq. (2.51) describes a particle freely diffusing in one dimension. When the ratchet potential is switched on, $f_a = -1/a$ and $f_a = 1/(1-a)$ on the long and short slopes of the potential, respectively. Note that the rescaled potential amplitude $\bar{V}$ is the Peclet number [31]. As shown by Eq. (2.50), it denotes the ratio of the times a particle needs to diffuse and drift a distance L. At large Peclet numbers drift is therefore dominant and Brownian diffusion during the on-time can be neglected.

We also rescale the periods of the ratchet cycle t_{on} and t_{off}. First, the off-time t_{off} is rescaled with respect to the diffusion time t_{diff},

$$\tau_{\mathrm{off}} = \frac{t_{\mathrm{off}}}{t_{\mathrm{diff}}}. \tag{2.53}$$

For $\tau_{\mathrm{off}} < 1$, Brownian particles are typically not able to cover a distance L by diffusion during the time t_{off}. Second, the on-time t_{on} is rescaled with respect

to the drift time t_{drift},

$$\tau_{\mathrm{on}} = \frac{t_{\mathrm{on}}}{t_{\mathrm{drift}}}. \tag{2.54}$$

For $\tau_{\mathrm{on}} > 1$, all particles will reach the minima of the potentials. In analogy with the rescaling of the time variable $\bar{t} = t/t_{\mathrm{diff}}$, we also obtain $\bar{t}_{\mathrm{on}} = \tau_{\mathrm{on}}/\bar{V}$ and the period

$$\bar{T} = \tau_{\mathrm{off}} + \tau_{\mathrm{on}}/\bar{V} \tag{2.55}$$

of one complete ratchet cycle. Note that for large Peclet numbers $\hat{V}$, the rescaled period is approximately given by $\bar{T} \approx \tau_{\mathrm{off}}$.

The motion of a Brownian particle in the on-off ratchet is fully determined by the rescaled off-time τ_{off}, the rescaled on-time τ_{on}, the asymmetry parameter a, and the Peclet number $\bar{V}$. For an arbitrary set of parameters, no analytical solution for the mean displacement exists. Numerical integration of the Langevin equation is therefore necessary in order to investigate the complete parameter space. However, in the limit of large Peclet numbers and sufficiently large values of τ_{on} analytic expressions are available.

The limit of discrete steps

To derive an analytic expression for the mean displacement $\langle \Delta\bar{x} \rangle$ in the case of large Peclet numbers $\bar{V}$, we apply the method of discrete steps [3]. This method is based on the assumption that the rescaled on-time τ_{on} and the Peclet number $\bar{V}$ are sufficiently large, so that a Brownian particle will always reach a minimum when the ratchet potential is switched on. Hence, the trajectory of the particle can be mapped onto a sequence of effective steps between the locations of the potential minima. These steps occur with certain step probabilities.

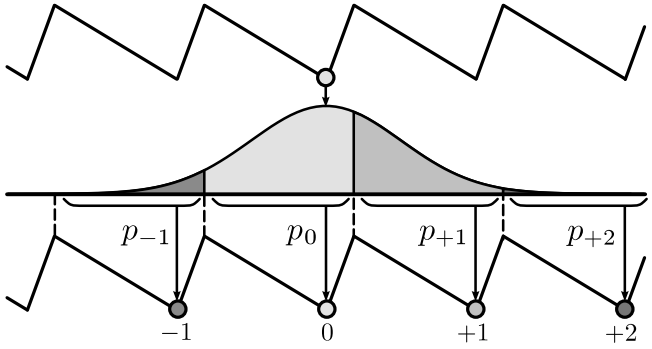

Figure 2.4: Schematic illustration of a complete cycle of the on-off ratchet in the discrete limit. The distinctly shaded parts of the probability density function $\mathcal{P}$ correspond with the step probabilities p_n for a particle to reach the minimum at $\bar{x} = n$ in the subsequent on-time.

For large Peclet numbers $\bar{V}$, Brownian motion can be neglected once the potential is switched on. As a result, a particle drifts uniformly towards a minimum. For the longer slope of the ratchet potential V, the drift velocity $v_{\text{drift}} = \hat{V}/[\gamma\,(1-a)L]$. Accordingly, the particle reaches the minimum for

$$t_{\text{on}} \geq \frac{(1-a)L}{v_{\text{drift}}} = (1-a)^2\, t_{\text{drift}}, \tag{2.56}$$

irrespective of its position at the time the potential is switched on. With the definition of the rescaled on-time τ_{on} in Eq. (2.54), the latter condition can be expressed as

$$\tau_{\text{on}} \geq (1-a)^2. \tag{2.57}$$

Particles drifting under the influence of the shorter slope also reach the minimum, provided Eq. (2.57) is satisfied. Accordingly, after each application of the potential, all particles are located at the minima of $V(x)$. A single particle hence performs discrete steps along the x-axis, provided its trajectory is sampled at the end of each on-time. The minima of potential V are labeled with the integer n , so that the corresponding positions are given by $\bar{x}_n = n$.

Now, we consider the probability p_n for a step performed by a single particle from the minimum 0 to the minimum n, as illustrated in Fig. 2.4. When the potential is switched off the particle diffuses freely, starting from $\bar{x} = 0$. According to Eq. (2.40), the probability density to reach the position $\bar{x}$ at the end of the off-time is given by

$$\mathcal{P}(\bar{x}) = \frac{1}{\sqrt{4\pi\tau_{\text{off}}}} \exp\left(-\frac{\bar{x}^2}{4\tau_{\text{off}}}\right). \tag{2.58}$$

Note that the width of this distribution is solely determined by the value of the rescaled off-time τ_{off}. In order to drift to the minimum n during the subsequent on-time, the particle needs to diffuse into the interval $n - 1 + a < \bar{x} < n + a$ situated between the neighboring maxima of minimum n. Accordingly, the step probability is given by integrating $\mathcal{P}(\bar{x})$, so that

$$p_n = \int_{n-1+a}^{n+a} \frac{d\bar{x}}{\sqrt{4\pi\tau_{\text{off}}}} \exp\left(-\frac{\bar{x}^2}{4\tau_{\text{off}}}\right). \tag{2.59}$$

The step probabilities are depicted in Fig. 2.5 (a) as a function of the rescaled off-time for $a = 0.2$. Due to the asymmetry of the sawtooth potential, the step probabilities are biased, such that $p_{+n} > p_{-n}$, for any value of τ_{off}.

The mean displacement $\langle \Delta\bar{x} \rangle$ is calculated by averaging over all possible steps

$$\langle \Delta\bar{x} \rangle = \langle n \rangle = \sum_n n \cdot p_n. \tag{2.60}$$

Note that in the discrete limit the mean displacement $\langle \Delta\bar{x} \rangle$ only depends on the values of the asymmetry parameter a and the rescaled off-time τ_{off}.

The mean displacement is depicted in Fig. 2.5 (b) as a function of the rescaled off-time for several values of a. For small values of τ_{off}, the mean

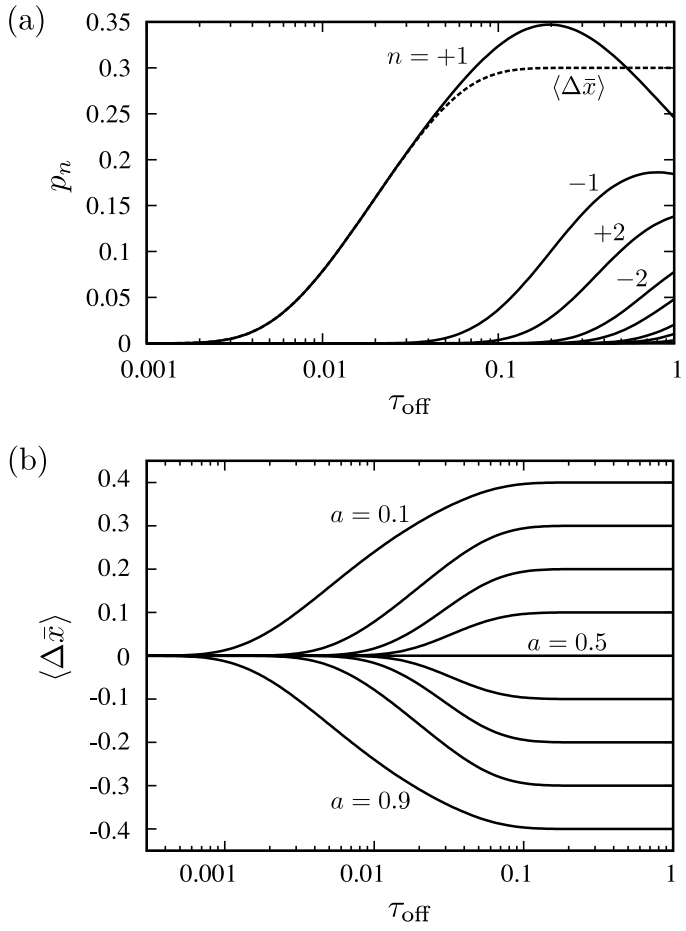

Figure 2.5: (a) Step probability p_n as a function of the rescaled off-time τ_{off} for $a = 0.2$. The corresponding mean displacement has been added for sake of comparison. (b) Mean displacement $\langle \Delta \bar{x} \rangle$ as a function of the rescaled off-time τ_{off} for nine asymmetry parameters a. The asymmetry parameters are in the range from 0.1 to 0.9 with increments of 0.1 between adjacent lines.

displacement vanish, because the step probabilities to neighboring minima become negligible. For large values of τ_{off}, the mean displacement approaches its maximum value $\langle \Delta \bar{x} \rangle_{\max}$. An algebraical expression for $\langle \Delta \bar{x} \rangle_{\max}$ can be derived on the basis that the probability profile between two maxima becomes approximately homogeneous for large values of τ_{off}. The fractions of the particles experiencing the longer and shorter slopes of the ratchet potential V are given by $(1-a)$ and a, respectively. The corresponding mean displacements of

these fractions are $(1-a)/2$ and $-a/2$. The total mean displacement is given by the weighed average of both fractions, so that

$$\langle \Delta \bar{x} \rangle = \frac{1}{2} - a. \tag{2.61}$$

It should be kept in mind that this expression is only valid for sufficiently large values of the rescaled on-time $\tau_{\text{on}} \geq (1-a)^2$.

In the on-off ratchet the direction of the induced mean displacement is solely determined by the asymmetry parameter a of the sawtooth potential. For $a < 1/2$, the mean displacement is in the positive direction along the x-axis, whereas for $a > 1/2$ the particle will move on average in the negative direction. A simple on-off ratchet with asymmetry $(1-a)$ induces exactly the opposite mean displacement as a ratchet with asymmetry a. In the symmetric situation with $a = 1/2$, no mean displacement will be observed.

Eventually, the mean velocity of the particle is related to the mean displacement through

$$\langle \dot{\bar{x}} \rangle = \langle \Delta \bar{x} \rangle / \bar{T}. \tag{2.62}$$

The mean velocity is depicted in Fig. 2.6 as a function of the rescaled off-time for several values of a. Smaller values of a lead to higher mean velocities, since the step probabilities ($p_{+n} > p_{-n}$) become more biased. Since the mean displacement $\langle \Delta \bar{x} \rangle$ reaches a maximum value for large values of τ_{off} and the cycle period $\bar{T}$ increases linearly with τ_{off}, the mean velocity has a maximum at a finite value for τ_{off}.

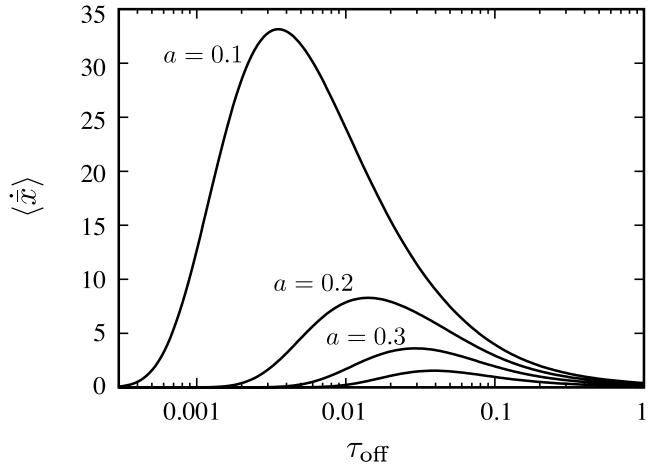

Figure 2.6: Mean velocity $\dot{\tilde{x}}$ as a function of the rescaled off-time τ_{off} for several asymmetry parameters a. The ratchet operates in the regime of discrete steps.

2.3.3 General definition of Brownian ratchets

With the on-off ratchet a non-equilibrium system has been introduced that is capable of rectifying Brownian motion. In general, Brownian ratchets have the following requirements:

1. The system has a spatial periodicity. This requirement facilitates continuous repetitions of the ratchet cycle. In the on-off ratchet, the sawtooth potential clearly features the required periodicity.

2. The averages of all external forces vanish over time and space. This requirement excludes the occurrence of trivial currents caused by non-vanishing forces. The applied sawtooth potential fulfills this requirement.

3. Fluctuations play a significant role in the motion of the particle. This requirement excludes mechanisms that work deterministically. For the functioning of the on-off ratchet, diffusion during the off-time is crucial and no mean velocity would occur for $T = 0$.

4. The symmetry of the system is broken. This requirement results in a directed response of the system to non-equilibrium perturbations. In the on-off ratchet, the sawtooth potential features a broken spatial inversion symmetry, which determines the direction of the induced mean velocity.

5. The system is driven out of equilibrium. This requirement is necessary to overcome the limitations due to the second law of thermodynamics and allows the system to perform work. In the on-off ratchet the periodic switching of the potential drives the system out of equilibrium.

The first three requirements have a rather technical character and are necessary to distinguish Brownian ratchets from similar mechanisms. The last two requirements address the fundamental functioning of each ratchet system. The vast number of ratchet models in literature can be categorized according to the way how those two requirements are fulfilled. Three major groups can be identified for the symmetry breaking. First, a ratchet potential with broken spatial symmetry can be applied [3, 88, 101]. Second, non-Gaussian fluctuations with non-vanishing odd moments cause the ratchet effect even in symmetric potentials [24, 86]. Third, spontaneous symmetry breaking can be caused by collective effects in non-eqilibrium systems [11, 61, 89, 108].

The applied non-equilibrium perturbations can also be categorized into three major groups. In the first group, the so-called pulsating ratchets, a multiplicative perturbation $\Theta(t)$ of the ratchet potential is used to drive the system out of equilibrium [9, 28, 101]. The corresponding Langevin equation for this ratchet type is given by

$$\gamma\,\dot{x}(t) = -\Theta(t)\,\frac{\partial}{\partial x}V(x) + \xi(t). \tag{2.63}$$

Note that the on-off ratchet belongs to this group, with the perturbation being incorporated in the time-dependent ratchet potential (see Sec. 2.3.2). In a recent branch of ratchet research, feedback-controlled ratchet systems are investigated [13, 41, 40]. Here, the perturbation $\Theta(\boldsymbol{x}, t)$ depends on the spatial configuration $\boldsymbol{x}$ of all particles.

In the second group, the so-called tilting or rocking ratchets, a perturbation $\Theta(t)$ enters the Langevin equation as an additional force term

$$\gamma\,\dot{x}(t) = -\frac{\partial}{\partial x}V(x) + \Theta(t) + \xi(t). \tag{2.64}$$

The additional term causes a time-dependent tilt of the ratchet potential and could also be a stochastic term [88, 72]. The random force term $\xi(t)$ in pulsating as well as tilting ratchets is uncorrelated, Gaussian noise as defined by the fluctuation-dissipation theorem in Eq. (2.49). In the third group of non-equilibrium perturbations, the Langevin equation features correlated, non-Gaussian noise $\xi_\Theta(t)$ [6]. The time-correlation of the noise

$$\langle \xi_\Theta(t)\xi_\Theta(t')\rangle = \Theta(t-t'). \tag{2.65}$$

is generally given by a function $\Theta(t-t')$ deviating from the δ-function which gives uncorrelated noise.

In this section, we summarized overdamped ratchet systems. However, the investigation of inertial ratchets has revealed interesting phenomena at the edge to chaotic behavior [62, 91]. Further, ratchet models can be arbitrary combinations of the above groups or not belong to any category. For a complete overview about various ratchet types we refer to the detailed reviews of Reimann [106] and Hänggi *et al.* [48].

2.4 Ratchet-based particle separation

In this section, we discuss how the rectification of Brownian motion in ratchet systems can be exploited for microfluidic particle separation. We firstly explain the basic idea of the separation process before we introduce a corresponding ratchet model. Subsequently, we discuss the effect of obstacles that are impermeable to the driving force and the effect of the finite size of particles.

2.4.1 Concept of the separation process

Several microfluidic devices have been introduced to exploit the ratchet effect for particle separation [36, 38]. A device demonstrating the underlying concept is schematically depicted in Fig. 2.7. As shown in panel (a), the particles are locally injected on the left hand side of the device and are driven through a periodic array of identical obstacles by an external force f_x. The obstacles feature a spatial asymmetry with respect to the direction of the force. Each time a particle passes a row of obstacles the ratchet effect induces a mean displacement in y-direction. As a result, the mean trajectory of the particles is inclined to the direction of the external force. If the induced mean displacements are different for two types of particles, each type will move in average towards another direction and both types will eventually be separated. Since the separation process is of stochastic nature, the exit positions of the particles at the right hand side of the array are distributed rather than well defined. Due to the angular resolution of the direction of the mean trajectory, this separation method has also been denoted as vector chromatography [33, 34].

We now explain how the ratchet effect causes a mean displacement each time the particle passes a row of obstacles. In panel (b), we therefore consider

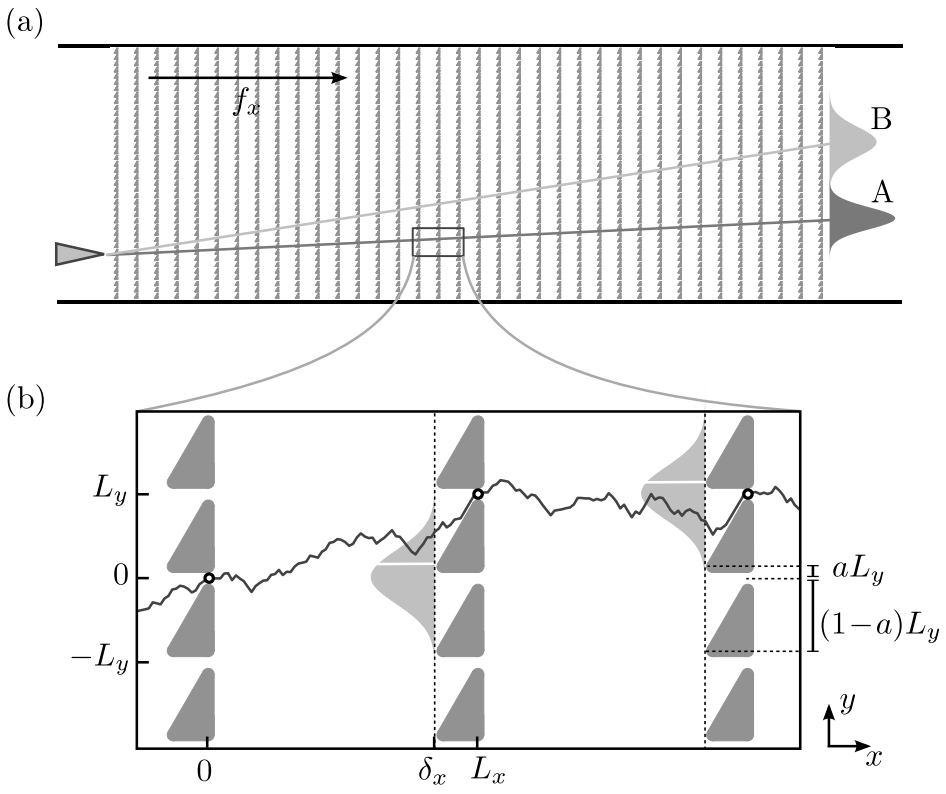

Figure 2.7: Schematic microfluidic device for ratchet-based particle separation. (a) Periodic array of obstacles confined by two walls. Particles are injected at one point and driven by an external force through the device. The mean trajectories for two distinct particle types are indicated, as well as, the distribution after having passed the device. (b) Example of a trajectory passing three rows of obstacles.

a single particle of type A driven through such an array starting in the gap at $(x = 0, y = 0)$. While the particle travels through the device in x-direction, it diffuses in y-direction. When it reaches the next row of obstacles at $x = \delta_x$ the probability to find it at a certain y-position is hence given by a Gaussian distribution. As a consequence, the particle has a certain probability p_{+1} to pass the row of obstacles through the gap at (L_x, L_y), *i.e.*, to make a step upwards. Any trajectory that reaches $x = \delta_x$ above the edge of the next obstacle at $y = aL_y$, makes such a step upwards. For a downward step through

the gap at $(L_x, -L_y)$, the particle has to reach $x = \delta_x$ below $y = -(1-a)L_y$. The step probabilities are given by the corresponding fraction of the Gaussian distribution. Due to the asymmetry of the obstacles, upward steps are more likely than downward steps. To be precise, in the given example the probability for downward steps is negligible. The bias of the probabilities ($p_{+1} > p_{-1}$) causes the mean displacement in y-direction, which eventually leads to the inclination of the mean trajectory. We now consider a particle of type B and assume that it needs a longer time to travel the distance δ_x between the rows of obstacles. As a result the Gaussian distribution is wider compared to the first particle. Therefore, the step probability p_{+1} is larger and eventually the trajectory of the particle is more inclined.[6]

2.4.2 Ratchet model

The separation dynamics can be mapped onto the on-off ratchet model, which has been introduced in Sec. 2.3.2. The diffusion in y-direction while the particle travels between two rows of obstacles corresponds with the diffusion of the particle during the off-time. Further the influence of the obstacle on the trajectory of the particle corresponds with the influence of the ratchet potential during the on-time. In particular, the gaps between two obstacles corresponds with the minima of the potentials. Since the particle has to pass through a gap, we can apply the method of discrete steps to calculate the inclination angle.

We consider particles with size σ, mobility μ and diffusion constant D. Further, we assume that the external force $f_x = Q\,F_x$ can be split into two

[6] The probability for an downward step p_{-1} actually also increases for a wider distribution, however, the probability for an upward step increases more.

terms. The particle-dependent term Q can be considered as a charge, while the particle-independent term F_x has the meaning of a field strength. In case of gravitational driving, $Q = \Delta m$ and $F_x = g$ with the mass difference between the particle and the equivalent amount of the solvent Δm and the gravitational acceleration constant g. The average time for a particle to travel the distance δ_x between two rows is hence given by

$$t_{\text{off}} = \frac{\delta_x}{\mu Q F_x}, \tag{2.66}$$

which we denote as t_{off} in analogy to the off-time in Sec. 2.3.2. Here, $\mu Q F_x$ is the mean drift velocity of the particle. The effect of the diffusion in x-direction on the travel time is neglected in this model. Using L_y as intrinsic length scale, the diffusion time scale is given by

$$t_{\text{diff}} = \frac{L_y^2}{D}. \tag{2.67}$$

The rescaled off-time is hence given by

$$\tau_{\text{off}} = \frac{t_{\text{off}}}{t_{\text{diff}}} = \frac{D\,\delta_x}{\mu Q F_x L_y^2}. \tag{2.68}$$

In analogy to the on-off ratchet, the behavior of the particle in the separation device is only determined by the rescaled off-time τ_{off} and the asymmetry parameter a. As indicated in Fig. 2.7 (b), the asymmetry parameter is fully determined by the shape of the obstacle. The step probabilities p_n take the same form as in Eq. (2.59)

$$p_n = \int_{n-1+a}^{n+a} \frac{\mathrm{d}\bar{y}}{\sqrt{4\pi\tau_{\text{off}}}}\ \exp\left(-\frac{\bar{y}^2}{4\tau_{\text{off}}}\right), \tag{2.69}$$

with the rescaled position $\bar{y} = y/L_y$. The rescaled mean displacement is hence given by

$$\langle \Delta \bar{y} \rangle = \sum_n n \cdot p_n, \tag{2.70}$$

in analogy to Eq. (2.60). The inverse of the rescaled mean displacement gives the average number of passages that a particle needs in order to make one step upwards and is hence directly linked with the inclination angle θ of the mean trajectory with respect to the direction of the driving force f_x through

$$\tan \theta = \frac{\langle \Delta \bar{y} \rangle \, L_y}{L_x}. \tag{2.71}$$

For strongly diffusive particles ($\tau_{\text{off}} > 0.1$), the rescaled mean displacement reaches the known limit of $\langle \Delta \bar{y} \rangle_{\max} = 1/2 - a$, which limits the inclination angle for a given geometry (see Fig. 2.5 (b)).

In many cases the system can be tuned such that all step probabilities apart from p_{+1} can be neglected by adjusting the external force f_x properly. For this scenario, the stepping process among the gaps in subsequent rows resembles a binomial process. While passing N_x rows of obstacles a particle makes in average $p_{+1}N_x$ upward steps. The width of the distribution around this mean value is given by $(p_{+1}p_0N_x)^{1/2}$. Since the width of the distribution grows slower than the displacement with increasing N_x, the resolution of the device can be improved by adding more rows.

Conventional external force

As already mentioned, the rescaled mean displacement and hence the inclination angle are fully determined by τ_{off} and a. Since a is a property of the obstacle, the particles need to have distinct values of τ_{off} to be separated. In

Eq. (2.68) for the rescaled diffusion constant, we see that the particle-specific information is given by the ratio $D/(\mu Q)$. This is however problematic since the mobility is connected to the diffusion constant through the Einstein relation $D = \mu k_{\mathrm{B}} T$. Thus, the rescaled off-time is independent of μ and D

$$\tau_{\mathrm{off}} = \frac{1}{Q} \frac{k_{\mathrm{B}} T \, \delta_x}{F_x L_y^2}. \tag{2.72}$$

Still particles can be separated with respect to their specific value of Q. However, the particularly interesting scenario of separation with respect to the size of the particles can not be achieved by this approach, if Q is independent of the particle size. Note that Eq. (2.72) was derived under the assumption of a homogenous external force. However, only magnetic and gravitational forces are virtually unaffected by the presence of the obstacles and can provide the assumed homogeneity.

Pressure-driven flows

An intriguing approach to ratchet-based particle separation is to drive the particles by a pressure gradient through the device instead of using an external force. In that case, the types of particles travel with identical velocities v_x and have the same value for t_{off}. The corresponding rescaled off-time

$$\tau_{\mathrm{off}} = D \, \frac{\delta_x}{v_x \, L_y^2}, \tag{2.73}$$

depends on the value for D which is directly related to the size of the particle. In such pressure-driven devices, however, the flow field is not homogeneous since the obstacles are impermeable to the fluid. The consequence of such non-homogeneous driving is discussed in section 2.4.3.

Separation of DNA

One important application of microfluidic particle separation is the separation of DNA with different contour lengths, *i.e.*, with different number of base pairs N_{bp}. In solution DNA forms random coils with a size proportional to $N_{\mathrm{bp}}^{1/2}$. The diffusion coefficient is hence proportional to $N_{\mathrm{bp}}^{-1/2}$. The drift velocity v_{DNA} of DNA in electrophoretic flow is however independent on the number of base pairs for typically used electric fields [114]. Therefore the rescaled off-time

$$\tau_{\mathrm{off}} \sim N_{\mathrm{bp}}^{-1/2} \tag{2.74}$$

depends on the number of base pairs, which facilitates the separation of different types of DNA molecules. Such separation has been demonstrated in Ref. [19, 52, 54]. As already mentioned in Sec. 1.2, the results deviate quantitatively from the theoretical predictions. The deviations originate from the inhomogeneity of the electrophoretic force. Similar to pressure-driven flows, the induced ion flow is not able to penetrate the obstacles and the resulting electric field is hence bent around the obstacles [5, 82].

2.4.3 The effect of impermeable obstacles

In this section, we consider the effect of obstacles that are impermeable for the external force. As discussed in the previous section, this is the case for pressure-driven flows as well as electrophoretic forces. We constrain the discussion to pressure-driven systems, since they are more relevant for this thesis. The reasoning is nevertheless similar for electrophoretic forces.

The fluid flow through the array is generated by a constant pressure gradient along the device. The flow lines around the discussed obstacle are depicted

in Fig. 2.8 (a) and are compared to homogeneous field lines in panel (b). The effect of impermeable obstacles can now be discussed by regarding the trajectories of *point-like* particles. Diffusion of the particle is omitted as it is not relevant for the discussed effect. In panel (a), two particles start at x_A close to the flow line that bifurcates at the obstacle. In panel (b), both particles start on the field line that reaches the obstacle at the foremost edge. In both scenarios, we follow one particle that moves upwards and one that moves downwards around the obstacle. After they have traveled around the obstacles they arrive at x_B. For the homogenous driving force, the trajectories effectively bifurcate and the particles are spatially separated. In case of the pressure-driven flow, however, the particles eventually arrive at the same point. This is a direct consequence of the incompressibility of the fluid (see Eq. (2.2)). In other words, the particle does not remember the obstacle after having traveled around it. As a consequence, the ratchet-based separation mechanism breaks down, since it makes no difference through which gap the particle travels.[7]

The difference between both scenarios occurs in the vicinity of the obstacles. For the homogeneous force, the particle reaches the surface of the obstacle and is deflected by a repulsive force. As a result, it slides along the surface towards the gap and thereby crosses several field lines which enter the obstacle. Later the particle is separated from the other particle by exactly the number of field lines that it has crossed on its way to the gap. The requirement for a sustainable bifurcation is hence that the field has a non-vanishing component perpendicular to the surface of the obstacle. It is exactly this component of the pressure-driven flow that vanishes at the surface of the obstacle due to stick-boundary conditions. The described effect is reduced if the obstacle is

[7]Independent on its initial position, a point-like particle always reaches the initial y-position after having passed one spatial period L_x.

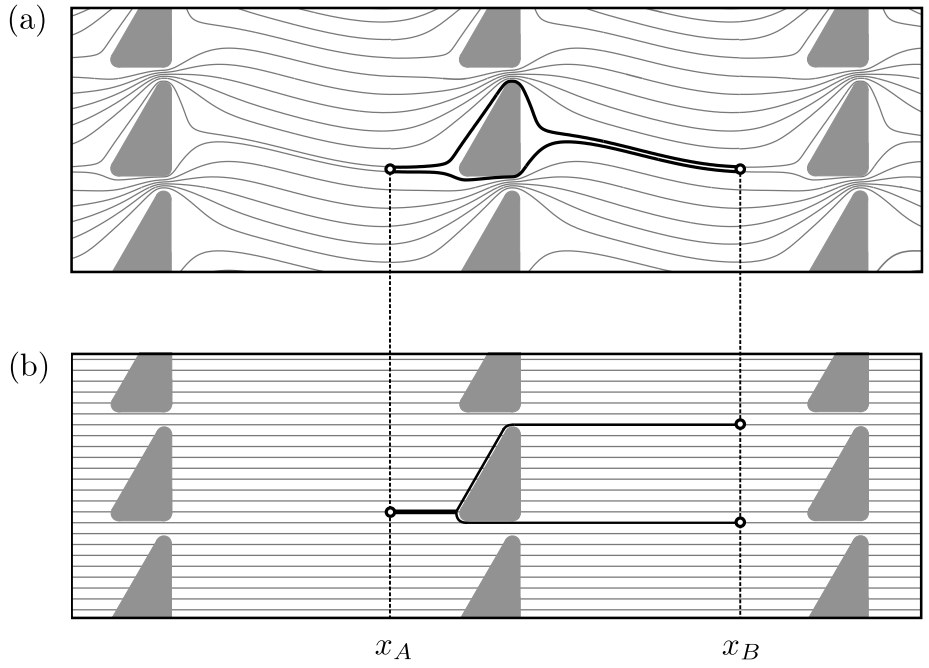

Figure 2.8: Bifurcation of particle trajectories at an obstacle for two different scenarios. (a) Obstacles that are completely impermeable to the external field. Here a pressure-driven flow is depicted, which has been generated by the method introduced in Sec. 4.2. (b) Obstacles that are fully permeable to the homogeneous field.

partially permeable to the field, since there will be a non-vanishing component of the force perpendicular to the surface of the obstacle.

2.4.4 Finite size effects

The discussion in the previous section changes significantly if we consider particles with a finite size. In Fig. 2.9, we compare the trajectories of particles with distinct diameters within a pressure-driven flow. Again the particles start at x_A close to the flow line that bifurcates. The finite size crucially alters the trajectories while the particles move to the gaps at x_B along the surface of the

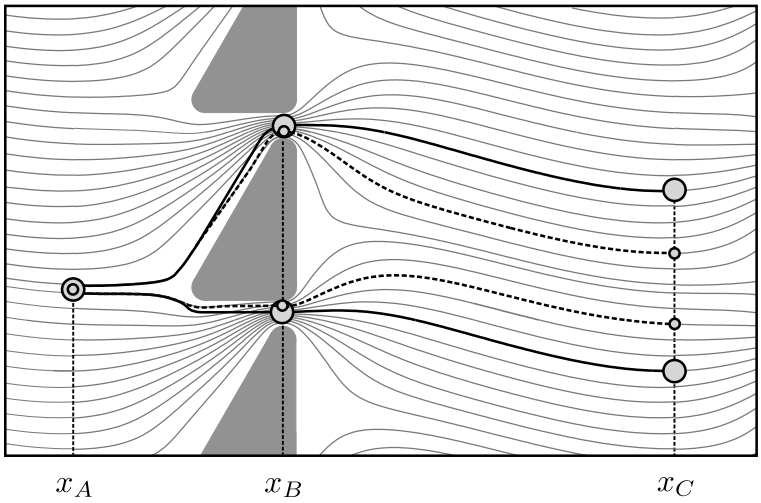

Figure 2.9: The effect of the finite size of a particle on the bifurcation at an obstacle for impermeable obstacles. The black lines indicate the trajectories of the particles: larger particle (solid line), smaller particle (dashed line).

obstacles.[8] Due to their spatial extension, it is not possible for the particles to follow the flow line. As a consequence, they are displaced towards other flow lines, which they follow after having passed the gap. This displacement eventually causes a sustainable separation of both trajectories at x_C. The repulsive interaction between particles and obstacles causes the required force perpendicular to the surface. The bifurcation is wider for larger particles, as the displacement induced by the particle-obstacle interaction is larger.[9] Giv-

[8]It is assumed that particles follow the flow field according to the flow velocity at their center. This approach neglects the motion induced by shear flows. Further, the effect of the presence of the particle on the flow field is neglected.

[9]The finite-size effect itself has been exploited for particle separation by a method denoted as deterministic lateral displacement (DLD) [27, 56, 57, 53]. A change in the geometry of the array is required for that method. Subsequent rows obstacles need to be displaced by a fraction of L_y in y-direction. In DLD devices, a pressure-driven flow is generated across a periodic array of pillars. Due to the vertical displacement of subsequent rows, several periodic flow bands arise. Depending on their size, particles in such a flow pattern either follow a zig-zag motion without any net-displacement or they are displaced to the adjacent flow band each time they pass a pillar. There is a critical size separating both modes of motion. This allows the separation of particles into the ones smaller and larger than the critical size, respectively. Since DLD is a deterministic approach rather than ratchet-based,

ing an asymmetric flow field, *i.e.*, a field that leads to biased step probabilities $p_{+1} > p_{-1}$, the effective bifurcation enables ratchet based particle separation.

Due to the finite size, the step probabilities are not equal for every passage, but rather depend on the actual trajectory. A particle that made a step upwards has an increased probability to make a downward step during the subsequent passage and *vice versa*. This path-dependence of the step probabilities reduces the induced mean displacement and hence reduces the effectivity of the separation process. For particles with a diameter close to the gap size, the step probabilities become path-independent. The impact of finite size has been demonstrated in Ref. [54], for coils of DNA molecules with various sizes. In agreement with the discussion in the previous section, no inclination has been observed for coils significantly smaller than the gap. The trajectories of coils with sizes similar to the gap width, were inclined. However, the observed inclination angles were smaller than predicted by ratchet theory. The applied model used the geometrical asymmetry a of the obstacles. As we will show in chapter 4, the effective asymmetry of the flow field differs significantly from the asymmetry of the obstacle.

2.5 Dynamics of colloidal systems

In the previous sections, the discussion was limited to single particles. Throughout this thesis single particle systems will serve as useful reference systems. For our studies on particle separation and hydrodynamic interactions we are however interested in the dynamics of systems containing many particles. In this section, we therefore extend the Langevin equation to many-particle sys-

no asymmetry is required and symmetric obstacles are sufficient.

tems including hydrodynamic interactions and particle interactions. Further, we introduce an algorithm for the numerical integration of the Langevin equation.

2.5.1 Hydrodynamic interactions

We have shown in Sec. 2.1.2 that a translating particle causes a flow field. This field influences the motion of other particles in the fluid. This effect is significant in colloidal systems and is known as hydrodynamic interaction or hydrodynamic coupling. Unfortunately a closed solution of the Stokes equation (2.14) for systems containing more than one particle is generally not possible. We therefore introduce approximative methods to describe hydrodynamic interactions.

We consider the motion of N spherical particles in an infinite, viscous fluid. As discussed in Sec. 2.1.2, we can limit the discussion to time-scales larger than the momentum relaxation time (see Eq. (2.12)) and small Reynolds numbers (see Eq. (2.4)). The system is hence governed by the linear Stokes equation. Due to the linearity, the translational and angular velocities $\boldsymbol{v}_i$ and $\boldsymbol{\omega}_i$ depend linearly on the external forces $\boldsymbol{f}_j$ and torques $\boldsymbol{t}_j$ acting on each particle. Four possible types of coupling occur among translations (index t) and rotations (index r). The equation of motion for particle i can hence be written as

$$\boldsymbol{v}_i = \sum_{j=1}^{N} \left(\boldsymbol{\mu}_{ij}^{\mathrm{tt}}(\boldsymbol{r}_1, \ldots, \boldsymbol{r}_N) \cdot \boldsymbol{f}_j + \boldsymbol{\mu}_{ij}^{\mathrm{tr}}(\boldsymbol{r}_1, \ldots, \boldsymbol{r}_N) \cdot \boldsymbol{t}_j \right), \tag{2.75}$$

$$\boldsymbol{\omega}_i = \sum_{j=1}^{N} \left(\boldsymbol{\mu}_{ij}^{\mathrm{rt}}(\boldsymbol{r}_1, \ldots, \boldsymbol{r}_N) \cdot \boldsymbol{f}_j + \boldsymbol{\mu}_{ij}^{\mathrm{rr}}(\boldsymbol{r}_1, \ldots, \boldsymbol{r}_N) \cdot \boldsymbol{t}_j \right). \tag{2.76}$$

The hydrodynamic coupling of the particles is described by four 3×3 mobility

tensors $\boldsymbol{\mu}_{ij}^{\mathrm{tt}}$, $\boldsymbol{\mu}_{ij}^{\mathrm{rr}}$, $\boldsymbol{\mu}_{ij}^{\mathrm{tr}}$ and $\boldsymbol{\mu}_{ij}^{\mathrm{rt}}$. In general, these tensors are functions of the complete spatial configuration of all particles [31].[10] In this thesis, we are mainly interested in translational motion. Further no external torques are applied. We hence limit the discussion in the following to purely translational coupling and omit the indices.

For sake of conciseness, we introduce the $3N$ dimensional vectors $\mathbf{v} = [\boldsymbol{v}_1, \ldots, \boldsymbol{v}_N]$ and $\mathbf{f} = [\boldsymbol{f}_1, \ldots, \boldsymbol{f}_N]$. For neglected random forces, the equations of motion hence take the following form

$$\mathbf{v} = \mathbf{M} \cdot \mathbf{f} \tag{2.77}$$

with the $3N \times 3N$ mobility matrix

$$\mathbf{M} = \begin{bmatrix} \boldsymbol{\mu}_{11} & \cdots & \boldsymbol{\mu}_{1N} \\ \vdots & \ddots & \vdots \\ \boldsymbol{\mu}_{N1} & \cdots & \boldsymbol{\mu}_{NN} \end{bmatrix}. \tag{2.78}$$

The mobility matrix has two important features. First, the symmetry relation

$$(\boldsymbol{\mu}_{ij})^{\mathrm{T}} = \boldsymbol{\mu}_{ij} \tag{2.79}$$

holds, such that $\mathbf{M} = \mathbf{M}^{\mathrm{T}}$. Second, the matrix is positive-definite. The latter guarantees that the dissipated energy is always positive. The dissipated power is given by $P = \mathbf{f} \cdot \mathbf{v}$ which can be written as $P = \mathbf{f} \cdot \mathbf{M} \cdot \mathbf{f}$. For positive-definite $\mathbf{M}$, the dissipated energy is $P > 0$ for arbitrary forces $\mathbf{f}$.

[10] For non-spherical particles the mobility tensors also depend on the orientation of each particle.

2.5.2 Rotne-Prager approximation

In this section, we derive an expression for the mobility matrix as a function of the spatial configuration of the particles. We consider spherical particles with radius σ. Again we assume an infinite fluid that is in rest at infinity and no-slip boundary conditions at the surface of the particles. In order to derive the mobility matrices for finite-size particles, we apply the method of reflexion [31]. The latter is based on the idea that the flow field is "reflected" from particles and can be calculated by iterative reflection steps. At each step the flow field needs to be adjusted such that the boundary conditions are fulfilled. This approach yields a series of correction terms that will be truncated to get the Rotne-Prager approximation.

The method of reflection is based on Faxén's theorem [31], which yields the velocity of a particle $\boldsymbol{v}$ in the flow field $\boldsymbol{u}(\boldsymbol{r})$ and driven by the force $\boldsymbol{f}$. The considered flow field is the unperturbed solution of the Stoke equation, *i.e.*, without the presence of the particle. According to Faxén's theorem, the velocity of a particle at position $\boldsymbol{s}$ is given by

$$\boldsymbol{v} = \mu \boldsymbol{f} + \left(1 + \frac{1}{6}\,\sigma^2 \nabla^2\right) \boldsymbol{u}(\boldsymbol{r})\Big|_{\boldsymbol{r}=\boldsymbol{s}}. \tag{2.80}$$

In the first step, we start with particle 1 under the force $\boldsymbol{f}_1$. The zeroth-order approximation for the equation of motion is

$$\boldsymbol{v}_1^{(0)} = \mu\, \boldsymbol{f}_1. \tag{2.81}$$

The flow field induced by the translation of such particle $\boldsymbol{u}^{(0)}(\boldsymbol{r})$ is given in Eq. (2.8). This flow field now induces a velocity to a second particle according

to Faxéns theorem [11]

$$\boldsymbol{v}_2^{(1)} = \mu \boldsymbol{f}_2 + \left(1 + \frac{1}{6}\,\sigma^2 \nabla^2\right) \boldsymbol{u}^{(0)}(\boldsymbol{r})\Big|_{\boldsymbol{r}=\boldsymbol{r}_2} . \tag{2.82}$$

The motion of the second particle induces an additional flow field $\boldsymbol{u}^{(1)}(\boldsymbol{r})$ given by Eqs. (2.7, 2.8) with $\boldsymbol{v} = \boldsymbol{v}_2^{(1)}$. In some sense the initial flow field has been reflected by the second particle. The resulting flow field $\boldsymbol{u}^{(0)}(\boldsymbol{r})+\boldsymbol{u}^{(1)}(\boldsymbol{r})$ fulfills the no-slip boundary condition at the surface of particle 2 but is perturbed at the surface of particle 1.

In the next iteration step we correct this deviation by another application of Faxén's theorem. This time we calculate the motion of particle 1 induced by the reflected field $\boldsymbol{u}^{(1)}(\boldsymbol{r})$. We set $\boldsymbol{f}_1 = 0$, since it has already been taken into account in Eqs. (2.81, 2.82), and get

$$\boldsymbol{v}_1^{(2)} = \left(1 + \frac{1}{6}\,\sigma^2 \nabla^2\right) \boldsymbol{u}^{(1)}(\boldsymbol{r})\Big|_{\boldsymbol{r}=\boldsymbol{r}_1} . \tag{2.83}$$

This motion again induces a flow field $\boldsymbol{u}^{(2)}(\boldsymbol{r})$ which requires some correction to fulfill the boundary condition at the surface of particle 2. The continuation of this iterative process leads to the series

$$\boldsymbol{u}(\boldsymbol{r}) = \boldsymbol{u}^{(0)}(\boldsymbol{r}) + \boldsymbol{u}^{(1)}(\boldsymbol{r}) + \boldsymbol{u}^{(2)}(\boldsymbol{r}) + \cdots \tag{2.84}$$

for the exact flow field. Accordingly the velocities of both considered particles

[11] We assume that changes of the flow field induced by particles instantly apply to other particles. A thorough investigation revealed that perturbations spread through two effects. One is spreading through spherical sound waves, that travel with the corresponding speed of sound c [20, 50]. The other is an expanding vortex ring that spreads diffusively. To spread over a distance r the sound waves need the time $\tau_1 = r/c$ whereas the vortex rings need $\tau_2 = r^2/\nu$, with $\nu = \eta/\rho$ being the kinematic viscosity of the fluid. For the considered systems, $\tau_1 < \tau_2 \approx 0.1\,\mathrm{ms}$, which is shorter than the time scales we are interested in.

are given by the following series

$$\begin{aligned} \boldsymbol{v}_1 &= \boldsymbol{v}_1^{(0)} + \boldsymbol{v}_1^{(2)} + \cdots , \\ \boldsymbol{v}_2 &= \boldsymbol{v}_2^{(1)} + \boldsymbol{v}_2^{(3)} + \cdots . \end{aligned} \tag{2.85}$$

All three series can be written as potential series of σ/r_{ij}. For the Rotne-Prager approximation, the series is truncated after the first iteration step in Eq. (2.84). For the mobility tensors we get the following expressions

$$\begin{aligned} \boldsymbol{\mu}_{ii} &= \mu\,\mathbf{1} + \mathcal{O}(4), \\ \boldsymbol{\mu}_{ij} &= \mu \left[\frac{3}{4}\frac{\sigma}{r_{ij}}(\mathbf{1} + \hat{\boldsymbol{r}}_{ij} \otimes \hat{\boldsymbol{r}}_{ij}) + \frac{1}{2}\left(\frac{\sigma}{r_{ij}}\right)^3 (\mathbf{1} - 3\hat{\boldsymbol{r}}_{ij} \otimes \hat{\boldsymbol{r}}_{ij}) \right] + \mathcal{O}(4) \end{aligned} \tag{2.86}$$

with $\mathcal{O}(n)$ being the error in orders of $(\sigma/r_{ij})^n$ [93]. Note that the first term in the latter equation corresponds with the Oseen tensor describing hydrodynamic interactions for large particle distances.[12] The mobility tensors reveal the characteristic long-range nature of hydrodynamic interactions, as they decay asymptotically with σ/r_{ij}

The Rotne-Prager approximation considers only two-particle interactions. For many-particle effects more iterations need to be taken into account. It was shown that the Rotne-Prager method describes hydrodynamic interactions precisely for particle distances $r_{ij} > 3\sigma$.

[12]The Oseen tensor is derived from the flow field generated by a point-like particle. The force density acting on the fluid is hence given by a delta function. The Oseen tensor can therefore be considered as the Green function of the Stokes equation. The Oseen tensor is a good approximation for hydrodynamic interactions at large distances. In this case, the impact of the particles on the fluid flow can reasonably be reduced to the impact of point-like objects. The Oseen tensor already features the long-ranged character.

2.5.3 Langevin equation of many-particle systems

We now extend the single-particle Langevin equation in Sec. 2.2.1 to describe N particles including their hydrodynamic interactions and repulsive interactions among particles.

As discussed in Sec. 2.1.1, colloidal particles interact in various ways, *e.g.*, hard-core interaction, electrostatic interaction and van-der-Waals interaction. In this thesis, however, we limit the discussion to hardcore interactions. For the studied phenomena, the particular interaction has no qualitative implications as long as particle overlap is inhibited. For the sake of simplified numerical handling, we use a quasi hard-core potential. For two particles with radii σ_i and σ_j the interaction potential is given by

$$V_{\mathrm{rep}}(r_{ij}) = C\left[\left(\frac{r_{ij}}{(\sigma_i+\sigma_j)}\right)^{12} - 1\right]^{-1}. \tag{2.87}$$

Here, $r_{ij} = |\boldsymbol{r}_i - \boldsymbol{r}_j|$ is the center-center distance between particles i and j. The corresponding repulsive force is given by

$$\boldsymbol{f}_{\mathrm{rep},ij}(r_{ij}) = -\frac{\partial}{\partial r_{ij}} V_{\mathrm{rep}}(r_{ij})\,\hat{\boldsymbol{r}}_{ij} \tag{2.88}$$

with $\hat{\boldsymbol{r}}_{ij} = \boldsymbol{r}_{ij}/r_{ij}$ being the unit vector pointing from particle i to particle j. The total force on particle i is given by the sum of external and repulsive forces

$$\boldsymbol{f}_i = \boldsymbol{f}_{\mathrm{ext},i} + \sum_j \boldsymbol{f}_{\mathrm{rep},ij}. \tag{2.89}$$

Using the $3N$ dimensional vectors $\mathbf{v} = [\boldsymbol{v}_1, \ldots, \boldsymbol{v}_N]$ and $\mathbf{f} = [\boldsymbol{f}_1, \ldots, \boldsymbol{f}_N]$

from Sec. 2.5.1, the Langevin equation for N particles can be written as

$$\mathbf{Z}(\mathbf{r}) \cdot \dot{\mathbf{r}} = \mathbf{f}(\mathbf{r}, t) + \boldsymbol{\xi}(t). \tag{2.90}$$

The stochastic force $\boldsymbol{\xi}(t)$ obeys the fluctuation-dissipation theorem

$$\langle \boldsymbol{\xi}(t) \otimes \boldsymbol{\xi}(t') \rangle = 2k_{\mathrm{B}}T\, \mathbf{Z}(\mathbf{r})\, \delta(t - t'). \tag{2.91}$$

This is a set of $3N$ stochastic differential equations which are coupled through the friction matrix $\mathbf{Z}$ and the repulsive forces, which both depend on the complete spatial configuration of the system.

2.5.4 Brownian dynamics simulations

For the numerical integration of the Langevin equation we use the algorithm of Ermak and McCammon [37]. The change of the particle positions $\mathrm{d}\mathbf{r}$ after one simulation step with the time interval $\mathrm{d}t$ is given by

$$\mathrm{d}\mathbf{r} = \mathbf{M} \cdot \mathbf{f}\, \mathrm{d}t + \mathbf{A} \cdot \mathrm{d}\mathbf{w}. \tag{2.92}$$

The total displacement contains a deterministic drift term and a random displacement.[13] The latter consists of a random vector $\mathrm{d}\mathbf{w}$ which is independent

[13] The full expression also contains an additional spurious drift term $\nabla\mathbf{D}\,\mathrm{d}t$. The latter originates from inertial effects on times scales smaller than the inertia relaxation time, and can hence not be derived from the overdamped Langevin equation. For the Rotne-Prager approximation, however, the spurious drift term vanishes, since $\nabla\mathbf{D} = \mathbf{0}$ [37].

on the spatial configuration of the system with the properties

$$\begin{aligned} \langle \mathrm{d}\mathbf{w} \rangle &= \mathbf{0}, \\ \langle \mathrm{d}\mathbf{w} \otimes \mathrm{d}\mathbf{w} \rangle &= \mathbf{1}\mathrm{d}t. \end{aligned} \tag{2.93}$$

and the $3N \times 3N$ amplitude matrix $\mathbf{A}$ that obeys

$$\mathbf{A} \cdot \mathbf{A}^{\mathrm{T}} = 2\mathbf{D}. \tag{2.94}$$

During the simulation $\mathbf{A}$ is determined by a Cholesky decomposition of $\mathbf{D}$ which is always possible since the matrix is positive definite [100]. Furthermore, the components of $\mathbf{M}$, $\mathbf{A}$ and $\mathbf{f}$ are calculated at the beginning of each simulation step, following the Itô interpretation of stochastic processes. For the Cholesky decomposition and the generation of random numbers we use the GNU scientific library [44].

The integration scheme in Eq. (2.92) yields N trajectories in three-dimensional space, which are a solution of the corresponding Langevin equation (2.90). It has to be kept in mind that the described method is only valid for spherical particles in an infinite fluid. The presence of walls significantly modifies the characteristics of hydrodynamic interactions. For example, it has been shown that infinite planar walls screen hydrodynamic interactions [23, 35].

Chapter 3

Selective pumping in microchannels

3.1 Motivation

In ratchet-based separation devices, the suspended particles are driven through rows of asymmetric obstacles with the help of an external force. As discussed in Sec. 2.4, the ratchet effect induces a mean displacement in direction perpendicular to the direction of the external force. The net flow of particles through the device is hence inclined with respect to the external force. Differences in the magnitude of the induced mean displacement between distinct types of particles lead to different inclinations and to particle separation. Compared to conventional technologies, like gel electrophoresis, such devices offer several advantages including continuous separation. However, the classical implementation of the device has two major drawbacks. First, the number of rows of obstacles, and consequently the size of the device, has to be increased, in order to improve the resolution. Second, a localized injection of the particles

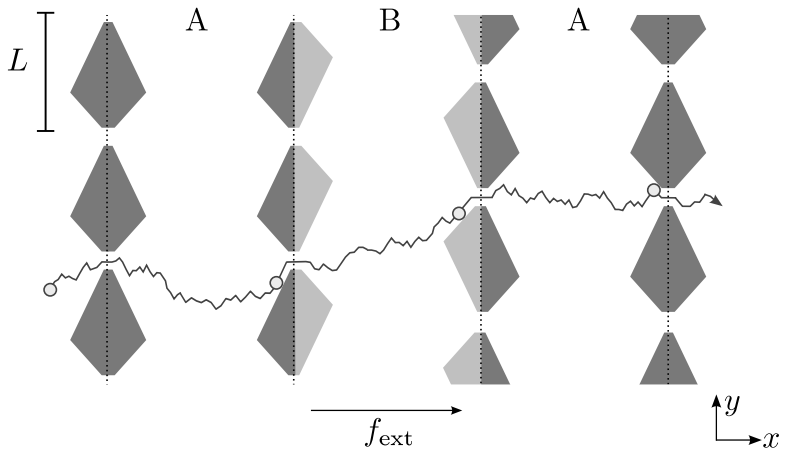

Figure 3.1: Microfluidic array devices for particle separation that benefit from the effect of direction reversal proposed by Derenyi *et al.* [29]. The solid line represents an example trajectory of a particle driven by an external force f_{ext} with constant strength but periodically changing sign (example trajectory only shown for one direction). The dark and light gray objects refer to the obstacles of type A and B, respectively.

is required for optimal separation. Localized injection, however, reduces the throughput of the device (see Section 2.4 for a detailed discussion).

It has been pointed out by Derenyi *et al.* [29] that the exploitation of the direction reversal effect would overcome both disadvantages. In Fig. 3.1, the proposed design is depicted. It is similar to the conventional array that has been discussed in Sec. 2.4.1. However, two changes are introduced. First, the obstacles feature spatial reflection symmetry with respect to the y-axis. In such an array, an external force with constant strength, but periodically alternating sign, can be applied driving the particles back and forth through several rows of obstacles in each direction. Each time the particles pass a row, they have a certain probability to make a step up- or downwards. If all rows are of type A, there will be a positive mean displacement in y-direction independent of the particle properties. Hence, no direction reversal occurs. Since the external

force has no bias, there is no net transport in x-direction and all particles move in average in y-direction, thus with different mean velocities. Note that the mean velocity increases with larger values for the rescaled off-time.[1] The resulting unidirectional transport clearly nullifies the intriguing advantage of the conventional array, namely the directional resolution.

Hence, a second modification is required. A certain fraction of rows is replaced by rows of type B. The obstacles within these rows feature inverted spatial asymmetry with respect to the x-axis. Further, these rows are displaced by half a spatial period L in y-direction. In contrast to rows of type A, the new rows induce a negative mean displacement in y-direction whose absolute magnitude decreases for larger values of the rescaled off-time.[2] As a consequence, a device containing both types of rows can be tuned such that the induced mean displacements for distinct types of particles have opposite signs.[3] In such scenario, two distinct types of particles would separate along the y-axis by moving towards opposite directions. This allows the reduction of the device to a few rows in x-direction. Further, the proposed separation process works even without localized injection of the particles.

In this chapter, we demonstrate how this approach can be further optimized. In line with the idea of Derenyi *et al.*, our approach exploits the direction reversal effect. For this purpose we introduce an extended version of the on-off ratchet, which features the required direction reversal and derive analytic expressions for the mean displacement. Subsequently we translate

[1] This is in full analogy to the mean displacement in conventional arrays as discussed in Sec. 2.4.1. See in particular Fig. 2.7.

[2] Without diffusion, *i.e.*, for $\tau_{\text{off}} = 0$, it is apparent that a downward step happens for every passage through a row of type B. For increasing values of τ_{off}, upward steps become more likely, accordingly, the absolute mean displacement decreases. For large values of τ_{off}, up- and downward steps balance.

[3] In a system that contains equal numbers of rows of both types, the induced mean velocities compensate mutually and zero mean displacement occurs.

the characteristic features of the ratchet model into a microfluidic device with significantly reduced spatial dimensions. In fact, we show that the size can be reduced to a single channel without sacrificing the resolution of the separation process. Subsequently we validate our predictions with the help of Brownian dynamics simulations for the microfluidic channel device.

3.2 The extended on-off ratchet

The simple on-off ratchet relies on an asymmetric sawtooth potential that is turned on and off and thereby induces a drift in one direction. A simple modification of this ratchet replaces the sawtooth potential in every second on-state by a sawtooth potential of inverse asymmetry and half the spatial periodicity. The second sawtooth potential alone would induce a drift in the reverse direction. We show that in such an extended ratchet the average drift direction can be controlled by variation of system parameters such as the time during which the potentials are switched on.

3.2.1 Details of the model

In the simple on-off ratchet, a Brownian particle moves under the influence of a sawtooth potential V_1, which is periodically switched on and off. For sake of coherence we briefly summarize the key features of the on-off ratchet model (see the detailed discussion in Sec. 2.3.2). The sawtooth potential and the ratchet cycle are schematically depicted in panel (a) and (b) of Fig. 3.2, respectively. The potential V_1 is characterized by a spatial period L, asymmetry a, and amplitude $\hat{V}$. When the potential is switched off during a time t_{off}, the particle diffuses freely along the x-axis. When the potential is switched on during a

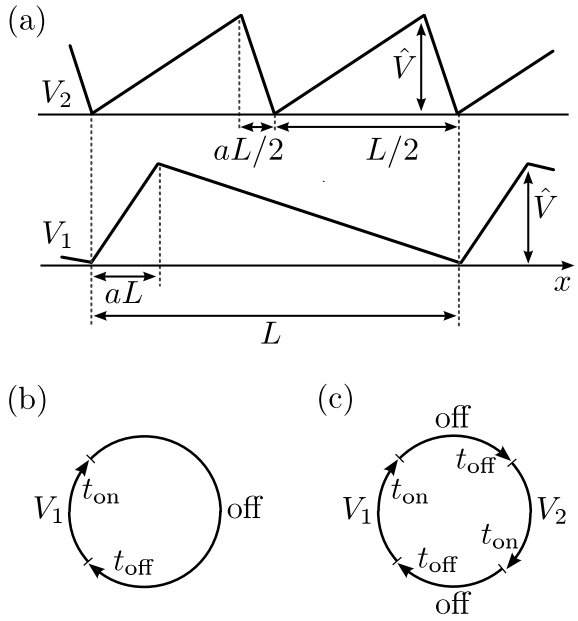

Figure 3.2: (a) Spatial characteristics of the potentials used in the extended on-off ratchet. Short-periodic sawtooth potential V_2 (top), long-periodic sawtooth potential V_1 (bottom). (b) Cycle of a simple on-off ratchet. (c) Cycle of the extended on-off ratchet.

time t_{on}, besides diffusion the particle drifts coherently toward a minimum of the sawtooth potential. The interplay of the diffusion and the coherent drift rectifies the motion of the particle. The magnitude of the mean displacement for an ensemble of particles is determined by the properties of the potential as well as by the diffusional behavior of the particles. In contrast, the direction of the mean displacement is exclusively determined by the value of the asymmetry parameter a.

In order to change the direction of the mean displacement with another property than the asymmetry of the sawtooth potential, the on-off ratchet needs to be extended. For this purpose, we add a second sawtooth potential V_2 to the ratchet cycle. The cycle of our proposed extended on-off ratchet is schematically depicted in panel (c) of Fig. 3.2. As illustrated in panel (a) of Fig. 3.2, the second potential V_2 is characterized by half the spatial period

$L/2$ and an inverse asymmetry parameter $(1-a)$. The two potentials are alternately activated with equal duration t_{on} and equal interjacent off-times t_{off}, so that the complete cycle lasts $T = 2t_{\mathrm{off}} + 2t_{\mathrm{on}}$. Due to their inverse asymmetries, the individual potentials induce drifts in opposite directions. In the extended on-off ratchet, both potentials are combined and the resulting direction of the mean displacement is no longer exclusively determined by the value of the asymmetry parameter a.

The extended on-off ratchet is fully characterized by the same four dimensionless parameters as the simple on-off ratchet. In analogy to Sec. 2.3.2, the motion of a particle can be described by dimensionless forms of the Langevin equation and the fluctuation-disspation theorem

$$\frac{\partial}{\partial \bar{t}}\,\bar{x} = \bar{V}\, f_a(\bar{x},\bar{t}) + \tilde{\xi}(\bar{t}), \tag{3.1}$$

$$\langle \bar{\xi}(\bar{t})\,\tilde{\xi}(\bar{t}')\rangle = 2\,\tilde{\delta}(\bar{t}-\bar{t}'). \tag{3.2}$$

Again we use the rescaled position $\bar{x} = x/L$, time $\bar{t} = t/t_{\mathrm{diff}}$, random force $\bar{\xi}(\bar{t}) = \xi(t)\,L/(k_{\mathrm{B}}T)$, and δ-function $\bar{\delta}(\bar{t}) = t_{\mathrm{diff}}\,\delta(t)$. The diffusion time scale $t_{\mathrm{diff}} = L^2/D$ is defined in analogy to Eq. (2.38). The time-dependent function $f_a(\bar{x},\bar{t})$ distinguishes the extended on-off ratchet from the simple model, as it carries the information about the ratchet cycle. When the potential is switched off, $f_a = 0$ and Eq. (3.1) describes a particle freely diffusing in one dimension. When the potential V_i $(i = 1, 2)$ is switched on, $f_a = -c_i/a$ and $f_a = c_i/(1-a)$ on the long and short slopes of the potential, respectively. The constant c_i takes the values $c_1 = 1$ and $c_2 = -2$. Again, the rescaled potential amplitude $\bar{V}$ is the Peclet number, denoting the relative significance of deterministic drift with respect to diffusional motion.

Also in analogy to the simple on-off ratchet, we rescale the periods of the ratchet cycle t_{on} and t_{off}. The off-time t_{off} is rescaled with respect to the diffusion time t_{diff},

$$\tau_{\mathrm{off}} = \frac{t_{\mathrm{off}}}{t_{\mathrm{diff}}}, \tag{3.3}$$

while the on-time t_{on} is rescaled with respect to the drift time t_{drift},

$$\tau_{\mathrm{on}} = \frac{t_{\mathrm{on}}}{t_{\mathrm{drift}}}, \tag{3.4}$$

resulting in the rescaled period $\bar{T} = 2(\tau_{\mathrm{off}} + \tau_{\mathrm{on}}/\bar{V})$ of one complete ratchet cycle. As discussed in Sec. 2.3.2, the rescaled off-time τ_{off} is a measure for the diffusivity of the particle during the off-time, while the rescaled on-time τ_{on} indicates whether the particle is able to reach the minima during the on-time.

In summary, the motion of a Brownian particle in the extended on-off ratchet depends on the rescaled off-time τ_{off}, the rescaled on-time τ_{on}, the asymmetry parameter a, and the Peclet number $\bar{V}$. In the subsequent sections, we calculate the mean displacement $\langle \Delta\bar{x} \rangle$ per ratchet cycle, as a function of these four dimensionless variables, where the Peclet number $\bar{V}$ will always be chosen much larger than one.

3.2.2 Numerical calculation of the mean displacement

In order to calculate the mean displacement for a wide range of parameters, we solve the Langevin equation (3.1) numerically. The simulations are based on the standard Euler method, which is sufficient in view of the simplicity of the potential. Following this method, the position $\bar{x}$ evolves during one time

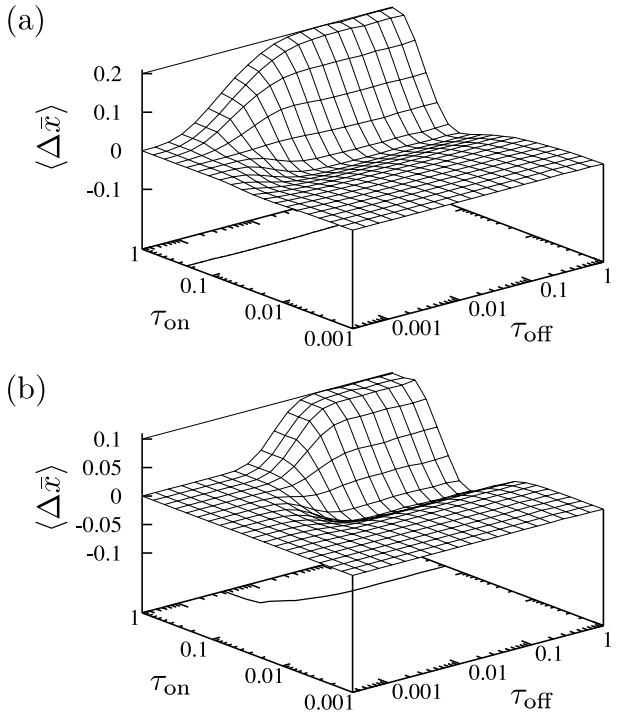

Figure 3.3: (a) Mean displacements $\langle \Delta \bar{x} \rangle$ obtained from a Brownian dynamics simulation with asymmetry $a = 0.1$ (b) As in panel (a), but for $a = 0.3$. The contour curves in the bottom planes correspond with $\langle \Delta \bar{x} \rangle = 0$. These curves with coordinates $\tau^*_{\rm off}$ and $\tau^*_{\rm on}$ trace the points of the direction reversal of the mean displacement.

step $\mathrm{d}\bar{t}$ according to

$$\bar{x}(\bar{t} + \mathrm{d}\bar{t}) = \bar{V} f_a(\bar{x}, \bar{t})\, \mathrm{d}\bar{t} + (2\, \mathrm{d}\bar{t})^{1/2}\, \mathrm{d}\bar{w}. \tag{3.5}$$

Here, $(2\, \mathrm{d}\bar{t})^{1/2}\, \mathrm{d}\bar{w}$ is the rescaled Wiener increment and $\mathrm{d}\bar{w}$ is a random number from a distribution with zero mean $\langle \mathrm{d}\bar{w} \rangle = 0$ and variance $\langle \mathrm{d}\bar{w}^2 \rangle = 1$ (see Sec. 2.5.4). To obtain sufficiently precise results, one million ratchet cycles were simulated for each combination of parameters.

The simulation results for the mean displacement $\langle \Delta \bar{x} \rangle$ with $\bar{V} = 1000$ and $a = 0.1$ and 0.3 are shown in panel (a) and (b) of Fig. 3.3, respectively. A common feature is that $\langle \Delta \bar{x} \rangle$ becomes vanishingly small in the limit $\tau_{\rm off} \to 0$

and $\tau_{\mathrm{on}} \to 0$. Furthermore, for large values of τ_{off} and τ_{on} the mean displacement approaches a maximum value $\langle \Delta\bar{x} \rangle_{\mathrm{max}}$. In Sec. 3.3.1, we will derive an analytical expression for $\langle \Delta\bar{x} \rangle_{\mathrm{max}}$. In contrast to the simple on-off ratchet, the extended model exhibits direction reversal. To be precise, the sign of $\langle \Delta\bar{x} \rangle$ now depends on the values of τ_{off} and τ_{on}. Two regions are observed, in which $\langle \Delta\bar{x} \rangle$ has opposite signs. The coordinates τ^*_{off} and τ^*_{on} of the curve which demarcates both regions depend on the value of the asymmetry parameter a.

In the following two sections, we will derive precise as well as approximative expressions for the mean displacement in different regions of the parameter space. Those expressions will enable us to predict direction reversal more quantitatively.

3.3 Method of discrete steps

To derive an analytic expression for the mean displacement $\langle \Delta\bar{x} \rangle$ in the case of large Peclet numbers $\bar{V}$, we apply the method of discrete steps as discussed in Sec. 2.3.2. This method is based on the assumption that the rescaled on-time τ_{on} is sufficiently large, so that a Brownian particle will always drift into a minimum when the sawtooth potentials are switched on. Hence, the trajectory of the particle can be mapped onto a sequence of effective steps between the locations of the potential minima. These steps occur with certain step probabilities. In Sec. 3.3.1, we apply the method of discrete steps to the extended on-off ratchet by incorporating the step probabilities corresponding to the additional ratchet potential. In Sec. 3.3.2, we successively extend the applicability of our method to smaller values of τ_{on} with the help of what we call the split-off approximation.

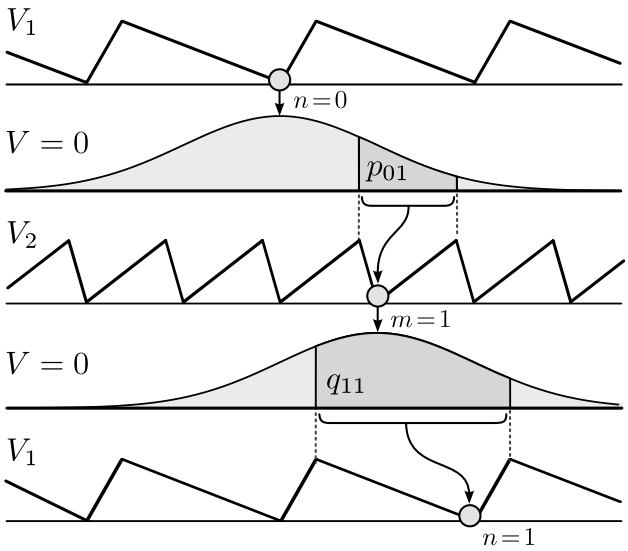

Figure 3.4: Schematic illustration of a complete cycle of the extended on-off ratchet in the discrete limit. For one possible step combination ($n = 0 \to m = 1 \to n = 1$) the graphical interpretation of the corresponding step probabilities p_{01} and q_{11} is visualized.

3.3.1 Discrete steps and their probabilities

For large Peclet numbers $\bar{V}$, Brownian motion can be neglected once the potential is switched on. As a result, a particle drifts uniformly towards a minimum. For the longer slope of potential V_1, the drift velocity is given by $v_{\text{drift}} = \hat{V}/[\gamma\,(1-a)L]$. Accordingly, the particle reaches the minimum for

$$t_{\text{on}} \geq \frac{(1-a)L}{v_{\text{drift}}} = (1-a)^2\, t_{\text{drift}}, \tag{3.6}$$

irrespective of its position at the time the potential is switched on. With the definition of the rescaled on-time τ_{on} in Eq. (3.4), the latter condition can be expressed as

$$\tau_{\text{on}} \geq (1-a)^2. \tag{3.7}$$

Particles drifting under the influence of the shorter slope of potential V_1 as well as both slopes of potential V_2 also reach the minimum, provided Eq. (3.7) is satisfied. Accordingly, after each application of the potential, all particles are located at the minima of either V_1 or V_2. A single particle hence performs discrete steps along the x-axis, provided its trajectory is sampled at the end of each on-time. The minima of the potential V_1 are labeled with the integer n , so that the corresponding positions are given by $\bar{x}_n = n$. For the potential V_2, the minima are labeled with m and the positions are $\bar{x}_m = m/2$, because V_2 has half the spatial periodicity.

Now, we consider the probability p_{nm} for a step performed by a single particle from the minimum n of V_1 to the minimum m of V_2, as illustrated in Fig. 3.4. When the potential is switched off the particle diffuses freely, starting from $\bar{x}_\mathrm{S} = n$. In our rescaled units, the probability density to reach the position $\bar{x}$ at the end of the off-time is given by the Gaussian distribution

$$\mathcal{P}(\bar{x}) = \frac{1}{\sqrt{4\pi\tau_\mathrm{off}}} \exp\left(-\frac{(\bar{x}-\bar{x}_\mathrm{S})^2}{4\tau_\mathrm{off}}\right). \tag{3.8}$$

Note that the width of this distribution is exclusively determined by the value of the rescaled off-time τ_off. In order to drift to the minimum m of potential V_2 during the subsequent on-time, the particle needs to diffuse into the interval $(m-a)/2 < \bar{x} < (m+1-a)/2$ situated between the neighboring maxima of minimum m. Accordingly, the step probability is given by integrating $\mathcal{P}(\bar{x})$, so that

$$p_{nm} = \int_{\frac{1}{2}(m-a)}^{\frac{1}{2}(m+1-a)} \frac{d\bar{x}}{\sqrt{4\pi\tau_\mathrm{off}}} \exp\left(-\frac{(\bar{x}-n)^2}{4\tau_\mathrm{off}}\right). \tag{3.9}$$

In a similar way, we derive the probability q_{mn} for a step from the minimum m of V_2 to the minimum n of V_1. Now, the initial minimum is located at

$\bar{x}_{\mathrm{S}} = m/2$ and the interval between the maxima around minimum n of V_1 is given by $(n-1+a) < \bar{x} < (n+a)$. Hence, the step probability takes the form

$$q_{mn} = \int_{n-1+a}^{n+a} \frac{d\bar{x}}{\sqrt{4\pi\tau_{\mathrm{off}}}} \exp\left(-\frac{(\bar{x}-m/2)^2}{4\tau_{\mathrm{off}}}\right). \tag{3.10}$$

The mean displacement $\langle\Delta\tilde{x}\rangle$ is calculated for a complete ratchet cycle. Due to the spatial periodicity of the system, one can always place the initial minimum at $n = 0$. By averaging over all possible step combinations, we arrive at

$$\langle\Delta\tilde{x}\rangle = \langle n\rangle = \sum_n \sum_m n \cdot p_{0m}\, q_{mn}. \tag{3.11}$$

Note that in the discrete limit the mean displacement $\langle\Delta\bar{x}\rangle$ only depends on the values of the asymmetry parameter a and the rescaled off-time τ_{off}.

We now discuss the limiting behavior of the mean displacement $\langle\Delta\bar{x}\rangle$ for small and large values of τ_{off}. For small values of τ_{off}, the mean displacement approaches zero, because the step probabilities to neighboring minima become vanishingly small. For large values of τ_{off}, the mean displacement takes its maximum value $\langle\Delta\bar{x}\rangle_{\max}$. An algebraical expression for $\langle\Delta\bar{x}\rangle_{\max}$ can be derived on the basis that the probability profile between two maxima becomes approximately homogeneous for large values of τ_{off}. The fractions of the particles experiencing the larger and shorter slopes of potential V_1 are given by $(1-a)$ and a, respectively. The corresponding mean displacements of these fractions are $(1-a)/2$ and $-a/2$. The total mean displacement induced by potential V_1 is given by the weighed average of both fractions, so that $\langle\Delta\bar{x}_1\rangle = (1/2) - a$. The mean displacement induced by V_2 can be derived in the same way and yields $\langle\Delta\bar{x}_2\rangle = -\langle\Delta\bar{x}_1\rangle/2$. For the complete cycle, the mean displacement is

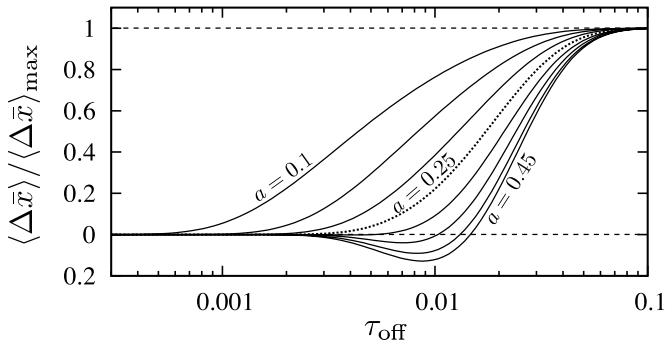

Figure 3.5: Normalized mean displacement $\langle\Delta\bar{x}\rangle/\langle\Delta\bar{x}\rangle_{\max}$ in the extended on-off ratchet versus the rescaled off-time $\tau_{\rm off}$. The curves have been calculated in the discrete limit. From top to bottom, $a = 0.1$, 0.15, 0.2, 0.25, 0.3, 0.35, 0.4 and 0.45. The dashed line with $a = 0.25$ indicates the onset of direction reversal in an intermediate range of values for $\tau_{\rm off}$.

given by the sum $\langle\Delta\bar{x}\rangle = \langle\Delta\bar{x}_1\rangle + \langle\Delta\bar{x}_2\rangle$, so that

$$\langle\Delta\bar{x}\rangle_{\max} = \lim_{\tau_{\rm off}\to\infty}\langle\Delta\bar{x}\rangle = \frac{1}{2}\left(\frac{1}{2} - a\right). \tag{3.12}$$

Note that this expression is only valid for sufficiently large values of the rescaled on-time $\tau_{\rm on} \geq (1-a)^2$.

We have obtained the mean displacement for a series of a values in the range $0.1 < a < 0.45$ by numerical evaluation of Eq. (3.11). The normalized values $\langle\Delta\bar{x}\rangle/\langle\Delta\bar{x}\rangle_{\max}$ with $\langle\Delta\bar{x}\rangle_{\max}$ obtained from Eq. (3.12) are displayed in Fig. 3.5 as a function of the rescaled off-time $\tau_{\rm off}$. For values of $\tau_{\rm off}$ exceeding 0.1, the normalized mean displacement approaches unity. This confirms the predicted limiting behavior given by Eq. (3.12). For values of $a > 0.25$, the normalized mean displacement becomes negative in an intermediate range of values of $\tau_{\rm off}$, *i.e.*, the mean displacement changes its direction. The resulting minimum becomes more pronounced for larger values of a. Note that $\langle\Delta\bar{x}\rangle_{\max}$ decreases linearly with a and reaches $\langle\Delta\bar{x}\rangle_{\max} = 0$ in the symmetric case with

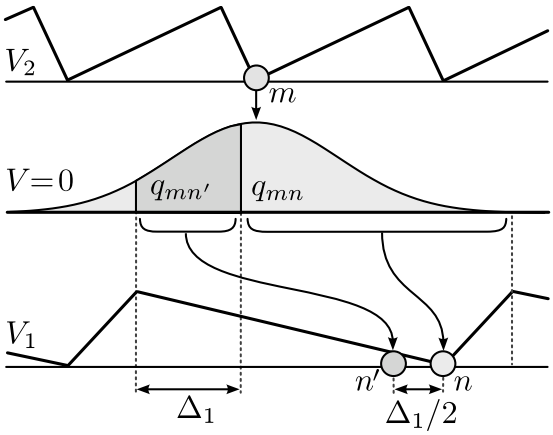

Figure 3.6: Illustration of the split-off approximation on the longer slope of potential V_1. Particles corresponding with the dark gray colored part of the diffusion profile fail to reach the minimum n during the on-time and will start the subsequent off-time from the split-off point n'.

$a = 0.5$. Accordingly, the minimum in the (unnormalized) mean displacement $\langle \Delta\bar{x} \rangle$ vanishes in the limit $a = 0.5$.

3.3.2 Split-off approximation

We now extend the method of discrete steps to values of τ_{on} smaller than $(1-a)^2$, *i.e.*, not all particles will drift into a minimum of either potential V_1 or V_2 during the on-time. For now, we restrict ourselves to the situation, where the particles on the longer slope of V_1 do not necessarily reach a minimum, but on the smaller slope and when potential V_2 is switched on they do. This situation corresponds to $(1-a)^2/4 < \tau_{\text{on}} < (1-a)^2$.

We consider an ensemble of particles at a time right before the potential V_1 is switched on. Particles on the right-hand side of each maximum will not reach a minimum if they are located in a spatial region with a width Δ_1 as illustrated in Fig. 3.6. We will call Δ_1 the *split-off* parameter in the following. With the help of the drift velocity on the longer slope of V_1 and the length

$(1-a)L$ of this slope, one is able to calculate the split-off parameter

$$\Delta_1 = \max\left[0,\, (1-a)\left(1 - \frac{\tau_{\mathrm{on}}}{(1-a)^2}\right)\right]. \tag{3.13}$$

In order to apply the method of discrete steps, we assume that *all* particles in the region Δ_1 drift to a *single* split-off point n'. As illustrated in Fig. 3.6, this split-off point is located at a distance $-\Delta_1/2$ from the minimum with index n. The locations of the split-off points are hence given by $\bar{x}_{n'} = n - \Delta_1/2$.

For $\tau_{\mathrm{on}} < (1-a)^2/4$, we introduce additional split-off points on the longer slope of potential V_2. They are located at $\bar{x}_{m'} = (m+\Delta_2)/2$ where m indicates the minima of V_2. Particles in a certain region at the left-hand side of the maxima are not able to reach the minima of potential V_2. The width of this region Δ_2 is given by

$$\Delta_2 = \max\left[0,\, \frac{(1-a)}{2}\left(1 - \frac{\tau_{on}}{\frac{1}{4}(1-a)^2}\right)\right]. \tag{3.14}$$

Obviously, our split-off approximation will result in a progressively worse estimation of the mean displacement for smaller values of τ_{on} and, implicitly, larger values of Δ_1 and Δ_2.

We can derive an expression for the mean displacement in the same manner as in Sec. 3.3.1. Now we need to consider eight step probabilities. They are obtained by integrating over the corresponding sections of the diffusion profile. The split-off points are taken into account by a modification of the starting points x_{S} in Eq. (3.8) and the integration limits in Eqs. (3.9, 3.10). Furthermore, in the expression for the mean displacement one has to introduce the respective probabilities P and P' for a particle to occupy either a minimum or the corresponding split-off point at the beginning of each cycle. Due to

the spatial periodicity of the ratchet, these probabilities do not depend on the particular location n of the potential well. To determine $P(\bar{t}_0 + \bar{T})$ and $P'(\bar{t}_0 + \bar{T})$ from $P(\bar{t}_0)$ and $P'(\bar{t}_0)$ after one full ratchet cycle with period $\bar{T}$, one has to consider all possible step combinations during such a cycle. Without loss of generality, all these step combinations are generated when one starts from the minimum at $n = 0$ or the split-off point at $0'$. Therefore the probabilities P and P' evolve in time according to

$$\begin{aligned} P(\bar{t}_0 + \bar{T}) &= P(\bar{t}_0) \sum_{m,n} (p_{0m}\, q_{mn} + p_{0m'}\, q_{m'n}) + \\ &\quad P'(\bar{t}_0) \sum_{m,n} (p_{0'm}\, q_{mn} + p_{0'm'}\, q_{m'n}) \qquad (3.15) \\ P'(\bar{t}_0 + \bar{T}) &= P(\bar{t}_0) \sum_{m,n} (p_{0m}\, q_{mn'} + p_{0m'}\, q_{m'n'}) + \\ &\quad P'(\bar{t}_0) \sum_{m,n} (p_{0'm}\, q_{mn'} + p_{0'm'}\, q_{m'n'}). \qquad (3.16) \end{aligned}$$

We are interested in the steady state solution, $P(\bar{t}_0 + \bar{T}) = P(\bar{t}_0)$ and $P'(\bar{t}_0 + \bar{T}) = P'(\bar{t}_0)$, which yields

$$\begin{aligned} \frac{P'}{P} &= \frac{1 - \sum_{m,n} (p_{0m}\, q_{mn} + p_{0m'}\, q_{m'n})}{\sum_{m,n} (p_{0'm}\, q_{mn} + p_{0'm'}\, q_{m'n})} \\ &= \frac{\sum_{m,n} (p_{0m}\, q_{mn'} + p_{0m'}\, q_{m'n'})}{1 - \sum_{n,m} (p_{0'm}\, q_{mn'} + p_{0'm'}\, q_{m'n'})}. \qquad (3.17) \end{aligned}$$

Together with the normalization constraint $P + P' = 1$, the probabilities P and P' are fully determined from either one of the conditions in Eq. (3.17). The mean displacement can now be derived by averaging over all possible step combinations (including the split-off points n' and m') and takes the following

form

$$\langle \Delta \bar{x} \rangle = \sum_{n,m} n \, [(P \, p_{0m} + P' \, p_{0'm}) \, (q_{mn} + q_{mn'}) + \\ + (P \, p_{0m'} + P' \, p_{0'm'}) \, (q_{m'n} + q_{m'n'})] \, . \tag{3.18}$$

Here we approximate the step length by n, irrespective of whether the step starts or ends in a minimum or split-off point. Note that the mean displacement now depends on the parameters $\tau_{\rm on}$, $\tau_{\rm off}$, and a. In particular, the rescaled on-time $\tau_{\rm on}$ enters through the values of the parameters Δ_1 and Δ_2 in the step probabilities. For $\tau_{\rm on} \geq (1-a)^2$, $\Delta_1 = \Delta_2 = 0$ and Eq. (3.18) reduces to the corresponding Eq. (3.11) pertaining to discrete behavior.

We have obtained the mean displacement $\langle \Delta \bar{x} \rangle$ according to the split-off approximation by numerical evaluation of Eq. (3.18) for $\tau_{\rm off} = 1$ and $a = 0.1$ and 0.3. The results are displayed in Fig. 3.7 as a function of the rescaled on-time $\tau_{\rm on}$. For the sake of comparison, we have also included the corresponding values following from the Brownian dynamics simulation. The maximum value $\langle \Delta \bar{x} \rangle_{\rm max}$, as given by Eq. (3.12), is recovered for $\tau_{\rm on} > (1-a)^2$. Note that the value $\tau_{\rm off} = 1$ is sufficiently large for the application of Eq. (3.12) (see *e.g.* Fig. 3.5). With decreasing values of $\tau_{\rm on}$, the mean displacement decreases and changes sign at a critical value of the rescaled on-time $\tau_{\rm on}^*$. Irrespective of the value of the asymmetry parameter a, the prediction based on the split-off approximation is in perfect agreement with the results of the Brownian dynamics simulations in the range $(1-a)^2/4 < \tau_{\rm on} < (1-a)^2$. The prediction even reproduces the behavior of $\langle \Delta \bar{x} \rangle$ for smaller values of the rescaled on-times (with deviations for $a = 0.3$). In particular, for the present combination of parameters, the split-off approximation is sufficient to predict the point of

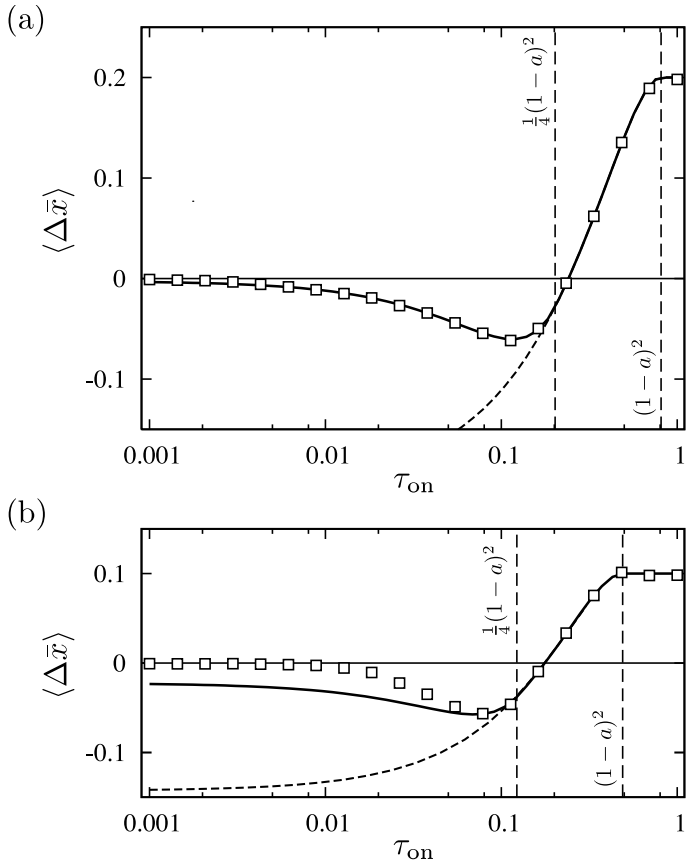

Figure 3.7: (a) Mean displacement $\langle \Delta \bar{x} \rangle$ in the extended on-off ratchet versus the rescaled on-time $\tau_{\rm on}$ for a rescaled off-time $\tau_{\rm off} = 1.0$ and asymmetry parameter $a = 0.1$. The solid curve refers to the results from the split-off approximation, whereas the symbols indicate the results from the Brownian dynamics simulations. The dashed curve refers to the results from the split-off approximation with $\Delta_2 = 0$ for all values of $\tau_{\rm on}$. The vertical dashed lines indicate the onset of the discrete regime at $\tau_{\rm on} = (1-a)^2$ and the threshold of the split-off approximation with $\Delta_2 = 0$ at $\tau_{\rm on} = (1-a)^2/4$. (b) As in panel (a), but for asymmetry parameter $a = 0.3$.

direction reversal $\tau_{\rm on}^*$.

In order to compare the predictions based on the split-off approximation with the relevant results of the Brownian dynamics simulations for values of $\tau_{\rm off}$ smaller than 1, we now consider the points of direction reversal of the mean displacement with coordinates $\tau_{\rm off}^*$ and $\tau_{\rm on}^*$ (*i.e.*, those coordinates for which

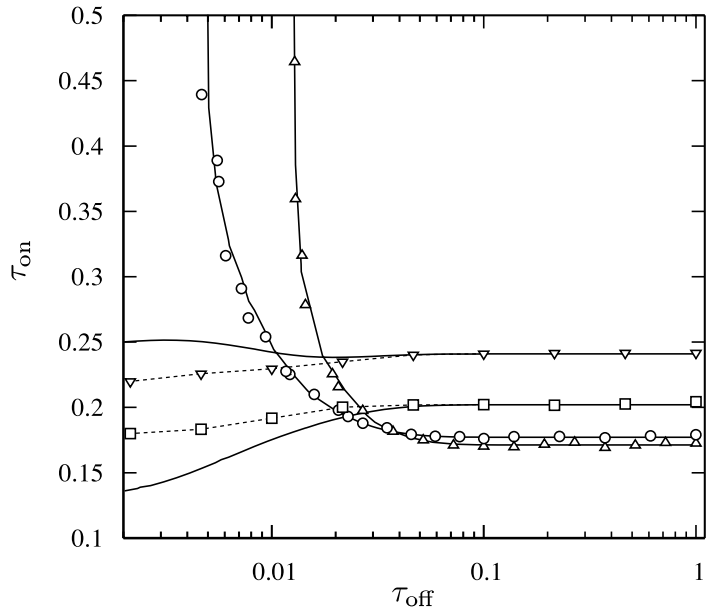

Figure 3.8: Contour curves for $\langle \Delta \bar{x} \rangle = 0$. These curves trace the points of direction reversal of the mean displacement with coordinates $\tau^*_{\rm off}$ and $\tau^*_{\rm on}$. The symbols refer to Brownian dynamics simulation results with asymmetry parameters $a = 0.1$ ($\triangledown$), $a = 0.2$ ($\square$), $a = 0.3$ ($\circ$) and $a = 0.4$ ($\triangle$). The solid curves represent the corresponding predictions based on the split-off approximation. The dashed curves serve as a guide to the eye. Notice that the latter predictions deviate from the simulation results for $a < 0.3$ and $\tau^*_{\rm off} < 0.05$.

$\langle \Delta \bar{x} \rangle = 0$). The corresponding contour curves following from the simulations as well as from the split-off approximation are displayed in Fig. 3.8 for some typical values of the asymmetry parameter a. The predictions of the points of direction reversal based on the split-off approximation are in perfect agreement with the simulation results for the larger values of the asymmetry parameter $a = 0.3$ and 0.4, irrespective the value of the rescaled off-time $\tau_{\rm off}$. In the case of smaller values of a, *i.e.* for $a = 0.1$ and 0.2, the split-off approximation only gives accurate results for a sufficiently large value of $\tau_{\rm off} > 0.05$. Furthermore, it should be noticed that for $\tau_{\rm off} > 0.1$, the point of direction reversal of the mean displacement $\tau^*_{\rm on}$ occurs at a constant but a dependent value, irrespective of the value of $\tau_{\rm off}$.

The split-off approximation also allows the calculation of the mean displacement $\langle \Delta \bar{x} \rangle$ for large values of τ_{off} (in practice for $\tau_{\text{off}} > 0.1$). In the same way as for the derivation of Eq. (3.12), we obtain

$$\lim_{\tau_{\text{off}} \to \infty} \langle \Delta \bar{x} \rangle = \frac{1}{2} \left(\frac{1}{2} - a \right) - \frac{1}{2} \Delta_1^2 + \Delta_2^2. \tag{3.19}$$

In the case of discrete behavior with $\Delta_1 = \Delta_2 = 0$, the latter expression correctly reduces to Eq. (3.12) for $\tau_{\text{on}} \geq (1-a)^2$. Furthermore, Eq. (3.19) allows the derivation of an expression for the point of direction reversal τ_{on}^*. We first solve $\lim_{\tau_{\text{off}} \to \infty} \langle \Delta \bar{x} \rangle = 0$ for the split-off parameter Δ_1 with $\Delta_2 = 0$ and use Δ_1 in Eq. (3.13) to calculate the rescaled on-time

$$\tau_{\text{on}}^* = (1-a)^2 \left[1 - \left(\frac{\frac{1}{2} - a}{(1-a)^2} \right)^{1/2} \right]. \tag{3.20}$$

Note that in the limit of $\tau_{\text{off}} \to \infty$, the value of τ_{on}^* only depends on the asymmetry parameter a. The predicted values for τ_{on}^* are displayed in Fig. 3.9 as a function of the asymmetry parameter a. Excellent agreement with the corresponding results from the Brownian dynamics simulations is observed for $a < 0.45$. Furthermore, we note that the predicted values for τ_{on}^* fall within the region $\tau_{\text{on}} > (1-a)^2/4$, where the split-off approximation applies for $\Delta_2 = 0$. Our *a priori* choice of $\Delta_2 = 0$ is hence justified.

In principle, the split-off approximation can be carried to higher levels by including split-off points on all slopes. We have however refrained from doing so, because the mathematical expressions become rather involved and there is not much gain in physical insight. Furthermore, very small values of τ_{on} are of little interest from a practical point of view, because the corresponding mean displacements are vanishingly small.

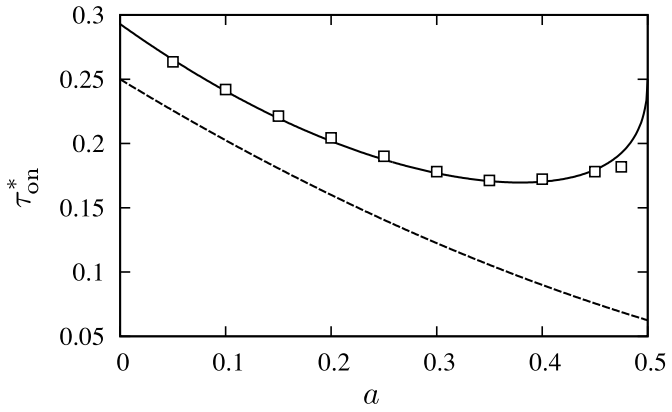

Figure 3.9: Points of direction reversal of the mean displacement $\tau^*_{\rm on}$ versus the asymmetry parameter a. The solid curve represents the prediction based on the split-off approximation in the limit of large values of $\tau_{\rm off}$. The symbols refer to the corresponding results from the Brownian dynamics simulations. The dashed curve demarcates the region $\tau_{\rm on} > (1-a)^2/4$, where the split-off approximation with $\Delta_2 = 0$ applies.

3.4 Particle separation

In the extended on-off ratchet the magnitude and the direction of the mean displacement can be varied by adjusting the parameters $\tau_{\rm off}$ and $\tau_{\rm on}$. In the following, we discuss how this feature can be exploited to reduce the size of microfluidic separation devices. Here, our objective is to translate the parameters of the extended on-off ratchet model to real design parameters. In particular, we will explore how we can experimentally control the magnitude and direction of the mean displacement of the particles.

3.4.1 Design parameters

We propose two possible designs for microfluidic devices. In the first design depicted in Fig. 3.10 (a), every second row of the obstacles in the classical array is replaced by a row of obstacles with half the spatial periodicity and inverse asymmetry. The particles are driven in y-direction through the device

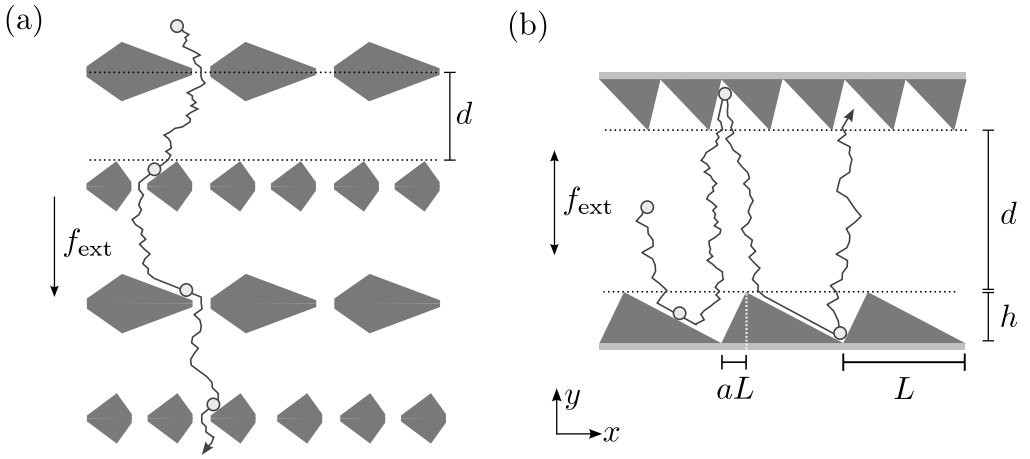

Figure 3.10: Microfluidic devices for particle separation that benefit from the effect of direction reversal. (a) A microfluidic array device. The solid line represents an example trajectory of a particle driven by a constant external force f_{ext}. The gray objects refer to the obstacles. (b) As in panel (a), but for a microfluidic channel device. The particles are driven by a periodically inverted external force back and forth across the channel.

with the help of an external force f_{ext} and they alternately interact with the two types of rows of obstacles. In the second proposed design depicted in Fig. 3.10 (b), the sawtooth shaped obstacles line the opposing walls of a single channel. Here, the particles are driven back and forth between the walls with the help of a periodically inverted external force f_{ext}. In both devices, the spatial extensions of the obstacles in x- and y-direction are given by L and h, respectively, whereas the asymmetry with respect to y-axis is determined by the parameter a.

Before we discuss particle separation, we need to define the time scales for diffusion and drift. For a particle with a mobility μ reacting on an external force f_{ext}, the velocity is given by $v = \mu\, f_{\text{ext}}$. In contact with an obstacle, the direction of the velocity changes and acquires a component v_x in the direction perpendicular to the external force. Assuming that the face of the obstacle is tilted by the angle $\theta = (1 - a)L/h$ from the direction of the external force,

the transverse component amounts to $v_x(\theta) = v \sin\theta \cos\theta$.[4] We now introduce the largest possible tilt angle $\theta_{\max} = \arctan(L/h)$ for obstacles with $a = 0$, and define the characteristic drift time $t_{\text{drift}} = L/v_x(\theta_{\max})$ in full analogy to Eq. (2.50). The diffusion time $t_{\text{diff}} = L^2/D$ remains the same as in the ratchet model and the Peclet number hence reads $t_{\text{diff}}/t_{\text{drift}} = L\, v_x(\theta_{\max})/D$. Accordingly, the latter can be tuned by adjusting the strength of the external force.

3.4.2 Separation in array devices

We now map the dynamics of particles in the array device with alternating rows (see panel (a) of Fig. 3.10) onto our extended on-off ratchet. Since the particles always have to pass the gaps between the obstacles, their motion can be described by the method of discrete steps. The parameters are mapped in analogy to Sec. 2.4.2, where the separation dynamics in a conventional array have been mapped onto the simple on-off ratchet. The off-time of the ratchet is determined by the time the particles need to cross the distance d between the rows under the influence of the external force and is given by $t_{\text{off}} = d/v$. Accordingly, the value of t_{off} and hence the rescaled off-time

$$\tau_{\text{off}} = \frac{dD}{\mu f_{\text{ext}} L^2} \tag{3.21}$$

can experimentally be tuned by adjusting the external force f_{ext}. Suppose that a suspension contains two types of particles A and B with different values for D/μ. In order to separate these particles in an array with a rescaled off-time for direction reversal τ^*_{off}, the rescaled off-times pertaining to the two types of

[4] We consider the longer face of the obstacles and therefore derive a lower bound for the Peclet number. Further we restrict the discussion to $a < 0.5$.

particles have to be tuned such that $\tau_{\mathrm{off,A}} > \tau^*_{\mathrm{off}} > \tau_{\mathrm{off,B}}$. As a consequence, the induced mean displacements in x-direction have opposite signs, to be precise $\langle \Delta\bar{x} \rangle_{\mathrm{A}} > 0 > \langle \Delta\bar{x} \rangle_{\mathrm{B}}$. In line with Ref. [29], the device can be operated in combination with a periodic reversal of the direction of the external force. In this case, both particle types move periodically back and forth in y-direction. However, particles of type A move in average to the right ($\langle \Delta\bar{x} \rangle_{\mathrm{A}} > 0$), while particles of type B move to the left ($\langle \Delta\bar{x} \rangle_{\mathrm{B}} < 0$). Hence, only a few rows of obstacles are necessary and the device can be downsized in y-direction without reducing the resolution of the separation process.

The methods presented in Sec. 3.3.1 can be used to determine the value of τ^*_{off} for a device specific value of the asymmetry parameter a. For the design of the obstacle it is crucial, that the value of a exceeds 0.25 in order to observe direction reversal of the mean displacement (see Fig. 3.5).

3.4.3 Separation in channel devices

Rather than driving the particles through subsequent rows of obstacles, the particles can be driven back and forth between the two opposing walls of a channel with the help of a periodically inverted external force (see panel (b) of Fig. 3.10). Note that the external force is applied perpendicular to the direction of the channel. We will now demonstrate that such channel operates in four different regimes depending on the inversion periods of the external force. Each regime requires a different mapping of the particle dynamics onto a ratchet model. We define the time periods T_+ and T_- to indicate the periods over which the external force points up and downwards, *i.e.* in the positive and negative y-direction, respectively.

For a simplified analysis of the channel device, we set $T_+ \gg d/v$. As a

consequence, the particles always reach the upper wall of the channel, meaning that they completely drift into the grooves of the sawtooth profile. The performance of the proposed device now depends on the period T_- of the pulsed external force, the distance between the rows d, the height of the sawtooth profiles h, and the velocity of the particles v. Four different regimes can be identified. In the first regime with $T_- < h/v$, the particles are trapped within one spatial period of the upper row of obstacles and no mean displacement occurs. Note that the limits of the four regimes, which we present here, are approximate values because of the Brownian motion in y-direction. In the second regime with $h/v < T_- < (d+h)/v$, the particles only interact with the upper row of obstacles. Hence the channel functions as a simple on-off ratchet. The value of the induced mean displacement is determined by the off-time $t_{\text{off}} \approx 2(T_- - h/v)$ and is negative due to the inverse asymmetry of the profile. For sufficiently large values of t_{off}, the displacement is given by $\langle \Delta\bar{x} \rangle = -(1/2 - a)/2$ (see Eq. (2.62)). In the third regime with $(d+h)/v < T_- < (d+2h)/v$, the particles interact with both rows of obstacles, however, they will not always drift into the grooves of the sawtooth profile of the lower wall before their electrophoretic direction is reversed by switching the external force. In this regime, the mean displacement can approximately be described by the split-off approximation of the extended on-off ratchet. The off-time is determined by the time the particles need to cross the distance d between the upper and lower rows. Hence, the rescaled off-time is given by Eq. (3.21). The time during which the particles are in contact with the lower row of obstacles determines the on-time $t_{\text{on}} \approx T_- - (d+h)/v$. Its rescaled value

$$\tau_{\text{on}} = \sin\theta_{\max} \cos\theta_{\max} \, \frac{\mu f_{\text{ext}} \, T_- - (d+h)}{L} \tag{3.22}$$

can be tuned by adjusting the product $f_{\text{ext}}T_-$ properly. Note that in this regime changes in T_- only affect τ_{on} whereas τ_{off} remains constant. In the fourth regime with $T_- > (d+2h)/v$, the particles always reach the walls of the channel before their velocity changes direction. In this regime, the channel is equivalent to our array device proposed priorly.

The equations derived under the split-off approximation require minor modification in order to describe the mean displacement in the third regime. For given values of h and L, we have already defined the maximum tilt angle $\theta_{\max} = \arctan(L/h)$. It occurs for asymmetry parameter $a = 0$. For nonzero a we define the tilt angle of the longest slope of the two obstacles, $\theta_a < \theta_{\max}$. Compared to the drift velocity induced by the sawtooth potential, the velocity $v_x(\theta_a)$ exhibits a different dependence on the asymmetry parameter a and the adjusted split-off parameter Δ_1 now reads

$$\Delta_1 = (1-a) - \tau_{\text{on}} \frac{v_x(\theta_a)}{v_x(\theta_{\max})}. \tag{3.23}$$

Due to our choice for T_+, the second split-off parameter $\Delta_2 = 0$ is zero.

3.4.4 Simulation of a single point-like particle

We performed two-dimensional Brownian dynamics simulations of a single point-like particle in the proposed channel device. The interaction between the particle and the walls was modeled with a short-ranged repulsive potential V_{wall}. For a reduced particle-wall distance $\bar{r}$ in units of L, the potential is given by $V_{\text{wall}}(\bar{r})/k_{\text{B}}T = (\bar{r}/b)^{-12}$ with $b = 1.25 \cdot 10^{-3}$. The asymmetry parameter and the reduced lengths of the channel geometry were set to $a = 0.1$, $\bar{h} = 0.1$, $\bar{d} = 4$, and the Peclet number was chosen as $t_{\text{diff}}/t_{\text{drift}} \approx 20$. Figure 3.11 shows

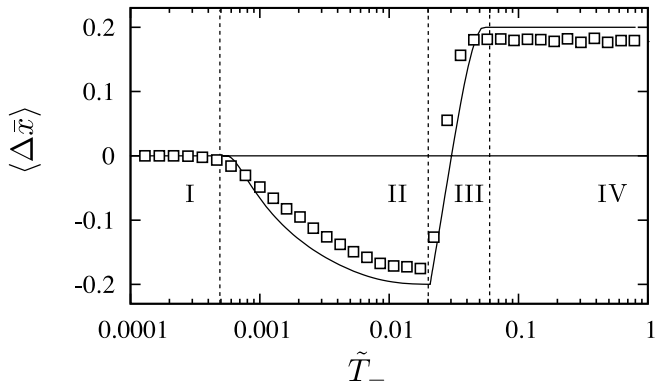

Figure 3.11: Mean displacement $\langle \Delta \bar{x} \rangle$ of a particle in a channel device as a function of the reduced time period $\bar{T}_-$ in units of t_{diff}. The geometry of the channel is defined by the asymmetry parameter $a = 0.1$ and the reduced lengths $\bar{h} = 0.1$ and $\bar{d} = 4$ in units of L. The symbols refer to results from two-dimensional Brownian dynamics simulations. The solid line refers, respectively, to predictions from the conventional and the extended on-off ratchet model. The vertical lines demarcate the different operational regimes of the channel device, as discussed in the text.

the mean displacement $\langle \Delta \bar{x} \rangle$ as a function of the reduced period $\bar{T}_-$ in units of t_{diff}. We have demarcated the four regimes with increasing $\bar{T}_-$ as discussed above. In each regime, the results of the simulations are compared to the predictions of the corresponding model, *i.e.*, zero-displacement in regime I, simple on-off ratchet in II, extended on-off ratchet with non-discrete behavior in III, and extended on-off ratchet with discrete behavior in IV, respectively. In all four regimes the predictions are in good agreement with the results from the simulations. Most of all, the reversal of the drift direction in the third regime is correctly predicted by the extended on-off ratchet within the split-off approximation. Deviations between the extended ratchet model and the simulation data are due to four main reasons. First, the one-dimensional model neglects diffusion of the particle in y-direction. Second, the model does not take into account that on- and off-times depend on the exact position of

the particle at times when the external force is reversed. Third, the model assumes that the particles can diffuse freely in x-direction even in the vicinity of the obstacles. Fourth, the simulations were performed for Peclet number $t_{\text{diff}}/t_{\text{drift}} \approx 20$, whereas the model refers to $t_{\text{diff}}/t_{\text{drift}} \gg 1$. Although the extended ratchet model is a simplification of the actual particle dynamics in the channel geometry, it offers a fairly good prediction of the mean displacements.

3.4.5 Simulation of finite-size particles

In this section, we investigate more realistic systems consisting of particles with finite size. For that purpose, we use a two-dimensional version of the simulation algorithm introduced in Sec. 2.5.4. Hydrodynamic interactions are neglected, since the channel geometry is too complex in order to be taken into account properly.[5]

We now discuss the behavior of two distinct types of particles within the channel. For that purpose, we simulated 40 spherical particles within a cell with three spatial periods L and periodic boundary conditions in x-direction. 20 particles have a rescaled radius of $\bar{\sigma} = 0.01$ and the other 20 particles have $\bar{\sigma} = 0.02$. According to Stokes' law in Eq.(2.10), the small particles move two times faster than the large ones. The channel parameters were set to $a = 0$, $\bar{h} = 0.3$, $\bar{d} = 2$ and the Peclet number was chosen as $t_{\text{diff}}/t_{\text{drift}} \approx 20$. For each particle type the induced mean displacement is depicted in Fig. 3.12 as a function of $\bar{T}_-$. Both particle types show the characteristic direction reversal, but the positions of the direction reversal are shifted and the amplitudes are smaller than expected for $a = 0$.[6] The shift is caused by the different drift

[5]The Rotne-Prager approximation for hydrodynamic interactions is only valid for unbound fluids, which is clearly not the case in the considered channel design.

[6]For $a = 0$, the extended on-off ratchet model predicts a maximum mean displacement of

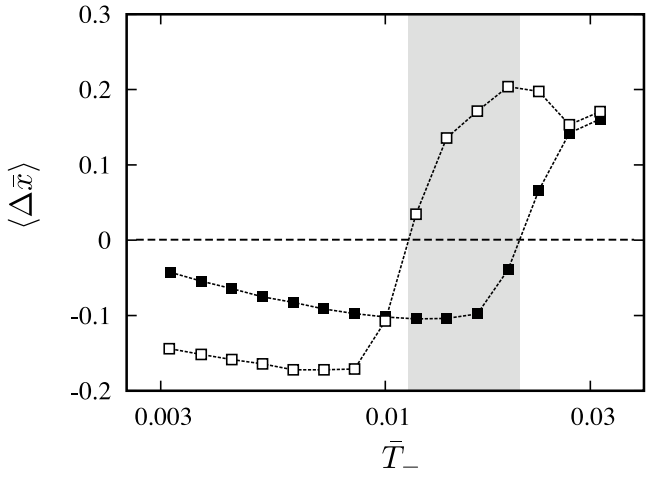

Figure 3.12: Mean displacement as a function of the time period T_- for two particle types. The empty symbols refer to data for particles with rescaled radius $\bar{\sigma} = 0.01$ while full symbols refers to particles with radius $\bar{\sigma} = 0.02$. The geometry of the channel is defined by the asymmetry parameter $a = 0$ and the reduced lengths $\bar{h} = 0.3$ and $\bar{d} = 2$. The grey area indicates the interval for T_- where particle of different type are displaced towards opposite directions.

times of both particle types. The smaller particles reach the opposite wall earlier than the larger particles. Therefore, their mean displacement changes the direction for smaller values of $\bar{T}_-$. The observed shift of the curves is crucial for the separation of both types of particles. The gray area marks the interval for $\bar{T}_-$ in which the mean displacements of both particle types have opposite signs. If the device parameters are adjusted such that the resulting value for $\bar{T}_-$ lies within this interval, small particles will move in average to the right, while large particles will move to the left.

In oder to demonstrate separation of two particle types, we repeated the

0.25 in both directions for a single particle. The reduced mean displacements originate from the behavior of the particles in the grooves of the sawtooth profiles. Given sufficient drift time, a single particle will always reach the grooves of the corresponding wall. For larger particle numbers, the groove might already be occupied by some other particle. In this case, particles start from a position slightly displaced from the position of the groove when the field changes its direction. Due to the asymmetry of the sawtooth profile, particles are displaced in average towards the longer slope. This decreases the relevant stepping probabilities and hence leads to the observed reduction of the mean displacements.

previous simulation but in a channel with four spatial periods and closed boundaries. To be precise, the channel is confined by two vertical walls on both sides as illustrated in Fig, 3.13 (a). Further, with $T_- = 0.02$ we choose the period $\bar{T}_-$ such that induced mean displacements have opposite signs for the considered particle types (gray area in Fig. 3.12). Initially, the particles are homogeneously distributed within the channel. The probability distribution $\mathcal{P}(n)$ to find a particle of a certain type within the spatial period n is plotted in Fig. 3.13 (b) after 25 ratchet cycles. The distribution data has been extracted from 100 independent simulation runs. For the small particles, the distribution is already significantly shifted towards the right end of the channel. Accordingly the large particles begin to accumulate at the left end. Panel (b) shows the distribution after 50 ratchet cycles. The accumulation of the distinct particle types at the opposing end of the channel is now more pronounced and only few particles can be found in the middle of the channel ($n = 2$, 3). In other words, the particles have been separated.

Assuming that the channel is connected to fluid reservoirs at both ends and that the left reservoir contains both types of particles the channel can act as a selective pump. The mean displacements for both particle types in Fig. 3.12 reveal three operational modes controlled by the actual value of T_-. First, the induced mean displacement can prevent both particles types to pass through the channel ($\langle \Delta \bar{x} \rangle < 0$ for both particles). Second, the small particles are pumped through the channel while the large particles are blocked ($\langle \Delta \bar{x} \rangle_{\text{small}} > 0$ and $\langle \Delta \bar{x} \rangle_{\text{large}} < 0$). Third, both particle types are pumped through the channel ($\langle \Delta \bar{x} \rangle > 0$ for both particles). In principle, this selective pumping between both reservoirs can be extended to suspensions containing more types of particles.

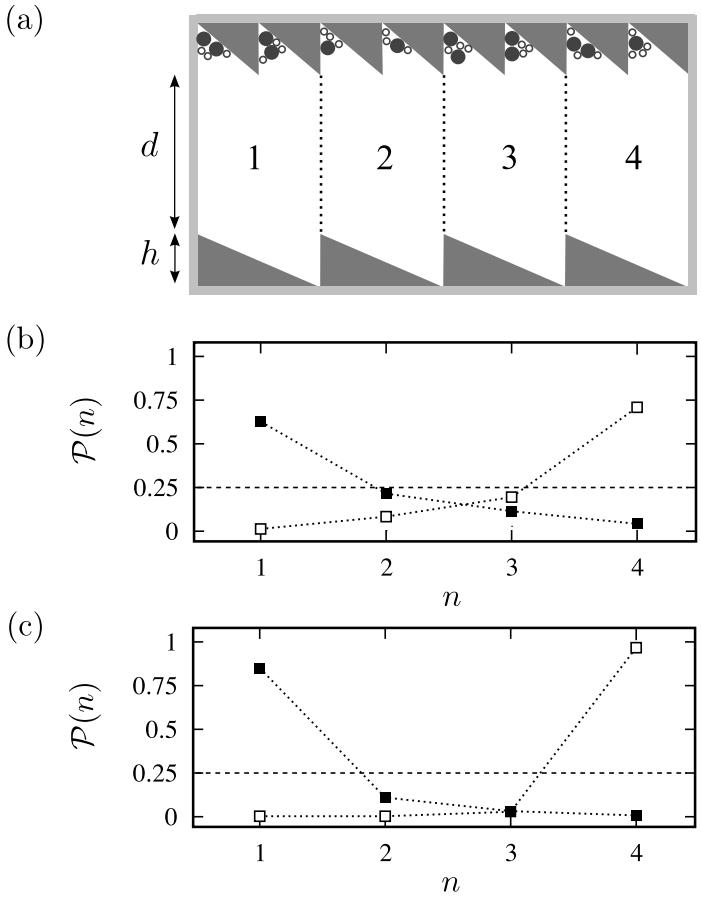

Figure 3.13: (a) Channel setup with four spatial periods confined by two vertical walls. Two particle types with different radii are schematically shown at the end of the time period $\bar{T}_+$ with the external force pointing upwards. (b) Particle distribution $\mathcal{P}(n)$ within the four spatial periods n after 25 ratchet cycles for particles with rescaled radius $\bar{\sigma} = 0.1$ (empty symbols) and with $\sigma = 0.2$ (full symbols). A channel containing 20 particles of each type as simulated. (c) Same as in (b), but after 50 ratchet cycles.

3.5 Conclusions

We have introduced an extension of the standard on-off ratchet by including a second asymmetric sawtooth potential with half the periodicity and inverse asymmetry in the ratchet cycle. As a result of this additional potential, Brownian particles exhibit direction reversal of their mean displacement. Analysis of the Langevin equation reveals that the motion of the particles and, hence,

their mean displacement depends on four dimensionless parameters: the Peclet number, the asymmetry of the potentials, and the rescaled on- and off-times. We have derived analytical expressions for the mean displacement, based on the method of discrete steps and the split-off approximation. We show that these expressions are valid in relevant regions of the parameter space and that they can be used to predict locations in parameter space where direction reversal occurs. We have concentrated on the ratio $1:2$ for the periods of the two sawtooth potentials. However, the formalism presented here can also be applied to other ratios, albeit some expressions will require modifications due to changes in the symmetry of the system.

We have demonstrated that our ratchet model offers new opportunities for the separation of particles in microfluidic devices. In particular, we have shown that the application of direction reversal can overcome the major drawbacks of the classical array designs. Therefore, we have proposed two different designs with significantly reduced system sizes without sacrificing the resolution of the separation process. Exploiting direction reversal in the non-discrete ratchet regime allows a reduction of the device to a *single* channel. Furthermore in both designs non-localized injection is possible, which leads to an increased throughput. We demonstrate that the model of the extended on-off ratchet is able to describe the dynamics of a single particle in the proposed devices. However, one should bear in mind that the model is a simplification. Many-particle effects due to electrostatic and hydrodynamic interactions among the particles are not included. Hydrodynamic interactions between the particles and the obstacles are also neglected. Furthermore, we have assumed a homogeneous external force that is not disturbed by the presence of the obstacles.

Our simulation results demonstrate that particles can be separated effec-

tively in a single channel. It is remarkable that separation can be achieved in a device that only contains four spatial periods. Given the usual dimensions of the obstacles in ratchet-based particle separation, the overall size of the simulated device can be estimated as $50\mu\text{m} \times 50\mu\text{m}$, which is orders of magnitude smaller than conventional devices. The small size of the proposed channel design is appealing for application in integrated microfluidic devices. Furthermore, the channel can be parallelized in y-direction, forming two-dimensional barriers with tunable permeability.

Chapter 4

Pressure-driven vector chromatography

4.1 Motivation

The substantial requirement for ratchet-based particle separation is a spatial asymmetry of the system. It is further crucial that particle trajectories bifurcate effectively when passing through distinct gaps. As discussed in Sec. 2.4.1, both requirements are fulfilled if the external force is homogeneous and the obstacles are permeable to the external force. In this case, the spatial symmetry can simply be broken by the shape of the obstacles. In pressure-driven vector chromatography, however, a pressure difference between two reservoirs generates a fluid flow through the device. The motion of the immersed particles is now determined by the pattern of the flow around the obstacles. For this case, we have shown in Sec. 2.4.3 and 2.4.4 that only particles with a finite size perceive the presence of the obstacles and bifurcate effectively.

In this chapter, we demonstrate that the bifurcation for finite-size parti-

cles itself is not sufficient for the occurrence of the ratchet effect. It is further necessary that the flow field features spatial asymmetry. In this context, it is shown that impermeable obstacles are not able to break the symmetry significantly, even if their shape is asymmteric. In order to overcome this limitation, we introduce a design that allows a fraction of the flow to penetrate the obstacles through gaps. The immersed particles, however, are sterically excluded and have to move around the obstacles. We demonstrate that our approach breaks the symmetry of the fluid flow and facilitates vector chromatography in pressure-driven flows. For the purpose of a quantitative analysis, we introduce a measure for the asymmetry of the flow field. We further introduce a ratchet model to predict the induced mean displacements and validate our predictions by means of Brownian dynamics simulations. In order to calculate the flow fields effectively, we introduce a novel boundary condition for the Lattice-Boltzmann method.

4.2 Calculation of flow fields in microfluidic arrays with bidirectional periodicity

For the calculation of the flow fields in this chapter, we use the Lattice-Boltzmann method (LBM), which has become a versatile tool for the simulation of fluid flows in complex geometries [16, 112]. In the microfluidic devices studied in this chapter, a pressure gradient between two reservoirs generates a flow through a two-dimensional array of identical obstacles. In addition, the array is confined by solid walls. The setup is schematically depicted in Fig. 4.1 (a). The resulting flow field reflects the bidirectional periodicity of the array. Only in the vicinity of the walls and the reservoirs the periodicity of the flow

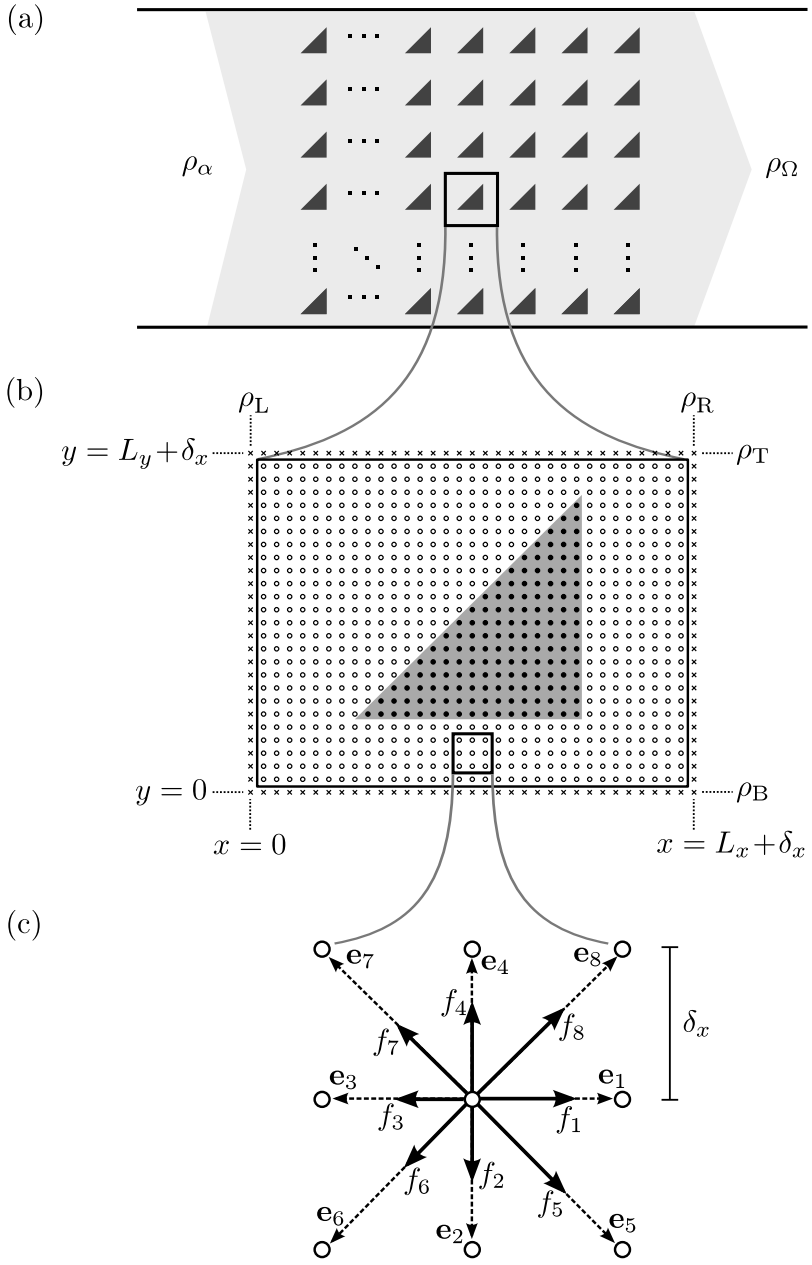

Figure 4.1: (a) Exemplary microfluidic device consisting of an periodic array of triangular obstacles. A pressure gradient ($\rho_\alpha > \rho_\Omega$) drives a fluid flow from left to right. (b) A single unit cell including the lattice nodes: fluid nodes (open circles), solid nodes (full circles), and GPBC boundary nodes (crosses). (c) Lattice vectors $\boldsymbol{e}_i$ and distribution functions f_i for a single lattice node.

is not fully established. Due to the large number of obstacles in such arrays, it is desirable to exploit the periodicity of the system in both directions. This would allow the reduction of the simulated system to a unit cell containing only a single obstacle.

With the boundary conditions known in literature, the full periodicity of the system cannot be exploited if the obstacles are asymmetric with respect to the x-axis. The depicted triangular obstacles clearly create such asymmetric scenario. Here, the flow initially adjusts its direction according to the shape of the obstacles reducing the effective resistance of the array. Hence, a net flow component perpendicular to the pressure gradient emerges. Due to the confining walls, this perpendicular flow gives rise to a perpendicular pressure gradient. This perpendicular pressure gradient increases until the forces resulting from obstacle are balanced and the perpendicular component of the flow vanishes.

In the following section, we introduce a Lattice-Boltzmann approach that correctly reflects the effect of the walls on the flow within a single unit cell. The simulation setup uses an adaptive perpendicular pressure gradient to suppress the perpendicular flow. This pressure gradient is adjusted through a standard proportional-differential controller loop, using the cell's vertical leakage and momentum as controlling quantities.

4.2.1 The Lattice-Boltzmann algorithm

Within two-dimensional LBM, the simulated system is mapped onto a uniform lattice of $N_x \cdot N_y$ lattice nodes with lattice constant δx. The lattice is schematically depicted for a unit cell of the array in Fig. 4.1 (b). At each node, a set of nine lattice vectors $\boldsymbol{e}_i$ is defined, *i.e.*, the eight vectors pointing to the

neighboring nodes and a null vector (see panel (c)).[1] The state of the system is then described by a set of distribution functions f_i at every lattice node. The distribution functions f_i correspond to the amount of molecules with a discrete velocity $\boldsymbol{u}_i = \boldsymbol{e}_i/\delta t$, with δt being the time between two simulation steps. As commonly done in the discussion of LBM, all quantities are in the following given in units of δx, δt and combinations thereof. The lattice vectors and the corresponding distribution functions are shown in panel Fig. 4.1 (c) for one lattice node. The macroscopic hydrodynamic parameters, namely density ρ and velocity $\boldsymbol{u}$, can be calculated from the distribution functions at each lattice node through

$$\rho = \sum_{i=0}^{8} f_i; \qquad \boldsymbol{u} = \sum_{i=0}^{8} \frac{f_i \boldsymbol{e}_i}{\rho}. \tag{4.1}$$

The evolution of the system emerges by repeated application of local rules for the redistribution of the functions f_i at each lattice node. For lattice nodes that are not subjected to boundary conditions, so-called fluid nodes, the propagation of the system is defined by the Lattice-Boltzmann equation

$$f_i\left(\boldsymbol{r} + \boldsymbol{e}_i, t + \delta t\right) - f_i\left(\boldsymbol{r}, t\right) = \Omega(\boldsymbol{f}). \tag{4.2}$$

Fluid nodes are represented by open circles in Fig. 4.1 (b). Two processes contribute to the evolution of the system. First, the populations f_i propagate freely along the lattice links. Second, the populations are redistributed by the collision operator Ω. The latter reflects the effect of microscopic collisions on

[1] This is the most commonly used two-dimensional lattice which is denoted as D2Q9. For a three-dimensional problems, lattices with either 18 vectors (D3Q18) or 27 vectors (D3Q27) are used. In the following, all our discussions will be based on a D2Q9-system of unit vectors, however, extension to other systems is straightforward.

the evolution on the distribution functions. In this sense, the collision operator takes dissipation into account. A proper formulation of $\Omega(\boldsymbol{f})$ has to fulfill the local conservation of mass and momenta. The most commonly used collision operator is the linear Bhatnagar-Gross-Krook (LBGK) relaxation operator[8]

$$\Omega(\boldsymbol{f}) = -\frac{(f_i - f_i^{\mathrm{eq}})(\boldsymbol{r}, t)}{\tau}, \tag{4.3}$$

with a linear decay to the local equilibrium distribution f_i^{eq}. The relaxation time τ determines the rate of change towards the local equilibrium and has to be set to $\tau > 0.5$ for stable decay [102, 74]. It has further been found that confining the relaxation time to $\tau < 1$ minimizes simulation errors. The equilibrium distribution f_i^{eq} is defined as a quadratic expansion of the Maxwell-Boltzmann equilibrium distribution

$$f_i^{\mathrm{eq}}(\rho, \boldsymbol{u}) = w_i \rho \left(1 + \frac{\boldsymbol{e}_i \cdot \boldsymbol{u}}{c_s^2} + \frac{1}{2} \frac{(\boldsymbol{u} \cdot \boldsymbol{e}_i)^2}{c_s^4} - \frac{1}{2} \frac{\boldsymbol{u}^2}{c_s^2} \right). \tag{4.4}$$

The weight factors w_i depend on the chosen set of unit vectors and are derived under the condition of rotational invariance. Furthermore, the speed of sound c_{s} is set to $c_s = 1/\sqrt{3}$ and relates density to pressure through the equation of state $p = c_{\mathrm{s}}^2 \rho$.

Bounce-back mechanism

The propagation of the system described in Eq. (4.2) needs to be adapted for lattice nodes that are a part of a solid obstacle. Such so-called solid nodes are represented by full circles in Fig. 4.1 (b). In most cases, solid nodes are simulated using the bounce-back mechanism [78]. During propagation, the component of the distribution function that would propagate into the solid

node is reflected back towards the initial node. This rule results in no-slip boundary conditions in the middle between both nodes.[2]

Generalized periodic boundary conditions

As shown in Fig. 4.1 (a), the array of obstacles is confined by outer walls and connected to reservoirs of different pressures ρ_α and $\rho_\Omega < \rho_\alpha$. The pressure difference over the system results in a periodic pressure gradient over each unit cell

$$\rho(x, y) - \rho(x + L_x, y) = \Delta\varrho_x \tag{4.5}$$

with $L_x = N_x \cdot \delta x$ being the spatial period of the unit cell in x-direction. The corresponding current through the device, however, is periodic

$$\boldsymbol{j}(x, y) = \boldsymbol{j}(x + L_x, y). \tag{4.6}$$

In an asymmetric geometry, a pressure gradient in y-direction

$$\rho(x, y) - \rho(x, y + L_y) = \Delta\varrho_y \tag{4.7}$$

will arise over time. In the fully developed state, it will suppress any net flow through any horizontal cross section over the unit cell interval such that

$$j_\perp(y) = \int_x^{x+L_x} \boldsymbol{j}_y(x, y)\mathrm{d}x = 0. \tag{4.8}$$

The boundary conditions for such a system have to take the periodicity of the momentum field in x- and y-direction into account. Furthermore, a constant

[2]The simple and flexible implementation of no-slip boundary conditions even for complex geometries can be considered as one reason for the widespread popularity of the Lattice-Boltzmann method.

pressure gradient in x-direction driving the flow has to be maintained, while another pressure gradient in y-direction has to be applied to fulfill $j_\perp = 0$ in the fully established state.

For the boundary conditions in x-direction, we use the generalized periodic boundary conditions (GPBC) that were suggested by Kim *et al.* [67]. This approach combines periodic momentum density with a pressure gradient for one dimension.[3] It therefore allows the reduction of the array to a single row by exploiting its periodicity in x-direction. Fixed average densities are assumed on the right and left boundary outside the unit cell: $\overline{\rho}(x = 0) = \rho_\mathrm{L}$ and $\overline{\rho}(x = L_x + \delta x) = \rho_\mathrm{R}$. Those lattice nodes lying outside the unit cell at $x = 0$ and $x = L_x + \delta x$ are represented by crosses in Fig. 4.1 (b). It should be noticed that the externally applied density difference $\Delta\rho_x = \rho_\mathrm{L} - \rho_\mathrm{R}$ is not identical to the periodic density gradient $\Delta\varrho_x$, since it is taken over a distance $L_x + \delta x$ slightly larger than the unit cell. Fluctuations in the pressure along the vertical boundaries are carried onward

$$\begin{aligned} \rho(0, y) &= \rho_\mathrm{L} + \rho(L_x, y) - \overline{\rho}(L_x), \\ \rho(L_x + \delta x, y) &= \rho_\mathrm{R} + \rho(\delta x, y) - \overline{\rho}(\delta x). \end{aligned} \tag{4.9}$$

The average densities on the inner boundaries of the unit cell, $\overline{\rho}(x = \delta x)$ and $\overline{\rho}(x = L_x)$, are not pre-defined but taken from the simulation. The velocity on

[3] In earlier works, a pressure gradient was often replaced by a body force akin to gravity. Such a force alters the equilibrium distribution, and hence simple periodic boundary conditions could be used. This approach however requires a uniform cross-sectional area of the system to give correct results. Generalised periodic boundary conditions for periodic flow velocities [120] and momentum densities [67] with pressure gradients allow to simulate such geometries without having to resort to a body force.

the vertical boundaries, given these pressures and the periodicity condition, is

$$\begin{aligned} \boldsymbol{u}(0,y) &= \frac{\rho(L_x,y)}{\rho(0,y)}\,\boldsymbol{u}(L_x,y), \\ \boldsymbol{u}(L_x+\delta x,y) &= \frac{\rho(\delta x,y)}{\rho(L_x+\delta_x,y)}\,\boldsymbol{u}(\delta x,y). \end{aligned} \tag{4.10}$$

The distribution functions on the corresponding nodes are given by the sum of the equilibrium distribution of the known density and velocity, and the non-equilibrium distribution of the corresponding periodic node

$$\begin{aligned} f_i(0,y) &= f_i^{\mathrm{eq}}(\rho(0,y),\boldsymbol{u}(0,y)) + f_i(L_x,y) - f_i^{\mathrm{eq}}(L_x,y), \\ f_i(L_x+\delta x,y) &= f_i^{\mathrm{eq}}(\rho(L_x+\delta x,y),\boldsymbol{u}(L_x+\delta x,y)) \\ &\quad + f_i(\delta x,y) - f_i^{\mathrm{eq}}(\delta x,y). \end{aligned} \tag{4.11}$$

Adaptive generalized periodic boundary conditions

For the boundary conditions in y-direction, we also use GPBC. As opposed to the x-direction, the pressure gradient between the top and bottom boundary nodes $\Delta\rho_y = \rho_{\mathrm{B}} - \rho_{\mathrm{T}}$ is not constant, but is adjusted to suppress $j_\perp$. We refer to these boundary conditions in the following as adaptive generalised periodic boundary conditions (AGPBC).

Densities, velocities and distributions on the upper and lower boundary nodes with $y = L_y + \delta_x$ and $y = 0$, respectively, are defined in analogy to Eqns. (4.9-4.11). The density on the corner nodes is given through the periodicity

conditions:

$$\begin{aligned}
\rho(0,0) &= \rho(L_x,L_y) + \Delta\varrho_x + \Delta\varrho_y \\
\rho(L_x+\delta x,0) &= \rho(\delta x,L_y) - \Delta\varrho_x + \Delta\varrho_y \\
\rho(0,L_y+\delta x) &= \rho(L_x,\delta x) + \Delta\varrho_x - \Delta\varrho_y \\
\rho(L_x+\delta x,L_y+\delta x) &= \rho(\delta x,\delta x) - \Delta\varrho_x - \Delta\varrho_y.
\end{aligned} \tag{4.12}$$

Since $\Delta\varrho_x$ is not an *a priori* known quantity, it has to be measured within the simulation, and the result will only be applicable in the fully developed state.

In the following, we introduce a controller algorithm to adapt ρ_B and ρ_T. In general terms, the average density on both boundaries needs to be adapted in order to suppress $j_\perp$. In a fully developed flow, Eq. (4.8) has to hold for any row y. Alternatively, we can require the total perpendicular momentum of the fluid in the unit cell

$$\begin{aligned}
j_y^\mathrm{tot} &= \int_V j_y \mathrm{d}x\mathrm{d}y \\
&= \sum_{k=1}^{N_x}\sum_{l=1}^{N_y}\sum_{i=0}^{8} \boldsymbol{e}_y\cdot\boldsymbol{e}_i f_i(k\delta x, l\delta x)
\end{aligned} \tag{4.13}$$

and the net leakage through the upper and lower walls of the cell

$$\begin{aligned}
\Phi_y &= \oint_{\partial V} j_y \boldsymbol{e}_y \mathrm{d}\boldsymbol{o} \\
&= \sum_{k=1}^{N_x}\Bigg(\sum_{m=2,5,6} f_i(k\delta x, L_y) - f_i(k\delta x, 0) \\
&\qquad + \sum_{i=4,7,8} f_i(k\delta x,\delta x) - f_i(k\delta x, L_y+\delta x)\Bigg)
\end{aligned} \tag{4.14}$$

to vanish separately. The total perpendicular momentum j_y^{tot} is a much better control quantity than the flow through a single line since it is less affected by fluctuations traveling through the liquid while the flow is developing. We control j_y^{tot} through the density difference $\Delta\rho_y$ and Φ_y through the density at the lower boundary ρ_{B}, which each are adjusted using a standard PD controller algorithm [32], such that

$$-\frac{\mathrm{d}}{\mathrm{d}t}\Delta\rho_y = K_{\mathrm{d}}\frac{\mathrm{d}}{\mathrm{d}t}j_y^{\mathrm{tot}} + K_{\mathrm{p}}j_y^{\mathrm{tot}} \tag{4.15}$$

and accordingly for ρ_{B} and Φ_y.

4.2.2 Validation of the method

In order to be able to evaluate the precision of our proposed adaptive boundary conditions, a reference system needs to be defined. We will take this reference from a system that contains one complete row of obstacles in y-direction including, the confining walls. The effects of the walls on the flow are hence fully captured, although finite size effects limiting the periodicity may arise.

Consider the array of obstacles shown in Fig. 4.1 (a). Using GPBC in x-direction, this array can be reduced to a $1 \cdot M_y$ array. Each unit cell contains a solid triangular obstacle. We choose $M_y = 7$, which is enough to achieve sufficient periodicity at the inner cells and can still be easily simulated with modern computers. A unit cell grid of $N_x = N_y = 200$ lattice nodes is used. The LBM relaxation time is set to $\tau = 0.8$, corresponding to a kinematic viscosity of $\nu = \delta x^2/10\delta t$. Using the resulting average flow velocity and the horizontal length of the obstacle as characteristic length and velocity, this setup corresponds to a Reynolds number of $\mathrm{Re} \approx 10^{-1}$. This is an approximate

upper boundary for our method since above this threshold, time dependencies – *albeit* very small ones – make it impossible to compare the accuracy in the stationary case at the achieved level. As we will see later in this chapter, the discussed microfluidic devices work in regimes with Reynolds numbers significantly below this threshold.

The value of $\Delta\rho_{\mathrm{y}}$ was adjusted using $K_{\mathrm{d}} = 0.8 \cdot 10^{-5}$ and $K_{\mathrm{p}} = 0.8 \cdot 10^{-6}$, while $K_{\mathrm{d}} = 0.5 \cdot 10^{-5}$ and $K_{\mathrm{p}} = 0.5 \cdot 10^{-4}$ were used for controlling ρ_{B}. Initially, the fluid in the system is inert. The simulation is run for $4 \cdot 10^5$ steps. The controller loop was started after an initialisation period of 10^4 steps, to avoid initial effects affecting the control variables. In the following, we use the central unit cell of this array as our reference system. Density averages at $x = 0$ and $x = L_x + \delta x$ are set to 1.00001 and 1.0 respectively.

Note that the average density difference $\Delta\rho_x$ calculated over the entire row of seven unit cells (*i.e.*, averaging from $y = \delta x$ to $y = M_y \cdot L_y$) is kept fixed. The flow velocities however vary due to the friction at the confining walls. To be precise, the flow in the inner cell, the reference system, is faster than the flow in cells closer to the walls. Only considering the middle cell, the flow seems to be driven by an increased effective pressure gradient ($\Delta\rho_x^{\mathrm{eff}} > \Delta\rho_x$). This error is a finite size effect intrinsic to the reference system and is not related to the single cells' setup. It vanishes with increasing number of obstacles within the row. We have to keep this deviation in mind for the subsequent comparison of both systems.

In the following, we use the reference system to test the accuracy of a single unit cell using AGPBC. For comparison, we also show the results for a cell that also uses GPBC in x- but simple periodic boundary conditions (SPBC) in y-direction. The resulting flow isolines $|\boldsymbol{v}|$ after $3 \cdot 10^5$ simulation steps are

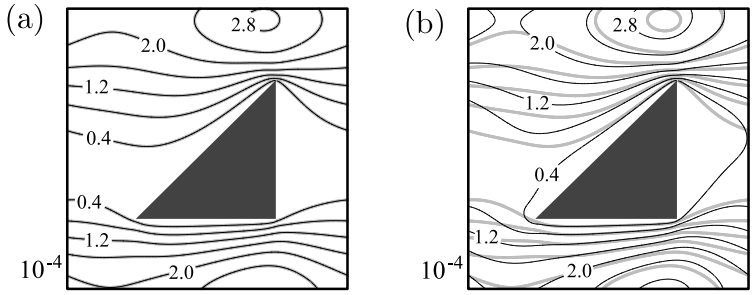

Figure 4.2: Flow isolines $|\boldsymbol{u}|$ of the reference system (thick gray lines) and the single cell (thin black lines) (a) with AGPBC (b) with SPBC. In both panels, velocity isolines are spaced by $4 \cdot 10^{-5} \delta x / \delta t$. The factors at the bottom left side indicate the order of magnitude.

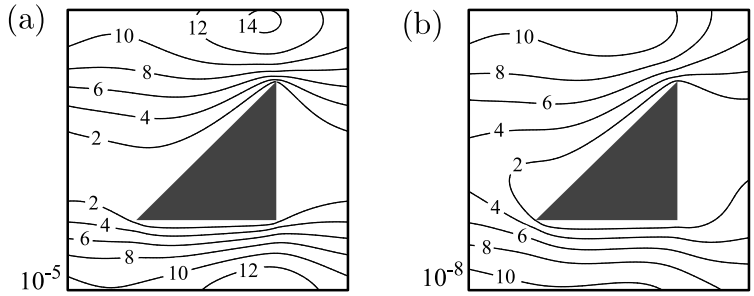

Figure 4.3: Relative deviations ϵ between the reference system and the single cell using AGPBC. (a) $\Delta\rho_x$ is equal for the reference system and the single cell. (b) The effective pressure gradient $\Delta\rho_x^{\text{eff}}$ of the reference system is applied to the single cell. The factors at the bottom left side indicate the order of magnitude.

shown in Fig. 4.2. Here, panel (a) shows the results for AGPBC, while panel (b) gives the isolines for SPBC. In both panels, the isolines of the control system are depicted as thicker gray lines. Results for AGPBC coincide with the control system to a degree where the isolines become indistinguishable. In contrast, deviations are clearly visible for SPBC. Here, the deviations in the velocity are of the same order of magnitude as the average flow velocity. The significant deviations are expected, since SPBC completely ignore the effects of asymmetric obstacles.

To quantify the deviations, we introduce the measure ϵ for the relative

error

$$\epsilon = \left(\frac{(|\boldsymbol{u}| - |\boldsymbol{u}_{\mathrm{ref}}|)^2}{\overline{\boldsymbol{u}}^2_{\mathrm{ref}}} \right)^{1/2}, \tag{4.16}$$

with the mean square flow velocity $\overline{\boldsymbol{u}}^2_{\mathrm{ref}}$ averaged over of the complete reference cell. The corresponding error data is shown in Fig. 4.3. Panel (a) shows the deviations between the reference system and the system with AGPBC. The errors are of the order 10^{-4}. Evidently, the error in the velocity appears to be proportional to the velocity itself, indicating that it may stem from the small difference in the pressure gradient $\Delta\rho_x$ discussed above. To test this hypothesis, we simulate the AGPBC system and apply the effective pressure gradient $\Delta\rho_x^{\mathrm{eff}}$ of the reference system. As shown in panel (b), the resulting error is reduced by several orders of magnitude, showing that the originally observed error was caused by the mismatch in $\Delta\rho_{\mathrm{x}}$. Furthermore, such an error is of a particular type, since only the flow velocity but not the flow pattern is altered. In fact, a simple rescaling of the flow velocities in order to match the density gradients would suffice to reduce the error by the same order of magnitude (data not shown).

The time evolution of the adaptive density gradient is shown in Fig. 4.4 (a). After the initialisation period, a very short period with strong fluctuations follows. Compared with the density gradient over the reference system, the adaptive density gradient thereafter converges faster and with smaller fluctuations against its long time limit. Notably, the density difference over the outermost cells differs significantly. This is caused by the presence of the solid outer walls, which slow down the flow considerably. However, already for our seven-cell system, such deviations occur only for the cells in direct contact with the solid walls. Density differences over all unit cells are shown in Figure 4.4

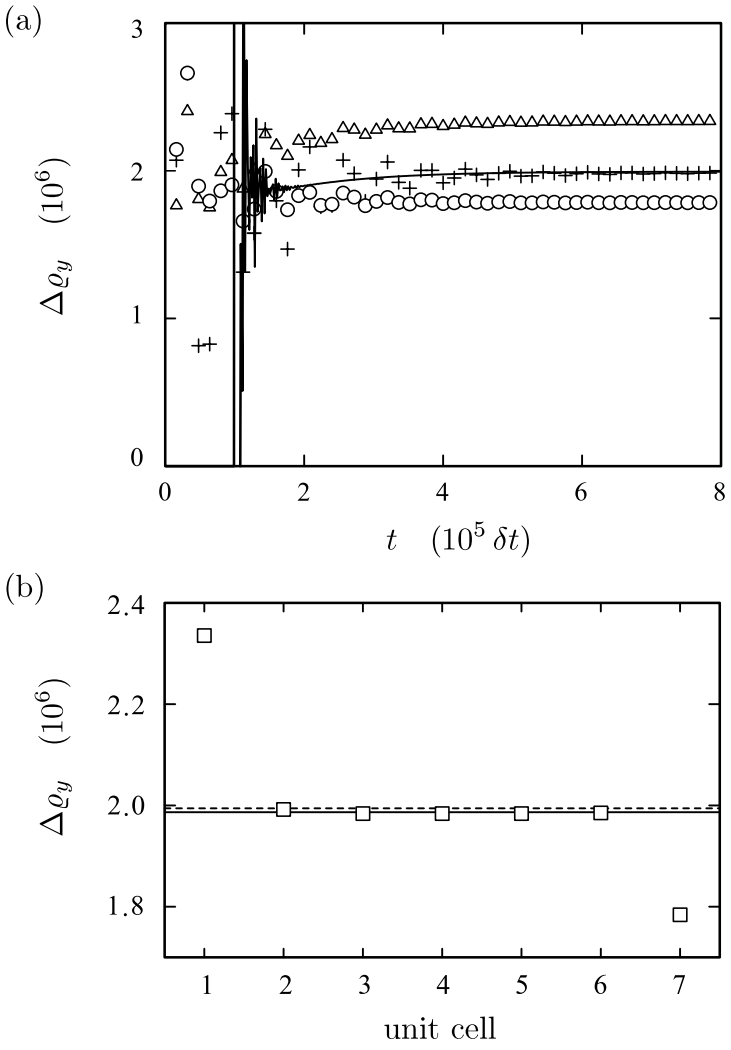

Figure 4.4: (a) Evolution of the density difference $\Delta\rho_y$ for the adaptive system (solid line) compared to the density difference over the topmost ($\circ$), central ($+$) and bottommost ($\triangle$) unit cells of the row. (b) Steady state values of the density difference over different unit cells of the row ($\square$), with the applied adaptive difference $\Delta\rho_y$ (dashed, between nodes 0 and 201) and the resulting periodic difference $\Delta\varrho_y$ (solid, between nodes 1 and 201) as horizontal lines.

(b) for the long time limit when numerical accuracy was reached ($t \approx 4{\cdot}10^5\delta t$). The differences over all inner cells are virtually identical and agree very well with the resulting $\Delta\varrho_{\mathrm{y}}$ over the unit cell with AGPBC.

4.3 Ratchet-based particle separation in asymmetric flow fields

In this section, we begin with a discussion of the flow around completely impermeable obstacles, similar to those used in conventional devices. We show that the corresponding flow fields are lacking the required asymmetry. Subsequently, we introduce a novel type of obstacles, which are partially permeable for the fluid flow and therefore generate asymmetric flows. We investigate how and to what extent the symmetry of the flow is broken. We furthermore estimate the key characteristics of the separation process by applying standard Brownian ratchet theory and validate the theoretical predictions by means of Brownian dynamics simulations.

4.3.1 Breaking the symmetry of flow fields

The setups of the simulated devices are similar to the one depicted in Fig. 4.1 (a). An periodic array of obstacles is confined by two walls in y-direction and connected to reservoirs with different pressures at each end of the device. As a consequence, a fluid flow is generated through the array in x-direction. We determine the flow fields by means of the Lattice-Boltzmann Method using the adaptive generalized periodic boundary condition that has been introduced in the previous section. The unit cell of the array has spatial extensions L_x and L_y and contains a single obstacle. The constant pressure difference $\Delta\rho_x$ that drives the fluid flow is taken into account via generalized boundary conditions. Furthermore, a self-adjusting pressure gradient $\Delta\rho_y$ in y-direction develops during the calculation, in order to match a zero net flow condition in that direction. As discussed in the previous section, this additional pressure

gradient mimics the effect of the confining walls of the device.

In Fig. 4.5 (a), the flow field for an impermeable, wedge-shaped obstacle is depicted using stream lines. One side of the wedge is parallel to the x-axis while the other is inclined by $\pi/3$. The gap between two adjacent obstacles in x and y-direction is given as δ_x and δ_y, respectively.[4] The shape has an asymmetry with respect to the y-axis, however, the flow around this obstacle lacks the required asymmetry.

In oder to understand why the flow around such an impermeable obstacle is not suitable for pressure driven vector chromatography, the underlying ratchet mechanism needs to be understood. We therefore consider a particle that passes the gap at $(x=0, y=0)$. Without diffusion, this particle would follow the stream line y_0 as indicated in Fig. 4.5 (a) throughout the device and no inclination would occur. For diffusing particles, however, there is a probability p_{+1} to diffuse into the stream S_+ before reaching the next row of obstacles at $x = \delta_x$. In this case, the particle passes through the gap at (L_x, L_y). Accordingly, p_{-1} denotes the probability for the particle to diffuse into the stream S_- and hence pass the gap at $(L_x, -L_y)$. Each time the particle passes a row of obstacles, it experiences a mean displacement of

$$\langle \Delta y \rangle = (p_{+1} - p_{-1}) L_y \tag{4.17}$$

in y-direction. For the ratchet effect, *i.e.*, for a non-zero mean displacement, the probabilities need to be biased. The streams S_+ and S_- are demarcated from the stream S_0 by the lines y_+ and y_-, respectively. For the depicted flow pattern around the obstacle, however, the distances $|y_+ - y_0|$ and $|y_- - y_0|$

[4] A resolution of 400 lattice nodes per δ_x has been used to calculate the flow. Furthermore, it has been checked that the results are indepent on the resolution.

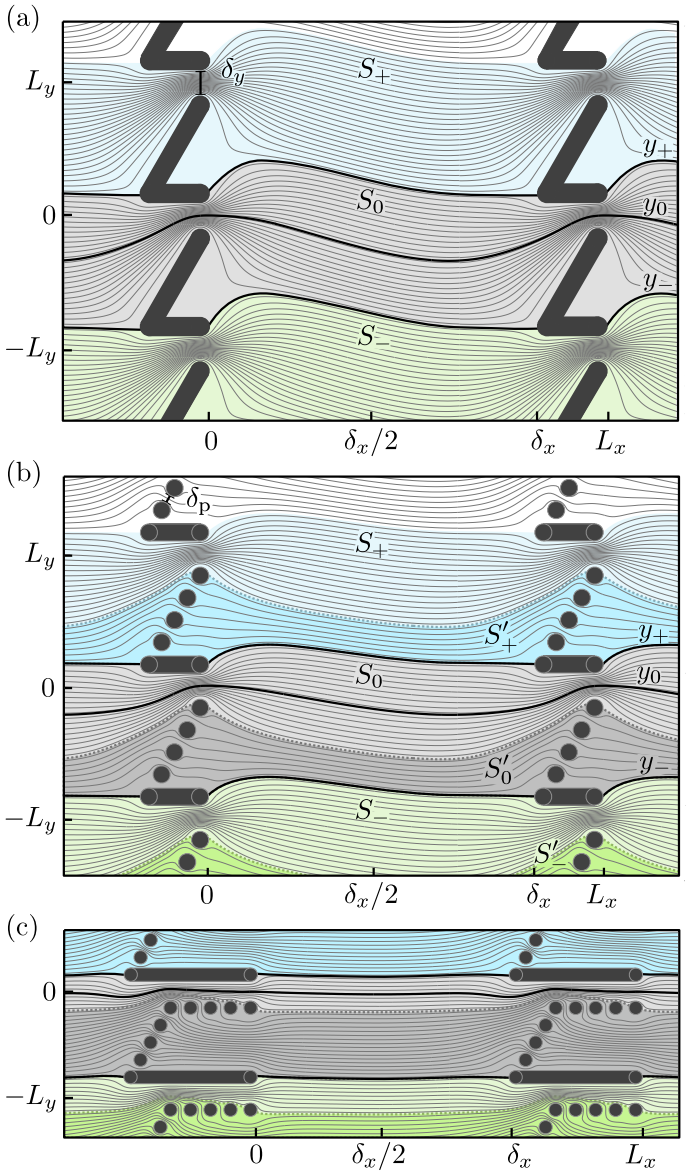

Figure 4.5: (a) Stream lines of the flow field for a solid, wedge-shaped obstacle with $\delta_y = 3\delta_\mathrm{p}$. The dark grey objects represent impermeable structures. The green, grey, and blue streams indicate the fractions S_-, S_0, and S_+ of the flow that pass through the gaps at $y = -L_y$, 0 and L_y, respectively. The black lines y_+ and y_- demarcate the streams S_+ and S_- from S_0, respectively. The black line y_0 indicates the stream line that passes the gaps at $y = 0$. (b) Same as in (a) but for the proposed obstacle. The streams S'_0, S'_+ and S'_- indicate the fractions of the flow that penetrates the obstacles. (c) Same as in (b) but for the extended version of the proposed obstacle with $N = 4$.

are similar for most of the interval between two obstacles. As a consequence, the probabilities are virtually unbiased and the mean trajectory will not be inclined.

In Fig. 4.5 (b), the flow field for our proposed design is shown. The diagonal side of the wedge is replaced by a row of four spherical pillars with radius σ_p, such that the values for δ_y and L_y are unchanged. The distance between two adjacent pillars is δ_p. In this chapter, the parameters are chosen such that $\delta_\mathrm{p} = \sigma_\mathrm{p}$. The change of the design allows the stream S_0' to penetrate the obstacle. For particles with radius σ larger than $\delta_\mathrm{p}/2$, this additional stream breaks the symmetry of the flow pattern, since now $|y_+ - y_0| < |y_- - y_0|$ and hence $p_{+1} > p_{-1}$. As a consequence, the particle experiences a non-zero mean displacement each time it passes a row of obstacles, and the mean trajectory is hence inclined. For a quantitative discussion of the asymmetry, we introduce the dimensionless parameter

$$a = |y_+ - y_0|/L_y \tag{4.18}$$

at $x = \delta_x/2$, *i.e.*, in the middle between two rows of obstacles.[5] Accordingly, the asymmetry of the flow is $a = 0.38$ for our proposed design and $a = 0.5$ for the solid obstacle.[6] Note that a value of 0.5 indicates a symmetric system,

[5]The value of the asymmetry parameter a depends on the actual x-position. In Fig. 4.5 one can see that a becomes smaller if it is measured closer to $x = \delta_x$. We chose to determine a at $x = \delta_x/2$, because the resulting values holds for most x-positions. Furthermore, the deviations close to the obstacle decrease for larger distances δ_x. In this sense, our definition of the asymmetry parameter can be considered as a long distance limit.

[6]The symmetry of the flow field around the impermeable obstacles sheds some light one the discrepancy between experimental results and theoretical predictions that occurred for ratchet-based particle separation [19, 54]. In the models, the geometrical asymmetry of the obstacle, as defined in Fig. 2.7, were used. We have shown now, that the asymmetry of the flow field is relevant for the separation process. The values of the geometrical asymmetry of the obstacles are smaller than the those of the resulting flow field. Using the geometrical asymmetry in the ratchet model therefore leads to an overestimation of the

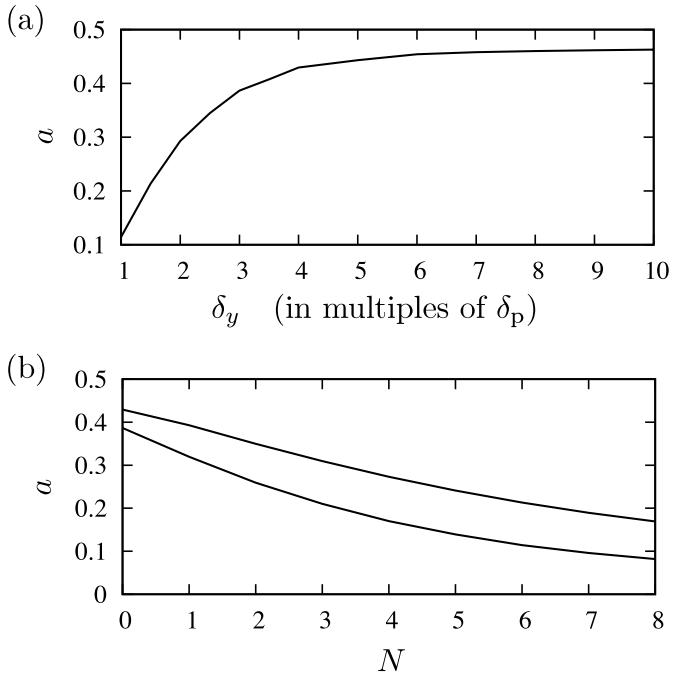

Figure 4.6: (a) Asymmetry parameter a as a function of the gap width δ_y. The gap width is given in multiples of the distance between two adjacent pillars δ_p. (b) Asymmetry parameter a as a function of the number of pillars N in the additional horizontal row. The gap width is $4\delta_p$ (upper line) and $3\delta_p$ (lower line).

while smaller values of a indicate more asymmetric flows.

In Fig. 4.6 (a), the asymmetry parameter a for the proposed obstacle is shown as a function of the gap width δ_y. The asymmetry parameter decreases for smaller gap widths δ_y, *i.e.*, the asymmetry of the flow pattern increases. For smaller gap widths, a larger fraction of the flow penetrates the obstacle, which leads to an increased distance between the y_0 and the y_- line and hence a smaller value for the asymmetry parameter a.

For a larger bias of the probabilities, the flow needs to be more asymmetric. We therefore modify the design in order to allow a wider range of values for a. As depicted in Fig. 4.5 (c), the proposed design is extended by an additional

mean displacement.

horizontal row of N spherical pillars, which connects to the upper end of the diagonal row. The horizontal side of the wedge is elongated such that its extension in x-direction matches the added horizontal row of pillars. The corresponding flow is depicted in Fig. 4.5 (c). The additional horizontal row allows a larger fraction of the flow to penetrate the obstacle without changing L_y and hence increases the asymmetry of the flow pattern. In Fig. 4.6 (b), the asymmetry parameter a is shown as a function of the number of pillars N in the horizontal row. For $N > 6$ and $\delta_y = 3\delta_\mathrm{p}$, the asymmetry parameter decreases to remarkably small values below 0.1.

4.3.2 Ratchet model

The probabilities p_n for a particle to diffuse into the stream S_n and hence the mean displacement $\langle \Delta y \rangle$ can be approximated by means of Brownian ratchet theory [3, 36]. In such a model, the ratchet behavior of a particle is completely determined by the asymmetry parameter a and the rescaled off-time

$$\tau_\mathrm{off} = \delta_x D/(v_x L_y^2) \tag{4.19}$$

with v_x being the average velocity of the flow in x-direction and D the diffusion constant of the particle. For spherical particles, the diffusion constant is related to the friction coefficient γ and the radius σ through the Stokes-Einstein relation $D = k_\mathrm{B}T/\gamma = k_\mathrm{B}T/(6\pi\eta\sigma)$, with η being the viscosity of the fluid. Note that δ_x/v_x is the average time that the particle needs to travel from a gap to the next row of obstacles. The rescaled diffusion constant hence compares the travel time δ_x/v_x with the typical time L_y^2/D for a particle to cover the distance L_y by diffusion.

As previously discussed, the y-position of the particle at the moment it reaches the next row of obstacles determines through which gap it passes. The probability density function $\mathcal{P}(\bar{y})$ to find a particle displaced by the rescaled distance $\bar{y} = (y - y_0)/L_y$ from the flow line y_0 at the position δ_x is assumed to be given by a normal distribution

$$\mathcal{P}(\bar{y}) = \frac{1}{\sqrt{4\pi\tau_{\text{off}}}} \exp\left(-\frac{\bar{y}^2}{4\tau_{\text{off}}}\right). \tag{4.20}$$

Accordingly, the probabilities p_n for a particle to be in the stream S_n at $x = \delta_x$ and hence to pass through the gap at (L_x, nL_y) are given by integrating $P(\bar{y})$, so that

$$p_n = \int_{n-1+a}^{n+a} \mathcal{P}(\bar{y}) \mathrm{d}\bar{y}. \tag{4.21}$$

The mean displacement is hence given by

$$\langle \Delta y \rangle = L_y \sum_{n=-\infty}^{\infty} n\, p_n, \tag{4.22}$$

which is a more general expression of Eq. (4.17). For very small values of the rescaled diffusion constant, the probabilities to reach adjacent gaps vanish and zero mean displacement occurs. For increasing values of τ_{off}, the mean displacement increases monotonously and reaches its maximum value

$$\langle \Delta y \rangle_{\max} = (1/2 - a)\, L_y \tag{4.23}$$

which is solely determined by the asymmetry parameter. Note that this model assumes parallel stream lines in the range $0 < x < \delta_x$. Therefore effects of the shear flow in the vicinity of the obstacles are not taken into account.

Further, effects due to the finite size of the particle as discussed in Sec. 2.4.4 are neglected. Diffusion in x-direction is also neglected, since only the average travel time δ_x/v_x is considered.

4.3.3 Brownian dynamics simulations

In order to validate the theoretical predictions and the feasibility of the separation process, Brownian dynamics simulations of spherical particles in the discussed flow fields were carried out. The simulation of a finite-size particle in shear flow and in the presence of non-trivial boundary conditions is a complex problem, because the involved effects occur on a wide range of time-scales. Since we are interested in particle trajectories that pass a large number of obstacles, it is impossible to fully resolve hydrodynamic effects that happen on much shorter time scales. We therefore have to assume that the presence of a suspended particle does not alter the flow field. In other words, the flow field is solely determined by the obstacles. For the interaction with the obstacles, however, the particles have a finite size.

Under these assumptions, the two-dimensional trajectories $\boldsymbol{r}(t) = (x(t), y(t))$ of suspended particles are governed by the overdamped Langevin equation

$$\dot{\boldsymbol{r}} = \gamma^{-1} \left[\boldsymbol{f}_{\mathrm{obs}}(\boldsymbol{r}) + \boldsymbol{\xi}(t) \right] + \boldsymbol{u}(\boldsymbol{r}). \tag{4.24}$$

The components ξ_i of the random force $\boldsymbol{\xi}$ are unbiased, so that $\langle \xi_i(t) \rangle = 0$, and obey the fluctuation-dissipation theorem

$$\langle \xi_i(t) \xi_j(t') \rangle = 2\gamma k_{\mathrm{B}} T \, \delta_{ij} \delta(t - t'). \tag{4.25}$$

The force $\boldsymbol{f}_{\text{obs}}$ is determined by the interaction potential between the particles and the pillars, which is modeled by a short-ranged, repulsive potential $V_{\text{obs}}(d) \sim d^{-12}$ with d being the closest distance between the surfaces of the particle and the obstacle. The proportionality factor is chosen such that the minimal distance during the simulations is approximately $0.01\,\delta_p$. The displacement of the particle due to the fluid flow is equal to the velocity $\mathbf{u}(\mathbf{r})$ of the fluid at the center of the particle. For the numerical integration of the Langevin equation we use a standard Euler approach with an adaptive time step algorithm.

We simulated particle trajectories in a system with $N = 8$ and $\delta_y = 4\,\delta_{\text{p}}$. The corresponding flow field has an asymmetry of $a = 0.17$ according to the data in Fig. 4.6 (b). With the radius of the pillars set to $\sigma_{\text{p}} = 0.5\,\mu\text{m}$, the system has the spatial dimensions $\delta_y = 2\,\mu\text{m}$, $\delta_x = 20\,\mu\text{m}$, $L_x = 32\,\mu\text{m}$ and $L_y = 8.2\,\mu\text{m}$. Flow velocities in the range from $v_x = 0.36\,\mu\text{ms}^{-1}$ to $36\,\mu\text{ms}^{-1}$ have been simulated. The corresponding Reynolds numbers $\text{Re} = v_x L_y \rho/\eta$ are in the range between 10^{-6} and 10^{-4} and hence completely in the Stokes regime. In this hydrodynamic regime, the flow pattern is independent of the pressure gradient Δp_x. Hence, it is sufficient to scale the velocity field $\mathbf{u}(\mathbf{r})$ in order to achieve the desired average velocity v_x. The resulting rescaled mean displacement $\langle \Delta y \rangle / L_y$ is depicted in Fig. 4.7 (a) as a function of the rescaled off-time τ_{off} for four particle radii σ. The data reveals two operational regimes, depending on the particle size. In the first regime, with particle sizes larger than the inter-pillar distance $2\sigma > \delta_{\text{p}}$, the results agree with the prediction of ratchet theory in Eq. (4.22). In particular, the mean displacement converges closely to the maximum value $\langle \Delta y \rangle_{\max}/L_y = 0.33$ for large values of τ_{off}, as predicted in Eq. (4.23). This behavior indicates that the symmetry of the

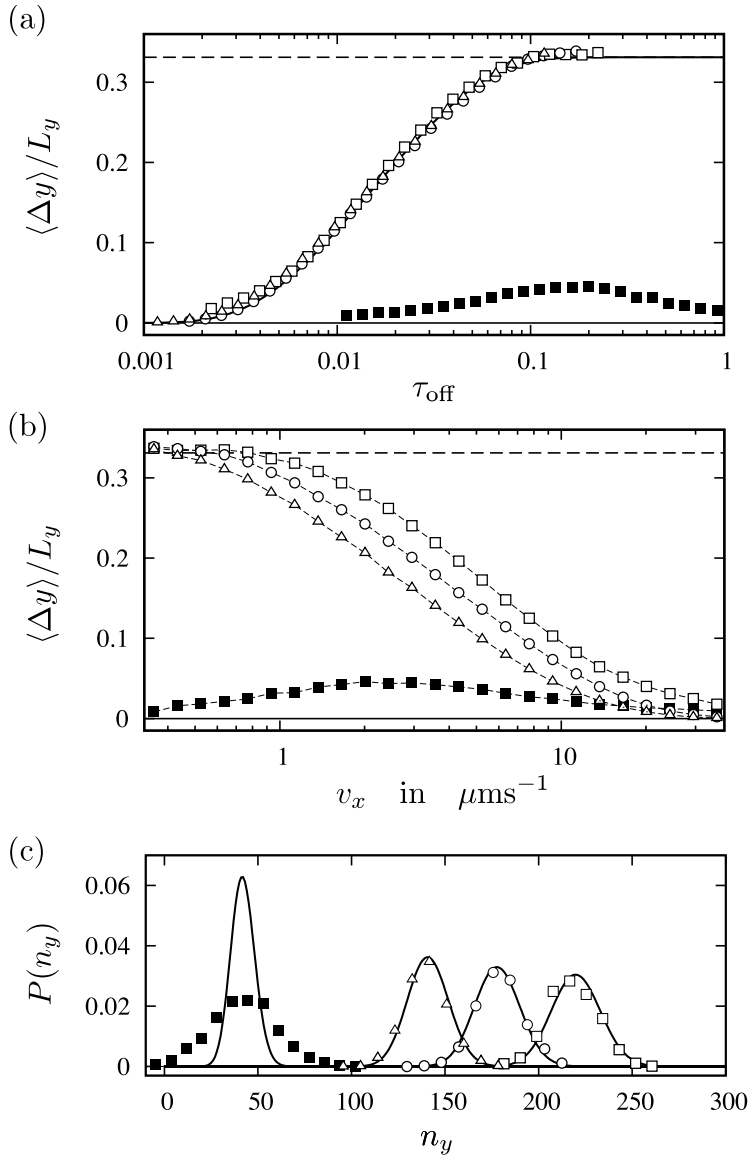

Figure 4.7: Brownian dynamics simulation data for a system with $N = 8$, $\delta_y = 4\,\delta_{\mathrm{p}}$ and $\delta_{\mathrm{p}} = 0.5\,\mu$m and for several particle radii: $\sigma = 0.1\,\mu$m (■), $0.5\,\mu$m (□), $0.7\,\mu$m (○) and $0.9\,\mu$m (△). (a) The rescaled mean displacement $\langle \Delta y \rangle / L_y$ as a function of the rescaled diffusion constant $\mathcal{D}$. The solid line refers to the Brownian ratchet model. The dashed line indicates the maximum value $\langle \Delta y \rangle_{\max}$. (b) Same data as in (a) but as a function of the flow velocity v_x. (c) Probability $P(n_y)$ for the particle to be displaced by n_y gaps in y-direction after having passed 1000 rows.The symbols refer to the simulation results, while the solid line refers to the corresponding binomial distributions.

flow field is indeed broken as predicted and that the ratchet effect occurs. In Fig. 4.7 (b), the same data is depicted as a function of the flow velocity v_x. For a certain value of v_x, the mean displacement decreases with larger particle sizes. This particle size dependence of the mean displacement facilitates vector chromatography, since the trajectories of particles with different radii point towards different directions.

In the second regime, with particle sizes smaller than the inter-pillar distance $2\sigma < \delta_\mathrm{p}$, the particle trajectories are not significantly inclined. Particles of that size can pass between the pillars. As a consequence, they perceive each pillar as an individual impermeable obstacle. Since individual pillars are not able to break the symmetry of the flow pattern, the mean trajectories are not expected to be inclined. The small values observed for $\langle \Delta y \rangle / L_y$ in that region may rise from finite-size effects, as discussed in Sec. 2.4.4 and Ref. [53].

Assuming that all probabilities but p_{+1} and p_0 are negligible, the rescaled mean displacement $\langle \Delta y \rangle / L_y$ is equal to p_{+1}. The probability to find the particle displaced by n_y gaps in y-direction after having passed n_x rows in x-direction is hence given by a binomial distribution. In Fig. 4.7 (c), the numerical results for $v_x = 3.6\ \mu\mathrm{ms}^{-1}$ are compared with the corresponding binomial distributions for $n_x = 1000$. For $2\sigma > \delta_\mathrm{p}$ the numerical data is well described by binomial distributions. For $2\sigma < \delta_p$, however, the numerical results clearly deviate from the binomial distribution. This further indicates that the behavior of particles in this regime is not described by the discussed ratchet effect. The results in this figure demonstrate that vector chromatography can be effectively realized in such a device, since the distributions for the three particle sizes that operate in the first regime are clearly distinguishable and completely separated from the distribution for the particle size that operate in the second

Figure 4.8: Position of fixed particles with radius $\sigma = 1.8\,\delta_\mathrm{p}$, that have been used to estimate the effect of finite-size particles on the asymmetry of the flow. The horizontal dashed lines indicate the extension of the unit cell in y-direction.

regime.

The applicability of the proposed method is limited by two conditions. First, the flow has to be in the regime of low Reynolds numbers, which is virtually always the case for microfluidic flows. Second, diffusion needs to be sufficiently strong to induce non-zero mean displacements. For the investigated system with $N = 8$ and $\delta_y = 4\delta_\mathrm{p}$, this requirement translates to the condition $\tau_\mathrm{off} > 0.005$ for the rescaled diffusion constant (see. Fig. 3 (a)). For the studied flow velocity $v_x = 3.6\,\mu\mathrm{ms}^{-1}$, the latter condition gives an upper bound of about $\delta_\mathrm{p} = 1.3\,\mu\mathrm{m}$ for the system size. Note that larger values of δ_x raise this upper bound. The advantage of the proposed method, however, is that no lower bound for the system size exists. In fact, the separation becomes more efficient for smaller system sizes, as diffusion is the driving process of the separation mechanism.

We conclude with brief remarks on two approximations used in this chapter. First, the effect of suspended particles on the asymmetry of the flow has been neglected. In order to get an upper bound for this effect, we placed a fixed particle at several positions indicated in Fig. 4.8 and recalculated the flow for a system with $N = 8$ and $\delta_y = 4\delta_\mathrm{p}$. For this purpose, we used particles with

Table 4.1: Asymmetry parameters a of the perturbed by a fixed, finite-size particle at the positions indicated in Fig. 4.8. The data is based on simulations with $N = 8$ and $\delta_y = 4\delta_\mathrm{p}$. The last row gives the value for the unperturbed flow without any particle.

position index	asymmetry a
1	0.169
2	0.170
3	0.173
4	0.166
unperturbed	0.169

$\sigma = 1.8\,\delta_\mathrm{p}$ which is the largest radius that has been investigated in this chapter. We limit the analysis on particles placed in front of the obstacle. Here, their motion is hindered by the pillars and the particles act approximately as fixed objects. Since fixed particles have a larger impact on the flow pattern than suspended ones, this approach is sufficient to estimate the maximal impact. The obtained asymmetries are shown in Table 4.1 and reveal a maximum deviation of about 3 % to the unperturbed flow. This estimate indicates that finite-size particles slightly affect the asymmetry of the flow, however, the magnitude of their impact is clearly not sufficient to impede the discussed symmetry breaking.

Second, the effect of other interactions between particles and obstacles has not been discussed in this chapter, although other types , *e.g.*, screened electrostatic interactions, might be relevant in the considered systems. For our separation process, additional repulsive interactions allow larger inter-pillar distances for a given particle size. In fact, the repulsion simply increases the effective radius of the particles. The range of separable particles is hence shifted towards smaller sizes. For long-ranged potentials, the effective size however depends on the flow velocity, as repulsive forces from the obstacles can

be compensated by faster flow rates. In this case, particles are pushed through the gaps surpassing a potential maximum. We hence chose the quasi-hardcore potential (d^{-12}), whose effect is virtually independent of the flow velocity. We want to highlight that the asymmetry of the flow is determined by the geometry of the obstacle and hence independent of the actual type of interaction. Any interaction between particles and obstacles that excludes particles from the inside of the obstacle is sufficient for the separation mechanism.

4.4 Conclusions

In summary, a mechanism has been introduced that facilitates pressure driven vector chromatography based on the ratchet effect. The key feature of the proposed design is the penetration of a certain fraction of the fluid flow through the obstacles, which results in a non-zero normal force at the surface of the obstacles for sterically excluded particles. This approach breaks the symmetry of the flow pattern. Highly asymmetric flow patterns can be achieved with the proposed extension of the obstacle design.

For an experimental realization the actual design may differ from the proposed one, as long as the conceptual key features are maintained. We are convinced that the discussed example can be realized with available lithographic methods. However, the uniformity of the array and the required aspect ratios of the pillars pose a challenge. It needs to be stressed, that any technological progress that allows the fabrication of smaller obstacle sizes would immediately lead to improved separation characteristics.

The proposed ratchet based separation approach has to be compared with existing pressure driven methods such as continuous separation through deter-

ministic lateral displacement [53, 56, 57]. The method has been successfully demonstrated for particle sizes in the order of 1 μm. However, the underlying deterministic separation mechanism is perturbed by diffusion. Therefore, high flow velocities were necessary in order to suppress negative effects of diffusion. Since it is not possible in microfluidic devices to increase the flow velocity to arbitrary values, there exists a lower bound for the particle sizes that can be separated by that method. In contrast, the proposed ratchet-based mechanism has in principle no lower bound for the particle size and therefore extends the range of separable particles to smaller sizes.

Chapter 5

Enhanced ratchet effect induced by hydrodynamic interactions

5.1 Motivation

A wide range of collective effects in ratchet systems has been investigated in literature. In those studies it has been reported that coupling among particles significantly influence the magnitude of the induced mean velocity as well as the direction [4, 6, 17, 75, 101, 107]. Hydrodynamic coupling of colloidal particles in ratchet systems has however attracted only minor interest. This seems to be surprising, as hydrodynamic interactions are, in some sense, the intrinsic coupling in colloidal systems. Effects of hydrodynamic interactions on ratchet systems have so far been investigated only in two numerical studies. In the first study, hydrodynamic coupling was included in the ASEP model for the dynamics of Brownian motors [51]. In the second study, hydrodynamic interactions were included in Brownian dynamics simulations of a harmonically coupled dimer in a ratchet potential [43]. Both studies reported significantly

increased mean velocities of the Brownian motors and dimers, respectively, due to hydrodynamic coupling. However, a microscopic understanding of the mechanism enhancing the ratchet effect was not given in either of both studies.

One collective effect that appears particularly interesting in view of ratchet systems, has been studied by Lutz *et al.* [87]. Here, colloidal particles moved under the influence of a tilted sawtooth potential in a toroidal trap setup. A caterpillar-like motion pattern was observed for a pair of particles. The pattern is caused by a repetitive sequence of hydrodynamic interactions as shown in Fig. 5.1. Initially, particle A is trapped in a minimum of the potential, while particle B drifts towards the same minimum. Due to hydrodynamic interactions particle A is pushed over the maximum of the potential and drifts to the next minimum. While doing so, it will drag particle B over the maximum. As soon as particle A reaches the next minimum, one caterpillar cycle is completed. As a result, the particles move with a significantly increased mean velocity compared to a single particle in the same potential. It has yet not been investigated whether hydrodynamic coupling is able to cause similar motional pattern in ratchet systems.

In this chapter, we study numerically how pure hydrodynamic coupling influences the dynamics of colloidal particles in a fluctuating ratchet potential within a toroidal trap. We use the Rotne-Prager approximation to incorporate hydrodynamic interactions in our Brownian dynamics simulations. For spatially constant transition rates, we demonstrate that hydrodynamic interactions increase the mean velocities only if the particles change their ratchet state individually rather than simultaneously. We explain the mechanisms how hydrodynamic coupling among particles in different ratchet states causes the enhanced ratchet effect. For localized transition rates, we show that hydro-

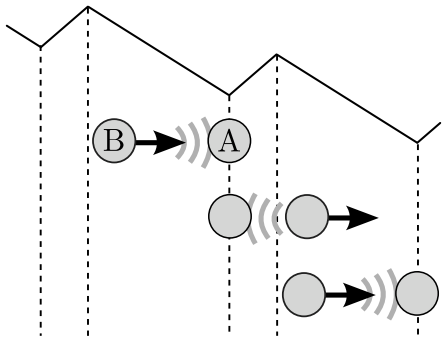

Figure 5.1: Sequence of interactions for caterpillar-like motion of a pair of colloidal particles in a static tilted sawtooth potential. The front and rear particle is labeled A and B, respectively. The arrows show the drift direction due to the potential and the grey arcs symbolize hydrodynamic interactions between the particles. The picture is explained in detail in the main text.

dynamic interactions can induce the formation of transient clusters traveling with velocities more than ten times faster than a single particle. Further, we identify the underlying sequence of hydrodynamic interactions causing the observed cluster formation. This cluster formation indeed has some remarkable reminiscence of the discussed caterpillar-like motion.

5.2 Model and numerical implementation

We choose a toroidal trap as a model system since such a system has already been used for related numerical studies of hydrodynamic phenomena in colloidal systems and has been realized experimentally [39, 103]. In particular, the experiments with colloids in a tilted sawtooth potential have been done in a toroidal trap [87].

5.2.1 Toroidal trap

The toroidal trap contains N spherical particles with radius σ. Their positions are specified by cylindrical coordinates (r, ϕ, z) and $\boldsymbol{r}$ is the positional vector. A harmonic trap potential V_{trap} of the form

$$V_{\text{trap}} = \frac{A}{2} \left[(r - R)^2 + z^2\right] \tag{5.1}$$

keeps the particles on a circle with radius R. In the following, we chose A such that the particles are not able to change their sequential order.

The interaction between the particles is modeled with a soft repulsive potential V_{rep} of the form

$$V_{\text{rep}} = B \left[\left(\frac{r_{ij}}{2\sigma} \right)^{12} - 1 \right]^{-1}. \tag{5.2}$$

as introduced in Eq. 2.87. Here, $r_{ij} = |\boldsymbol{r}_i - \boldsymbol{r}_j|$ is the center-center distance between particles i and j. In the following, we chose B such that the minimal distance during the simulations is approximately 3σ. A trap with radius $R = 20\sigma$ and 30 particles is depicted in Fig. 5.2 (a).

5.2.2 Ratchet potential and transition rates

A sawtooth-type ratchet potential $V_{\text{rat}}(\phi, t)$ is imposed in tangential direction. As illustrated in Fig. 5.2 (b), the ratchet potential is characterized by the angular period L_ϕ, the asymmetry parameter a, and the amplitude $\hat{V}_{\text{rat}}$ (see also Eq. (2.47)). The number of potential minima N_{min} determines the angular period $L_\phi = 2\pi/N_{\text{min}}$ and the asymmetry parameter a is defined as the ratio between the width of the short side of the sawtooth and the period L_ϕ. Finally,

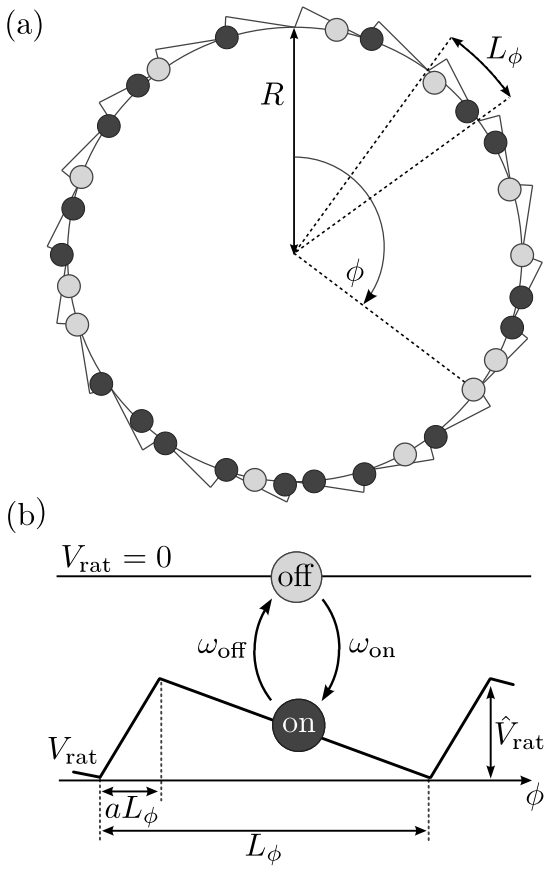

Figure 5.2: (a) Toroidal trap with $N = 30$ particles and radius $R = 20\sigma$. A ratchet potential with $N_{\mathrm{min}} = 20$ minima and asymmetry parameter $a = 0.1$ is schematically indicated. (b) The two states of the ratchet potential V_{rat}: the off-state with zero potential and the on-state with a sawtooth potential characterized by the angular period L_ϕ, the potential amplitude $\hat{V}_{\mathrm{rat}}$, and the asymmetry parameter a. The stochastic transition between both states is governed by the transition rates ω_{on} and ω_{off}.

for a given trap radius R, the spatial period of the sawtooth potential is $L = RL_\phi = 2\pi R/N_{\mathrm{min}}$.

As discussed in Sec. 2.3.3, several models for the time-dependence of the ratchet potential are known in literature. In this chapter, we use a fluctuating ratchet potential. In such a ratchet, the potential changes stochastically between two states: the on-state, in which the particle feels a force according to the ratchet potential V_{rat}, and the off-state, in which the particle diffuses

freely along the trap. The transition between both states is governed by the rates ω_{on} and ω_{off}. We investigate two different scenarios for the stochastic transitions. In the first scenario, the ratchet state changes simultaneously for all particles and they are always in the same state. In the second scenario, each particle changes its state individually. As a consequence, particles in different states coexist in the trap. We further introduce the position-dependent transition rate $\hat{\omega}_{\mathrm{off}}(\phi)$ such that the rate is increased to $\omega_{\mathrm{off}}\, b$ in a narrow interval around each minimum, while it is decreased to ω_{off}/b anywhere else along the circle. The interval has the width of 1 deg and is centered around each minimum. This position dependence localizes the transitions from the on to the off-state in the vicinity of the potential minima. The parameter $b > 1$ defines the strength of this localization. For $b = 1$, the transition rate does not depend on the particle position.

For all simulations, we set the potential amplitude to $\hat{V}_{\mathrm{rat}}/k_{\mathrm{B}}T = 100$ where $k_{\mathrm{B}}T$ is the thermal energy. As a consequence, the induced drift by the ratchet potential dominates the motion of particles in the on-state.

5.2.3 Hydrodynamic interactions

As discussed in Sec. 2.5.1, forces acting on particles also influence all the other particles through induced flow fields. Due to the linearity of the Stokes equations, the translational velocities $\dot{\boldsymbol{r}}_i$ depend linearly on the external forces $\boldsymbol{f}_j$ acting on all particles. The velocity of particle i can be written as

$$\dot{\boldsymbol{r}}_i = \sum_{j=1}^{N} \boldsymbol{\mu}_{ij}(\boldsymbol{r}_1, \ldots, \boldsymbol{r}_N)\boldsymbol{f}_j. \tag{5.3}$$

The hydrodynamic coupling of the translating particles is described by 3×3 mobility tensors $\boldsymbol{\mu}_{ij}$.

In our quasi-one-dimensional system, hydrodynamic interaction mainly has the following effects. Consider three particles in the toroidal trap, with the particle in the middle being driven by an external force along the channel. The two adjacent particles only feel the trap potential. Whereas the particle in the middle pushes the preceding particle forward by its drift motion, due to hydrodynamic interaction it can also pull the succeeding particle forward for a certain time.

5.2.4 Langevin equation

The total external force on particle i is given by the sum of the trap force, the repulsive forces, and the ratchet force which we derive from the potentials defined in Eqs. (5.1), (5.2), and in Sec. 5.2.2:

$$\boldsymbol{f}_i = \boldsymbol{f}_{\mathrm{trap},i} + \boldsymbol{f}_{\mathrm{rat},i} + \sum_j \boldsymbol{f}_{\mathrm{rep},ij}. \tag{5.4}$$

In analogy to Sec. 2.5.3, we combine the individual forces $\boldsymbol{f}_i$ and positions $\boldsymbol{r}_i$ of the particles to the $3N$-dimensional vectors $\mathbf{f} = (\boldsymbol{f}_1, \ldots, \boldsymbol{f}_N)$ and $\mathbf{r} = (\boldsymbol{r}_1, \ldots, \boldsymbol{r}_N)$, respectively. Then, the particle trajectories of the N particle system are governed by the Langevin equation

$$\mathbf{Z}(\mathbf{r})\,\dot{\mathbf{r}} = \mathbf{f}(\mathbf{r}, t) + \boldsymbol{\xi}(t). \tag{5.5}$$

Table 5.1: List of simulation parameters and the corresponding time and velocity scales. The diffusion time is given for $a = 0.1$.

Particle radius σ	0.5	μm
Trap radius R	10	μm
Trap coefficient A	$5 \cdot 10^{-7}$	Nm^{-1}
Repulsion coefficient B	$7.5 \cdot 10^{-19}$	Nm
Temperature T	300	K
Viscosity η	10^{-3}	Pa s
Potential amplitude $\hat{V}_{\mathrm{rat}}$	$4.1 \cdot 10^{-19}$	Nm
Number of minima N_{min}	20	
Drift velocity v_{drift}	15.5	$\mu\mathrm{ms}^{-1}$
Drift time t_{drift}	0.18	s
Diffusion time t_{diff}	0.22	s

The stochastic force $\boldsymbol{\xi}(t)$ is unbiased $\langle \boldsymbol{\xi}(t) \rangle = 0$ and its autocorrelation function obeys the fluctuation-dissipation theorem

$$\langle \boldsymbol{\xi}(t) \otimes \boldsymbol{\xi}(t') \rangle = 2 k_{\mathrm{B}} T \, \mathbf{Z}(\mathbf{r}) \, \delta(t - t'). \tag{5.6}$$

5.2.5 Numerical methods

For the numerical integration the Langevin equation, we use the algorithm of Ermak and McCammon [37]. The change of the particle positions after one simulation step during time interval $\mathrm{d}t$ is given by

$$\mathrm{d}\mathbf{r} = \mathbf{M}\,\mathbf{f}\,\mathrm{d}t + \mathbf{A}\,\mathrm{d}\mathbf{w}. \tag{5.7}$$

The mobility matrix $\mathbf{M}$, the amplitude matrix $\mathbf{A}$ and the Wiener increment $\mathrm{d}\mathbf{w}$ have been discussed in Sec. 2.5.4. The complete list of parameters for the performed simulations is given in Table 5.1.

In order to analyze the particle dynamics, we calculate the mean velocity

and the velocity auto-correlation function from the simulated particle trajectories. Based on the angular positions of the particles at the beginning ($\phi(0)$) and the end ($\phi(T)$) of the simulation, the mean velocity is given by

$$\langle v \rangle = \frac{R}{N} \sum_{i=1}^{N} \frac{\phi_i(T) - \phi_i(0)}{T}. \tag{5.8}$$

Here, $\phi_i(t)$ is a continuous angular trajectory. It grows beyond the angle 2π, so it is not reset each time the particle passes $\phi = 0$. For all simulations in this article the simulation time T was chosen such that at least 10^4 individual ratchet cycles occured. The velocity auto-correlation function is defined as

$$c(\tau) = \frac{1}{N} \sum_{i=1}^{N} \frac{\langle \Delta v_i(t) \Delta v_i(t+\tau) \rangle}{\sqrt{\langle \Delta v_i(t)^2 \rangle \langle \Delta v_i(t+\tau)^2 \rangle}} \tag{5.9}$$

with

$$\Delta v_i(t) = v_i(t) - \langle v \rangle. \tag{5.10}$$

5.3 Ratchet dynamics of a single particle

In this section, we discuss the dynamics of a single particle in the fluctuating ratchet potential. The single particle system serves as a reference for the multi-particle systems which we discuss for spatially constant and localized transition rates in Secs. 5.4 and 5.5.

In contrast to the on-off ratchet discussed in Sec. 2.3.2, the sawtooth potential switches stochastically between the on and the off-state, rather than cyclically. However, the underlying mechanism of the ratchet effect remains unchanged. Again, the interplay between deterministic drift caused by the asymmetric potential and unbiased diffusion leads to a rectification of Brow-

nian motion in the fluctuating ratchet. We consider a particle that has just changed to the off-state and assume a ratchet potential with asymmetry parameter $a < 1/2$. In the off-state, the particle diffuses freely along the trap. We now derive the probability density function for the particle to be at a certain position when it changes back to the on-state. First, the probability density function for the particle to change to the on-state after time t has elapsed is given by

$$p_{\mathrm{on}}(t) = w_{\mathrm{on}} \exp(-\omega_{\mathrm{on}} t). \tag{5.11}$$

Hence, the average time the particle spends in the off-state is

$$\langle t_{\mathrm{off}} \rangle = \int_0^\infty p_{\mathrm{on}}(t) t \, \mathrm{d}t = 1/\omega_{\mathrm{on}}. \tag{5.12}$$

Second, the probability density function to find the particle displaced by $\Delta\phi$ from its initial position ϕ_0 after time t has elapsed is given by a Gaussian distribution

$$\mathcal{D}(\Delta\phi, t) = \frac{1}{\sqrt{4\pi D_\phi t}} \exp\left(-\frac{(\Delta\phi)^2}{4 D_\phi t}\right), \tag{5.13}$$

where $D_\phi = D/R^2$ is the diffusion constant for angular diffusion along the circular trap. Eventually, the probability density to find the particle displaced by $\Delta\phi$ from its initial position ϕ_0 when it returns to the on-state is given by

$$\begin{aligned} \mathcal{P}(\Delta\phi) &= \int_0^\infty p_{\mathrm{on}}(t) \mathcal{D}(\Delta\phi, t) \mathrm{d}t \\ &= \sqrt{\frac{\omega_{\mathrm{on}}}{4 D_\phi}} \exp\left(-\sqrt{\frac{\omega_{\mathrm{on}}}{D_\phi}} |\Delta\phi|\right). \end{aligned} \tag{5.14}$$

This function is symmetric and gives zero mean displacement as expected from free diffusion. However, due to the asymmetry of the ratchet potential and

a mean bias of the initial position ϕ_0 towards a local mimimum, the fraction of $\mathcal{P}(\Delta\phi)$ reaching into a neighboring spatial period is larger in clockwise direction. As a consequence, the particle will on average travel clockwise along the trap in absence of any net force in this direction. The resulting mean velocity $\langle v \rangle$ defined in Eq. (5.8) is the main measure in this article. As a reference velocity, we introduce the velocity

$$v_{\mathrm{drift}} = \mu \hat{V}_{\mathrm{rat}}/[(1-a)L] \tag{5.15}$$

of a single particle solely driven by the force $\hat{V}_{\mathrm{rat}}/[(1-a)L]$ that is exerted by the longer slope of the ratchet potential. Further we rescale the transition rate ω_{on} by the inverse of the time

$$t_{\mathrm{diff}} = (aL)^2/D \tag{5.16}$$

a particle needs to diffuse an average distance $aL/2$. The transition rate ω_{off} rate is referred to the inverse of the drift time

$$t_{\mathrm{drift}} = (1-a)L/v_{\mathrm{drift}} \tag{5.17}$$

a particle spends on the longer slope of the ratchet potential. The numeric values of t_{drift}, v_{drift} and t_{diff} are given in Table 5.1.

Figure 5.3 (a) depicts simulation results for the rescaled mean velocity $\langle v \rangle / v_{\mathrm{drift}}$ as a function of $\omega_{\mathrm{on}}\, t_{\mathrm{diff}}$ for several values of the asymmetry parameter a. As discussed in Sec. 2.3.2, more asymmetric ratchet potentials, *i.e.*, those with smaller values of a, lead to larger mean velocities. The maximum mean velocity occurs for a transition rate $\omega_{\mathrm{on}} \approx t_{\mathrm{diff}}$ that gives the particle a

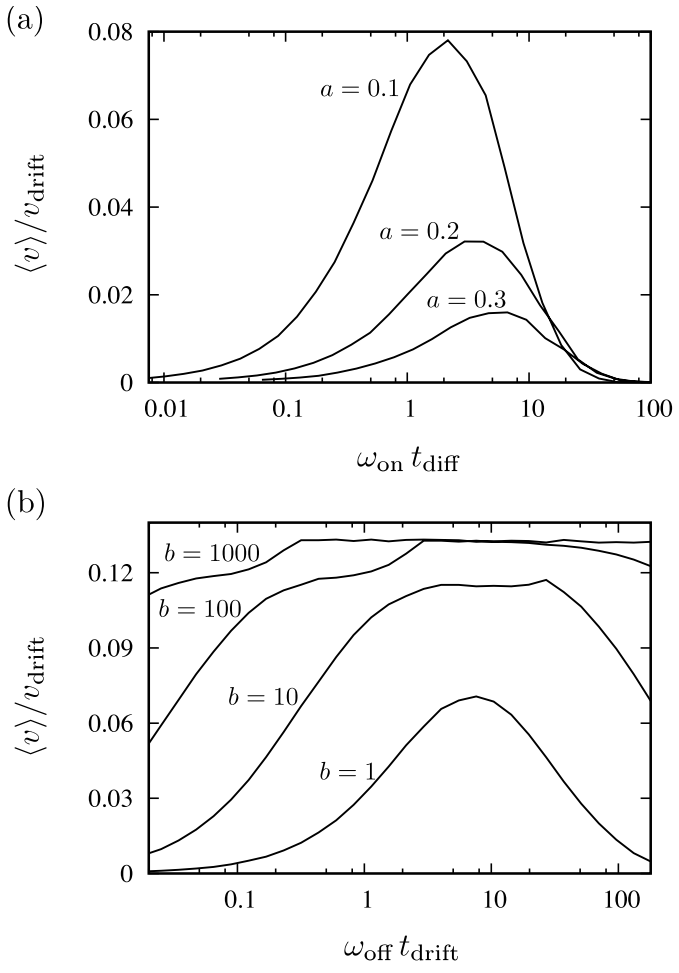

Figure 5.3: Rescaled mean velocity $\langle v\rangle/v_{\mathrm{drift}}$ of a single particle, (a) as a function of $\omega_{\mathrm{on}}\, t_{\mathrm{diff}}$ for $a = 0.1, 0.2$ and 0.3 with $\omega_{\mathrm{off}}\, t_{\mathrm{drift}} = 3.6$ and $b = 1$. (b) as a function of $\omega_{\mathrm{off}}\, t_{\mathrm{drift}}$ for $b = 1, 10, 100$ and 1000 with $\omega_{\mathrm{on}}\, t_{\mathrm{diff}} = 4.5$ and $a = 0.1$.

significant chance to reach the next spatial period by diffusion and keeps the duration of the off-state short.

Figure 5.3 (b) shows the simulation results for the rescaled mean velocity $\langle v\rangle/v_{\mathrm{drift}}$ as a function of $\omega_{\mathrm{off}}\, t_{\mathrm{drift}}$ for several values of the localization parameter b. For a spatially constant transition rate ($b = 1$), the mean velocity has a maximum value for $\omega_{\mathrm{off}}\, t_{\mathrm{drift}} \approx 10$. This means that for maximizing the mean velocity, it is rather beneficial to change to the off-state before reaching the

minimum of the potential than being trapped at the minimum. For localized transition rates with $b > 1$, the mean velocities significantly increase and the maximum velocity occurs for a wider range of values ω_{off}. For $b = 100$, the maximum velocity reaches its maximum value. For very large values of b this value is reached virtually independent of ω_{off}. The mean velocity increases since the performance of the ratchet is optimized by the localized transition rate $\hat{\omega}_{\text{off}}(\phi)$. On the one hand, the localization reduces the probability for a particle to change to the off-state before it reaches the potential minimum and hence increases the displacement during the on-state. On the other hand, the localization increases the probability to change to the off-state as soon as the potential minimum is reached. This keeps the time short during which the particle is trapped in the potential minimum.

For sufficiently large values of b, the particle will virtually always drift all the way towards the minimum and immediately change to the off-state. This optimized ratchet cycle gives the observed maximum value $\langle v \rangle / v_{\text{drift}} \approx 0.13$ for the mean velocity in Fig. 5.3. As expected, this value is still smaller than the deterministic drift velocity v_{drift} even for highly optimized ratchet cycles. However, we will show in the subsequent sections that the ratio $\langle v \rangle / v_{\text{drift}}$ increases significantly in multi-particle systems and even surpasses parity for localized transition rates.

5.4 Spatially constant transition rates

We now investigate multi-particle effects on the ratchet dynamics, in particular the effect of hydrodynamic interactions among the particles. We consider a ratchet potential with spatially constant transition rates and compare two

scenarios where particles change the ratchet state either simultaneously or individually.

We first present the results when all particles always occupy the same state. Figure 5.4 depicts the rescaled mean velocity $\langle v \rangle / v_{\mathrm{drift}}$ as a function of the rescaled transition rate $\omega_{\mathrm{on}}\, t_{\mathrm{diff}}$ for various particle numbers. With $\omega_{\mathrm{off}}\, t_{\mathrm{drift}} = 3.6$, the transition rate ω_{off} has been chosen such that the mean velocity is close to the corresponding maximal value for any value of ω_{on}.[1] Panel (a) shows the simulation results when hydrodynamic interactions are neglected while in panel (b) hydrodynamic interactions are included. The maximum mean velocity is virtually unchanged for $N = 1, 10, 20$ and 30 particles. For $N = 40$ particles, the maximum mean velocity even drops by a factor of 0.6 compared to the single particle system. Hydrodynamic interactions hardly influence this behavior. Two effects due to the fixed sequential order of the particles in the toroidal trap reduce the mean velocity for large particle numbers. First, single-file diffusion occurs with sub-diffusional behavior of the mean square displacement $\langle \Delta\phi \rangle^2 \sim t^{1/2}$. which is most pronounced when the particle number is large [71, 119]. This slows down the spreading of the particle distribution function during the off-state and hence the mean velocity is reduced. Second, for large particle numbers the probability that two or more particles drift towards the same minimum increases. Since only one particle can occupy the position at the minimum, the drift of the other particles is hindered. This decreases the mean velocity not only by reducing the mean drift length but also by increasing the mean distance to the neighboring potential minimum.

[1] As shown in Fig. 5.3 (b), the choice of $\omega_{\mathrm{off}}\, t_{\mathrm{drift}} = 3.6$ leads to a mean velocity close to the maximum. However, the precise position of the maximum depends further on the values of ω_{on} and N. Our choice has been made empirically such that the mean velocity is close to the maximum (with respect to ω_{off}) for all considered combinations of ω_{on} and N.

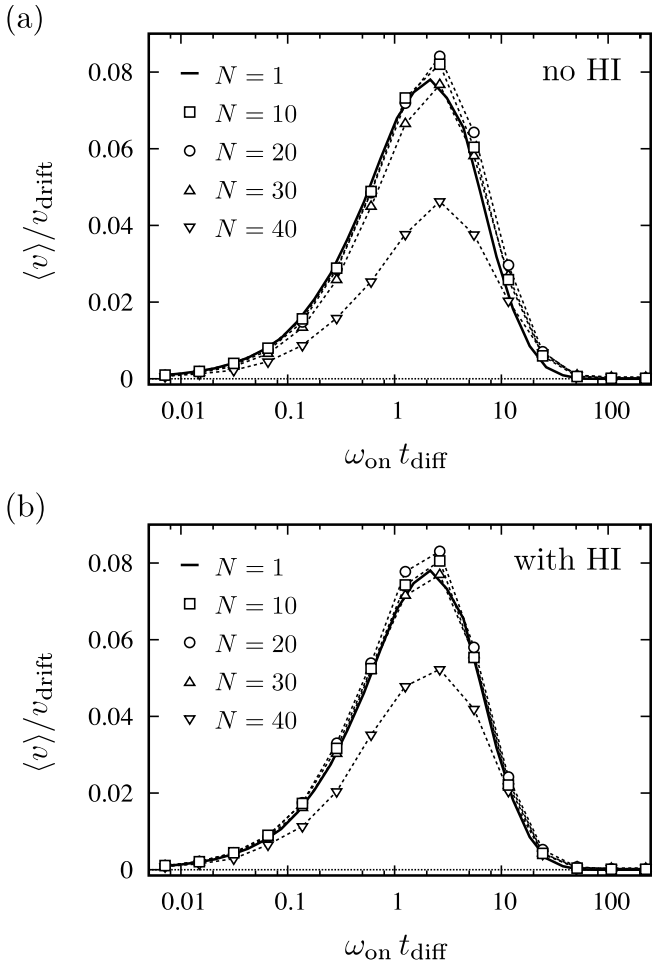

Figure 5.4: Rescaled mean velocity $\langle v \rangle / v_{\mathrm{drift}}$ as a function of $\omega_{\mathrm{on}}\, t_{\mathrm{diff}}$ when particles change their ratchet states simultaneously. Simulation results for different particle numbers $N = 1$ (solid line), $N = 10$ ($\square$), $N = 20$ ($\circ$), $N = 30$ ($\triangle$), and $N = 40$ ($\triangledown$) are plotted. Parameters are $\omega_{\mathrm{off}}\, t_{\mathrm{drift}} = 3.6$, $a = 0.1$, and $b = 1$. (a) without hydrodynamic interactions, (b) with hydrodynamic interactions.

The system's response for increasing particle numbers changes crucially when individual transitions of the particles between the ratchet states are allowed. For this scenario, Fig. 5.5 illustrates the rescaled mean velocity $\langle v \rangle / v_{\mathrm{drift}}$ as a function of the rescaled transition rate $\omega_{\mathrm{on}}\, t_{\mathrm{diff}}$ for various particle numbers. Panel (a) shows the simulation results when hydrodynamic interactions are neglected. Here, the maximum mean velocity increases with

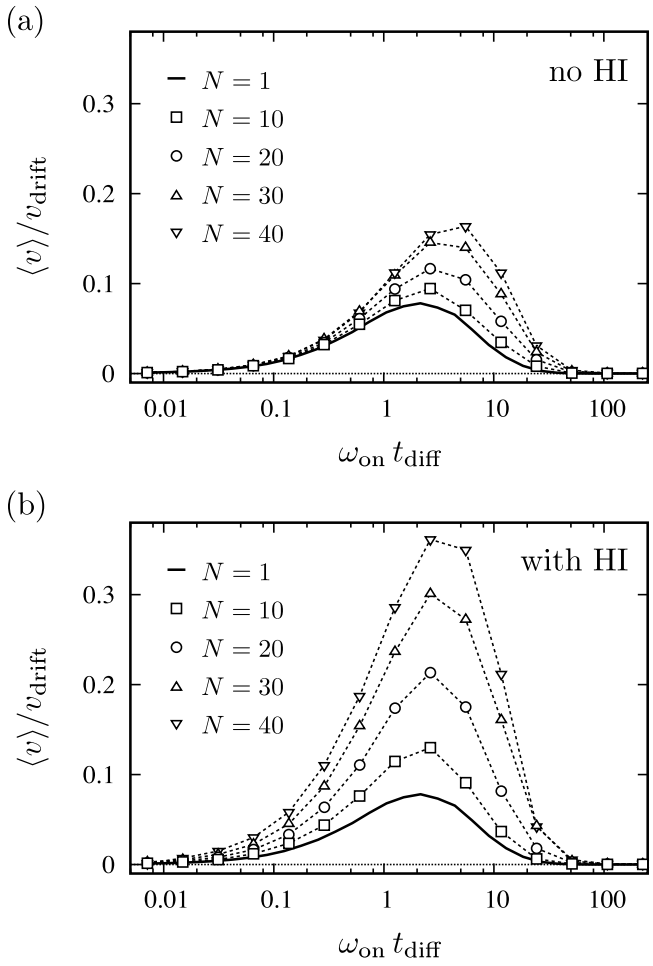

Figure 5.5: Rescaled mean velocity $\langle v \rangle / v_{\mathrm{drift}}$ as a function of $\omega_{\mathrm{on}}\, t_{\mathrm{diff}}$ when particles change their ratchet states individually. Simulation results for different particle numbers $N = 1$ (solid line), $N = 10$ ($\square$), $N = 20$ ($\circ$), $N = 30$ ($\triangle$), and $N = 40$ ($\triangledown$) are plotted. Parameters are $\omega_{\mathrm{off}}\, t_{\mathrm{drift}} = 3.6$, $a = 0.1$, and $b = 1$. (a) without hydrodynamic interactions, (b) with hydrodynamic interactions.

growing particle number. For $N = 40$ particles, $\langle v \rangle / v_{\mathrm{drift}}$ is larger than the single-particle value by a factor of 2.2. Panel (b) shows the simulation results when hydrodynamic interactions are included. In contrast to the system with simultaneous transitions, hydrodynamic interactions now lead to a further significant increase of the mean velocity. For $N = 40$ particles, the mean velocity is larger by a factor of about 4.7 compared to the single-particle velocity. The

following consideration provides a qualitative understanding why the mean velocity increases when particles can switch individually between the on- and off-state. Particles in the on-state can push neighboring particles in the off-state due to repulsive interactions. Since the ratchet effect induces a mean drift clockwise along the longer potential slope, particles in the off-state are more likely pushed clockwise. When hydrodynamic interactions are included, drifting particles can also pull neighboring particles along which further enhances the mean velocity.

In order to analyze this mechanism quantitatively, we consider in Fig. 5.6 the probability density function $\mathcal{P}(\Delta\phi)$ for a particle to move a distance $\Delta\phi$ along the circle during off-time. The two graphs illustrate numerical results for $N = 1$, 20, and 40 particles and compare them to the theoretical prediction of Eq. (5.14) for a single-particle system (full line). In panel (a) hydrodynamic interactions are not included. For $N = 1$, simulations give a symmetric and unbiased probability density $\mathcal{P}(\Delta\phi)$ in good agreement with the theoretical curve. For larger particle numbers the distribution is shifted towards positive values, *i.e.*, clockwise, whereby the induced bias increases with the number of particles. To be concrete, the mean value of the distribution is $\langle\Delta\phi\rangle = 0.2\,\mathrm{deg}$ for $N = 20$ particles and $\langle\Delta\phi\rangle = 0.51\,\mathrm{deg}$ for 40 particles. As a consequence, the probability for a particle to reach the neighboring potential minimum during the off-state and hence the mean velocity increases. Panel (b) shows the results when hydrodynamic interactions are included in the simulations. The induced bias of the probability distribution is further enhanced. For $N = 20$ particles, the mean value of the distribution is $\langle\Delta\phi\rangle = 0.46\,\mathrm{deg}$ for $N = 20$ particles and $\langle\Delta\phi\rangle = 1.0\,\mathrm{deg}$ for 40 particles. These mean values are now of the order of the length of the short slope of the ratchet potential

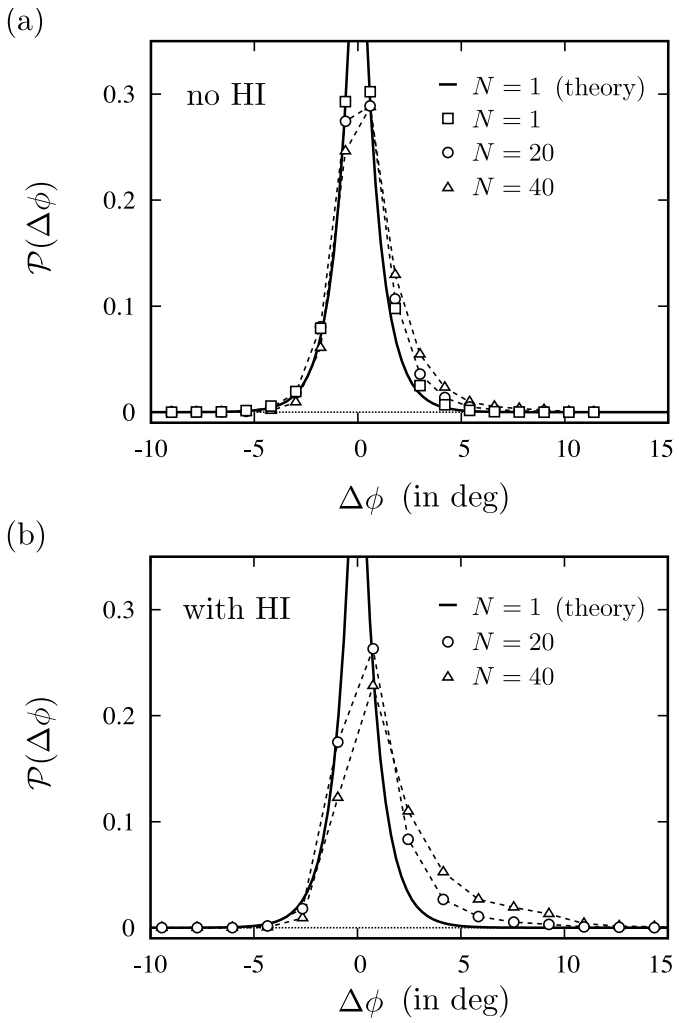

Figure 5.6: The probability density function $\mathcal{P}(\Delta\phi)$ for a particle displacement $\Delta\phi$ at the moment when the particle changes to the on-state determined from the same simulation data as the graphs of Fig. 5.5. The curves belong to particle numbers $N = 1$ ($\square$), $N = 20$ ($\circ$), and $N = 40$ ($\triangle$), and the full line corresponds to the analytic expression of Eq. (5.14) for a single particle. (a) Without hydrodynamic interactions, (b) with hydrodynamic interactions.

($aL_\phi = 1.8\,\mathrm{deg}$). It is noteworthy that the distribution is not symmetric any longer and the probability for particles to be displaced by more than 5 deg is increased significantly. The long-range character of hydrodynamic interactions explains the enhanced bias of the distribution. A drifting particle not only pushes diffusing particles without being in direct contact but also

pulls diffusing particles. Both mechanisms lead eventually to the observed increase of the mean velocities. In other words, the hydrodynamic coupling enhances the induced bias in diffusion.

We want to stress that this induced bias does not occur when all particles change their ratchet states simultaneously since then drifting particles cannot influence the diffusion of particles in the off-state. Individual transitions between the ratchet states are therefore a crucial requirement for the ratchet effect being enhanced by hydrodynamic coupling.

5.5 Localized transition rates

In this section, we demonstrate that hydrodynamic interactions in combination with a localized transition rate $\hat{\omega}_{\text{off}}(\phi)$ initiate the formation of transient particle clusters that move at high velocities. The underlying mechanism goes beyond the previously discussed induced bias in the diffusional off-state. Of course, the model is only realizable when the transitions between the on- and off-state occur individually for each particle. The transition rate from the on- to the off-state is $\omega_{\text{off}} b$ when the particle reaches a potential minimum and ω_{off}/b otherwise.

Figure 5.7 shows the velocity $\langle v \rangle$ in units of both v_{drift} and the one-particle value $\langle v \rangle_{N=1}$ as a function of the particle number N when hydrodynamic interactions are included as well as neglected. For the localization parameter $b = 100$, $\omega_{\text{on}}\, t_{\text{diff}} = 4.5$, and $\omega_{\text{off}}\, t_{\text{drift}} = 3.6$ the ratchet operates close to its maximum velocity. In both cases, the mean velocity increases with the particle number N. For 40 particles, the mean velocity is larger by a factor of 4.4 than the one-particle value when hydrodynamic interactions are neglected;

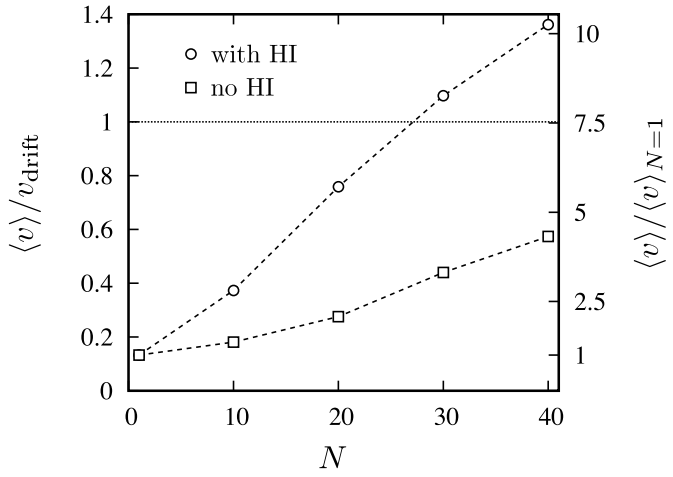

Figure 5.7: Mean velocity $\langle v\rangle$ in units of $v_{\rm drift}$ (left ordinate) and $\langle v\rangle_{N=1}$ (right ordinate) as a function of particle number N. The parameters are $\omega_{\rm on}\, t_{\rm diff} = 4.5$, $\omega_{\rm off}\, t_{\rm drift} = 3.6$, $a = 0.1$, and $b = 100$. The symbols refer to simulation results including (○) and without (□) hydrodynamic interactions, respectively.

in the presence of hydrodynamic interactions the factor assumes 10.3. It is remarkable that the mean velocity for $N \geq 30$ even surpasses the deterministic drift velocity $v_{\rm drift}$ when hydrodynamic interactions are included. In other words, the particles in the ratchet potential move faster than a single particle would travel that is driven by a constant force exerted by the longer slope of the ratchet potential. It is known that particles under the influence of a constant force in a toroidal trap move faster than a single particle due to reduced hydrodynamic drag [103]. In the following we discuss how clusters of particles in a ratchet potential can partially benefit from such a drag reduction and eventually surpass the velocity $v_{\rm drift}$.

In order to reveal the underlying mechanism, we consider the example trajectories in Fig. 5.8 for a system with $N = 20$ particles. One set of trajectories is based on simulations including hydrodynamic interactions (HI); they have been neglected in the other set. The close-up of the trajectories in panel (b) (with HI) features strong variations in the particle density. In

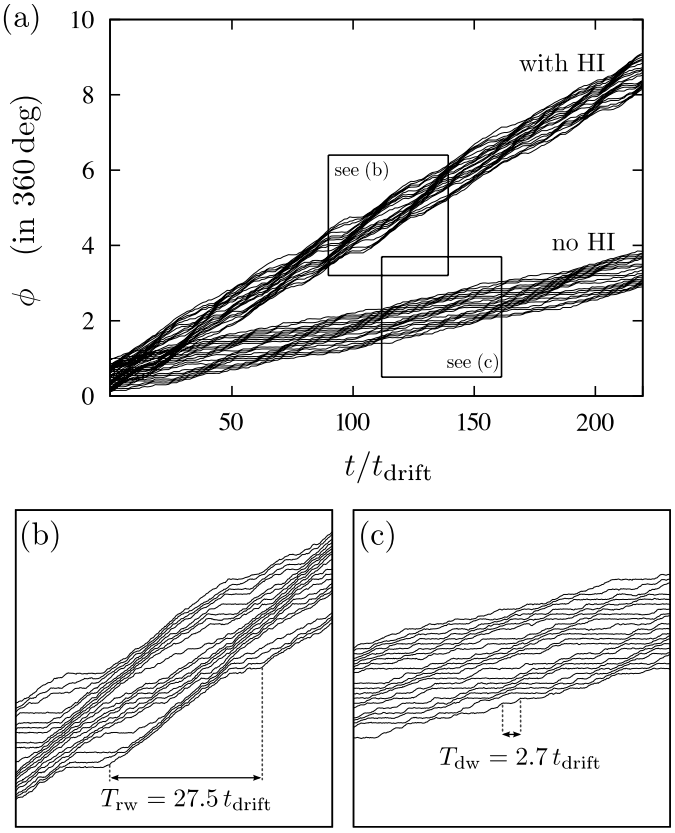

Figure 5.8: (a) Particle trajectories $\phi(t)$ of $N = 20$ particles in the toroidal trap. The upper and lower set of trajectories refer to simulations where hydrodynamic interactions (HI) are included or neglected , respectively. The parameters are $a = 0.1$, $b = 100$, $\omega_{\rm on}\, t_{\rm diff} = 4.5$, and $\omega_{\rm off}\, t_{\rm drift} = 3.6$. The boxes indicate close-ups of the trajectories in panels (b) and (c). Examples of the run-walk cycle with duration $T_{\rm rw}$ and the drift-wait cycle with duration $T_{\rm dw}$ are indicated in (b) and (c), respectively.

other words, clusters of particles with short distances occur spontaneously in the circular trap. These clusters travel with remarkably high velocities before they dissolve. The number of particles in such a transient cluster is not fixed. Rather, new particles join the cluster from the front and others are left behind at the rear end. When hydrodynamic interactions are neglected, as in panel (c), the spontaneous formation of transient clusters is not visible.

For a pair of particles, we explain in Fig. 5.9 how hydrodynamic interactions

induce the formation of transient clusters which are then able to move with high velocities. We denote the particle in front with A and assume that it is located at the minimum of the ratchet potential where it has just switched into the off-state (grey). The second particle B is in the on-state (black) and drifts towards the minimum. It reaches the minimum without changing the state, due to the localization of $\hat{\omega}_{\mathrm{off}}$, and pushes particle A forward beyond the location of the potential barrier. Note that particle A needs to be in the off-state for this step. When particle B reaches the minimum, it immediately changes to the off-state. Ultimately, particle A assumes the on-state and drifts towards the next minimum. While doing so, it uses hydrodynamic interactions to pull particle B beyond the location of the potential barrier. When particle A arrives at the next minimum and when particle B changes to the on-state, the initial configuration is reached; the cluster has moved one spatial period. Without hydrodynamic interactions this sequence is interrupted, as the leading particle A is not able to pull B while drifting into the next minimum and the cluster breaks up.

The motional pattern just described resembles the caterpillar-like motion that has been observed for colloidal particles in tilted sawtooth potentials [87]. The latter describes a fully deterministic pattern only disturbed by Brownian motion whereas the motion of the transient clusters has intrinsic stochastic elements: diffusion during the off-state and stochastic transition to the on-state. This stochastic character is the major difference to the caterpillar dynamics in Ref. [87]. The cluster dynamics has been demonstrated for a pair of particles. The presence of additional particles stabilizes the cluster since several pushing particles at the rear end and pulling particles at the front increases the probability that the cycle illustrated in Fig. 5.9 repeats itself.

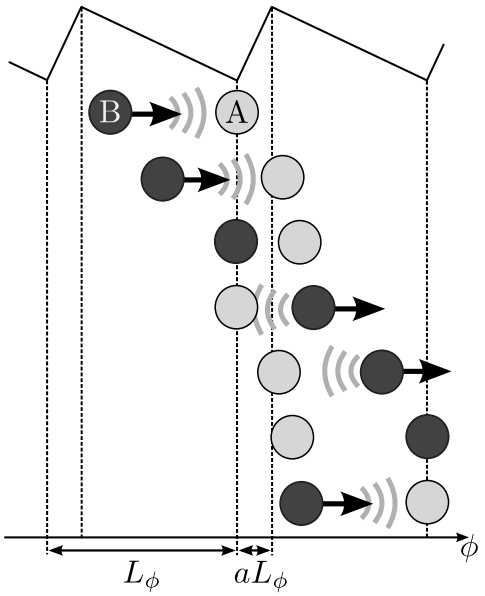

Figure 5.9: Transient cluster formation of a pair of particles using hydrodynamic interactions. The front and rear particles are labeled A and B, respectively. The colors of the particles indicate the on-state (black) and the off-state (grey) in the ratchet cycle. The arrows show the drift direction in the ratchet potential and the grey arcs symbolize hydrodynamic interactions between the particles. The picture is explained in detail in the main text.

Particles traveling in the observed clusters perform repetitive *drift-wait* cycles: They *drift* in the on-state to the next minimum, and subsequently *wait* until they are either pushed or pulled into the neighboring period by a front or rear particle, respectively. Note, that the waiting period might last multiple ratchet cycles, as the particle might fail to reach the next period during the off-time. In addition to this short-period drift-wait cycle, particles perform long-period *run-walk* cycles, where they *run* with high velocity as part of a cluster until they are left behind. Then, they *walk* as single particles with velocities lower than the overall mean velocity, until they join another cluster. When hydrodynamic interactions are neglected, the characteristic cluster formation does not occur but particles still perform drift-wait cycles. Since no

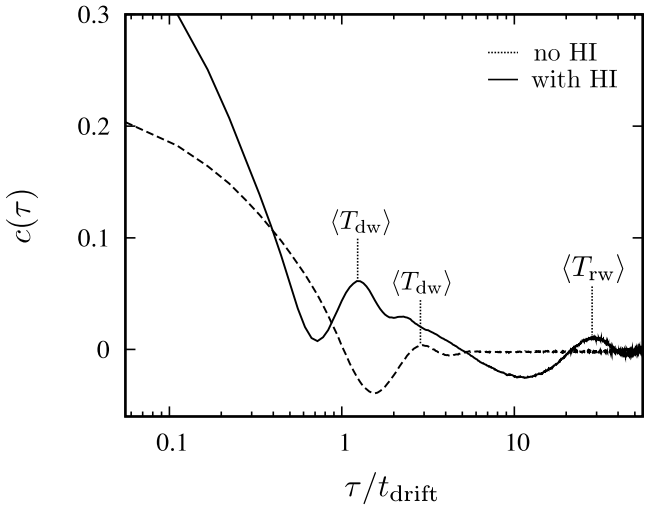

Figure 5.10: Velocity auto-correlation functions $c_n(\tau)$ as a function of the rescaled time lag τ/t_{drift}. Solid and dotted lines refer to data including and neglecting hydrodynamic interactions, respectively. The mean cycle periods $\langle T_{\mathrm{dw}} \rangle$ and $\langle T_{\mathrm{rw}} \rangle$ are indicated by the arrows in units of t_{drift}.

hydrodynamic pulling occurs, particles wait in the vicinity of a potential minimum until they reach the next period either by diffusion or by being pushed by a rear particle. In Fig. 5.8 (b), an exemplary run-walk and drift-wait cycle are indicated, respectively. The drift-wait cycles for included hydrodynamic interactions in panel (b) are too short to be properly visualized in the same figure.

The discussed cycles cause velocity signals with alternating intervals of velocities larger and smaller than the mean velocity. If such oscillations in the signal have a predominant period, oscillations with the same period will appear in the velocity auto-correlation function defined in Eq. (5.9).[2] We use this relation to obtain statistic information about the discussed cycles. The velocity auto-correlation function $c(\tau)$ based on simulations with $N = 20$ particles is depicted in Fig. 5.10. For included hydrodynamic interactions, the

[2]In the considered case, the oscillations in the auto-correlation function decay due to the stochastic nature of the velocity signal.

correlation data indeed features two superimposed oscillations with different periods. The period of the fast oscillation corresponds with the mean period of the drift-wait cycle $\langle T_{\mathrm{dw}} \rangle$, whereas the slow oscillation refers to the run-walk cycle with its mean period $\langle T_{\mathrm{rw}} \rangle$. From the correlation data, the mean periods have been found to be $\langle T_{\mathrm{rw}} \rangle = 28.6\, t_{\mathrm{drift}}$ and $\langle T_{\mathrm{dw}} \rangle = 1.15\, t_{\mathrm{drift}}$, respectively. Note, that the latter is smaller than the sum of the drift time and the mean off-time $t_{\mathrm{drift}} + \langle t \rangle_{\mathrm{off}} = 1.27\, t_{\mathrm{drift}}$. This comparison reveals two characteristics of the drift-wait cycle. Since the mean off-time is not influenced by the cluster dynamics, the actual drift time $\langle T_{\mathrm{dw}} \rangle - \langle t \rangle_{\mathrm{off}} = 0.88\, t_{\mathrm{drift}}$ is, in average, smaller than the drift time which was calculated for a single particle. This indicates that the drift velocities are increased in multi-particle systems due to screening of hydrodynamic drag. Second, one off-time occurs in average per drift-wait cycle. In other words, the particle skips to the next period virtually every ratchet cycle while traveling in the cluster.

For neglected hydrodynamic interactions, the correlation data features only one oscillation, which corresponds to the drift-wait cycle. Here, the mean period has been found to be $\langle T_{\mathrm{dw}} \rangle = 2.75\, t_{\mathrm{drift}}$ which is significantly larger than the drift-wait cycle for included hydrodynamic interactions. This is mainly because, the lack of hydrodynamic pulling decreases the probability for a particle to skip to the next period during an off-time. Assuming a single-particle drift velocity, the average number of off-times per drift-wait cycle is $(\langle T_{\mathrm{dw}} \rangle - t_{\mathrm{drift}})/\langle t \rangle_{\mathrm{off}} = 6.5$. In other words, the particle needs in average more than six off-times to reach the next period. Here, the on-times have been neglected, when the particles failed to reach the next period, because the corresponding distances to drift are very short.

5.6 Conclusions

In this chapter, we presented a thorough investigation how hydrodynamic interactions among Brownian paricles influence the performance of fluctuating thermal ratchets. In particular, we demonstrated that hydrodynamic interactions can significantly increase the particles' mean velocity. However, this is only possible when the particles change their ratchets states individually rather than simultaneously. Only then can drifting particles in the on-state act on neighboring particles in the off-state and add drift motion to their diffusional spreading. If in addition the transition rate from the on- to the off-state is localized at the minima of the ratchet potential, hydrodynamic interactions induce the formation of characteristic transient clusters. They travel with remarkably high velocities due to the reduction of the friction coeffcient per particle in such a linear cluster.

Localized transition rates in ratchet systems are discussed in the context of modeling molecular motors [60, 83, 84]. On the other hand, recent theoretical work based on an extended ASEP model addressed the traffic of kinesin proteins along microtubulin complexes and showed that hydrodynamic interactions increase the mean velocity of the motor proteins and even cause cytoplasmic streaming [51].

An early realization of a Brownian ratchet with colloidal particles uses a circling optical tweezers, the intensity of which is modulated in order to create the sawtooth potential [39]. Realizing, in particular, a localized transition rate would require some feedback mechanism that monitors the particle position and switches off the sawtooth potential when a single particle reaches a minimum. A different feedback algorithm for particles whose states are switched

collectively has already been demonstrated in the optical tweezer system [85]. It remains a challenge to experimentalists to construct the fluctuating ratchet where the particles change their states individually.

Bibliography

[1] A. Ajdari, *Force-free motion in an asymmetric environment: a simple model for structured objects*, Journal de Physique I **4** (1994), 1577.

[2] A. Ajdari, D. Mukamel, L. Peliti, and J. Prost, *Rectified motion induced by ac forces in periodic structures*, Journal de Physique I **4** (1994), 1551.

[3] A. Ajdari and J. Prost, *Drift induced by a spatially periodic potential of low symmetry - pulsed dielectrophoresis*, Comptes rendus de l'academie des sciences serie II **315** (1992), 1635.

[4] R. Astumian and M. Bier, *Fluctuation driven ratchets: Molecular motors*, Phys Rev Lett **72** (1994), 1766.

[5] R.H. Austin, N. Darnton, L.R. Huang, J.C. Sturm, O. Bakajin, and T.A.J. Duke, *Ratchets: the problems with boundary conditions in insulating fluids*, Applied Physics A Materials Science & Processing **75** (2002), 279, Springer-Verlag 2002.

[6] R. Bartussek, *Ratchets driven by colored gaussian noise*, Stochastic Dynamics **484** (1997), 68.

[7] J. Beeg, S. Klumpp, R. Dimova, R.S. Gracià, E. Unger, and R. Lipowsky, *Transport of beads by several kinesin motors*, Biophys J **94** (2008), 532.

[8] P.L. Bhatnagar, E.P. Gross, and M. Krook, *A model for collision processes in gases. i. small amplitude processes in charged and neutral one-component systems*, Physical Review **94** (1954), 511.

[9] M. Bier and R.D. Astumian, *Biasing brownian motion in different directions in a 3-state fluctuating potential and an application for the separation of small particles*, Phys Rev Lett **76** (1996), 4277.

[10] J. Brugués and J. Casademunt, *Self-organization and cooperativity of weakly coupled molecular motors under unequal loading*, Phys Rev Lett **102** (2009), 118104.

[11] J. Buceta, J.M. Parrondo, C. Van den Broeck, and F.J. de La Rubia, *Negative resistance and anomalous hysteresis in a collective molecular motor*, Physical Review E **61** (2000), 6287.

[12] R.E. Caflisch, C. Lim, J.H.C. Luke, and A.S. Sangani, *Periodic solutions for three sedimenting spheres*, Physics of Fluids **31** (1988), 3175.

[13] F.J. Cao, L. Dinis, and J.M.R. Parrondo, *Feedback control in a collective flashing ratchet*, Phys Rev Lett **93** (2004), 040603.

[14] Y. Chai, S. Klumpp, M.J.I. Müller, and R. Lipowsky, *Traffic by multiple species of molecular motors*, Physical review E **80** (2009), 041928.

[15] J.-F. Chauwin, A. Ajdari, and J. Prost, *Current reversal in asymmetric pumping*, Europhysics Letters (EPL) **32** (1995), 373.

[16] S. Chen and G.D. Doolen, *Lattice boltzmann method for fluid flows*, Annual Review of Fluid Mechanics **30** (1998), 329.

[17] Y.-D. Chen, *Asymmetric cycling and biased movement of brownian particles in fluctuating symmetric potentials*, Phys Rev Lett **79** (1997), 3117.

[18] Y.-D. Chen, B. Yan, and R. Miura, *Asymmetry and direction reversal in fluctuation-induced biased brownian motion*, Physical Review E **60** (1999), 3771.

[19] C.F. Chou, O. Bakajin, S.W. Turner, T.A.J. Duke, S.S. Chan, E.C. Cox, H. Craighead, and R.H. Austin, *Sorting by diffusion: an asymmetric obstacle course for continuous molecular separation*, Proc Natl Acad Sci USA **96** (1999), 13762.

[20] B. Cichocki and B.U. Felderhof, *Long-time tails in the solid-body motion of a sphere immersed in a suspension*, Physical Review E **62** (2000), 5383.

[21] E. Craig, M. Zuckermann, and H. Linke, *Reversal of motion induced by mechanical coupling in brownian motors*, American Physical Society (2006), 33009.

[22] J.C. Crocker, *Measurement of the hydrodynamic corrections to the brownian motion of two colloidal spheres*, The Journal of chemical physics **106** (1997), 2837.

[23] B. Cui, H. Diamant, and B. Lin, *Screened hydrodynamic interaction in a narrow channel*, Phys Rev Lett **89** (2002), 188302.

[24] T Czernik, J Kula, J uczka, and P Häautnggi, *Thermal ratchets driven by poissonian white shot noise*, Physical Review E **55** (1997), 4057.

[25] R.M. da Silva, C.C. de Souza Silva, and S. Coutinho, *Reversible transport of interacting brownian ratchets*, Physical review E **78** (2008), 061131.

[26] D. Dan, M.C. Mahato, and A.M. Jayannavar, *Multiple current reversals in forced inhomogeneous ratchets*, Physical Review E **63** (2001), 56307.

[27] J.A. Davis, D.W. Inglis, K.J. Morton, D.A. Lawrence, L.R. Huang, S.Y. Chou, J.C. Sturm, and R.H. Austin, *Deterministic hydrodynamics: taking blood apart*, Proc Natl Acad Sci USA **103** (2006), 14779.

[28] I. Derényi and A. Ajdari, *Collective transport of particles in a "flashing" periodic potential*, Physical Review E **54** (1996), 5.

[29] I. Derényi and R.D. Astumian, *ac separation of particles by biased brownian motion in a two-dimensional sieve*, Physical Review E **58** (1998), 7781.

[30] I. Derényi and T. Vicsek, *Cooperative transport of brownian particles*, Phys Rev Lett **75** (1995), 374.

[31] J.K.G. Dhont, *An introduction to dynamics of colloids*, Elsevier, Amsterdam, 1996.

[32] R.C. Dorf and R.H. Bishop, *Modern control systems*, Prentice Hall, Englewood Cliffs, NJ, 2008.

[33] K.D. Dorfman and H. Brenner, *"vector chromatography": Modeling micropatterned separation devices*, J Colloid Interface Sci **238** (2001), 390.

[34] K.D. Dorfman and H. Brenner, *Separation mechanisms underlying vector chromatography in microlithographic arrays*, Physical review E **65** (2002), 052103.

[35] E.R. Dufresne, T.M. Squires, M.P. Brenner, and D.G. Grier, *Hydrodynamic coupling of two brownian spheres to a planar surface*, Phys Rev Lett **85** (2000), 3317.

[36] T.A.J. Duke and R.H. Austin, *Microfabricated sieve for the continuous sorting of macromolecules*, Phys Rev Lett **80** (1998), 1552.

[37] D.L. Ermak and J.A. McCammon, *Brownian dynamics with hydrodynamic interactions*, The Journal of chemical physics **69** (1978), 1352.

[38] D. Ertaş, *Lateral separation of macromolecules and polyelectrolytes in microlithographic arrays*, Phys Rev Lett **80** (1998), 1548.

[39] L.P. Faucheux, L.S. Bourdieu, P.D. Kaplan, and A.J. Libchaber, *Optical thermal ratchet*, Phys Rev Lett **74** (1995), 1504.

[40] M. Feito, J.P. Baltanás, and F.J. Cao, *Rocking feedback-controlled ratchets*, Physical review E **80** (2009), 031128.

[41] M. Feito and F.J. Cao, *Threshold feedback control for a collective flashing ratchet: threshold dependence*, Physical review E **74** (2006), 041109.

[42] R.P. Feynman, R.B. Leighton, and M. Sands, *The feynman lectures on physics*, vol. 1, Addison-Wesley, Reading, MA, 1966.

[43] J.A. Fornés, *Hydrodynamic interactions induce movement against an external load in a ratchet dimer brownian motor*, J Colloid Interface Sci **341** (2010), 376.

[44] M. Galassi, *GNU scientific library*, http://www.gnu.org/software/gsl/.

[45] R.E. Goldstein, M. Polin, and I. Tuval, *Noise and synchronization in pairs of beating eukaryotic flagella*, Phys Rev Lett **103** (2009), 168103.

[46] D.G. Grier, *A revolution in optical manipulation*, Nature **424** (2003), 810.

[47] B.A. Grzybowski, H.A. Stone, and G.M. Whitesides, *Dynamic self-assembly of magnetized, millimetre-sized objects rotating at a liquid-air interface*, Nature **405** (2000), 1033.

[48] P. Hänggi and F. Marchesoni, *Artificial brownian motors: Controlling transport on the nanoscale*, Reviews of Modern Physics **81** (2009), 387.

[49] J. Happel and H. Brenner, *Low Reynolds number hydrodynamics*, Noordhoff, Leyden, 1973.

[50] S. Henderson, S. Mitchell, and P. Bartlett, *Propagation of hydrodynamic interactions in colloidal suspensions*, Phys Rev Lett **88** (2002), 088302.

[51] D. Houtman, I. Pagonabarraga, C.P. Lowe, A. Esseling-Ozdoba, A.M.C. Emons, and E. Eiser, *Hydrodynamic flow caused by active transport along cytoskeletal elements*, Europhysics Letters **78** (2007), 18001.

[52] L.R. Huang, E.C. Cox, R.H. Austin, and J.C. Sturm, *Tilted brownian ratchet for dna analysis*, Anal Chem **75** (2003), 6963.

[53] L.R. Huang, E.C. Cox, R.H. Austin, and J.C. Sturm, *Continuous particle separation through deterministic lateral displacement*, Science **304** (2004), 987.

[54] L.R. Huang, P. Silberzan, J.O. Tegenfeldt, E.C. Cox, J.C. Sturm, R.H. Austin, and H. Craighead, *Role of molecular size in ratchet fractionation*, Phys Rev Lett **89** (2002), 178301.

[55] A. Igarashi, S. Tsukamoto, and H. Goko, *Transport properties and efficiency of elastically coupled brownian motors*, Physical review E **64** (2001), 051908.

[56] D.W. Inglis, *Efficient microfluidic particle separation arrays*, Applied Physics Letters **94** (2009), 013510.

[57] D.W. Inglis, J.A. Davis, R.H. Austin, and J.C. Sturm, *Critical particle size for fractionation by deterministic lateral displacement*, Lab Chip **6** (2006), 655.

[58] T. Ishikawa and T.J. Pedley, *Coherent structures in monolayers of swimming particles*, Phys Rev Lett **100** (2008), 088103.

[59] I.M. Jánosi, T. Tél, D.E. Wolf, and J.A.C. Gallas, *Chaotic particle dynamics in viscous flows: The three-particle stokeslet problem*, Physical Review E **56** (1997), 2858.

[60] F. Jülicher, A. Ajdari, and J. Prost, *Modeling molecular motors*, Reviews of Modern Physics **69** (1997), 1269.

[61] F. Jülicher and J. Prost, *Cooperative molecular motors*, Phys Rev Lett **75** (1995), 2618.

[62] P. Jung, J. Kissner, and P. Hänggi, *Regular and chaotic transport in asymmetric periodic potentials: Inertia ratchets*, Phys Rev Lett **76** (1996), 3436.

[63] M. Kenward and G. W. Slater, *Polymer deformation in brownian ratchets: theory and molecular dynamics simulations*, Physical review E **78** (2008), 051806.

[64] C. Kettner, P. Reimann, P. Hänggi, and F. Müller, *Drift ratchet*, Physical Review E **61** (2000), 312.

[65] M.J. Kim and T.R. Powers, *Hydrodynamic interactions between rotating helices*, Physical review E **69** (2004), 061910.

[66] S. Kim and S.J. Karrila, *Microhydrodynamics: principles and selected applications*, Butterworth-Heinemann, Boston, 1991.

[67] S.H. Kim and H. Pitsch, *A generalized periodic boundary condition for lattice boltzmann method simulation of a pressure driven flow in a periodic geometry*, Physics of Fluids **19** (2007), 8101.

[68] S. Klumpp and R. Lipowsky, *Asymmetric simple exclusion processes with diffusive bottlenecks*, Physical review E **70** (2004), 066104.

[69] S. Klumpp, A. Mielke, and C. Wald, *Noise-induced transport of two coupled particles*, Physical review E **63** (2001), 031914.

[70] S. Klumpp, T.M. Nieuwenhuizen, and R. Lipowsky, *Self-organized density patterns of molecular motors in arrays of cytoskeletal filaments*, Biophys J **88** (2005), 3118–32.

[71] M. Kollmann, *Single-file diffusion of atomic and colloidal systems: Asymptotic laws*, Phys Rev Lett **90** (2003), 180602.

[72] M. Kostur and J. Luczka, *Multiple current reversal in brownian ratchets*, Physical Review E **63** (2001), 21101.

[73] J. Kotar, M. Leoni, B. Bassetti, M.C. Lagomarsino, and P. Cicuta, *Hydrodynamic synchronization of colloidal oscillators*, Proc Natl Acad Sci USA **107** (2010), 7669.

[74] T. Krüger, F. Varnik, and D. Raabe, *Shear stress in lattice boltzmann simulations*, Physical Review E **79** (2009), 46704.

[75] J. Kula, *Brownian transport controlled by dichotomic and thermal fluctuations*, Chemical Physics **235** (1998), 27.

[76] M.C. Lagomarsino, P.Jona, and B. Bassetti, *Metachronal waves for deterministic switching two-state oscillators with hydrodynamic interaction*, Physical Review E **68** (2003), 21908.

[77] L.D. Landau and E.M. Lifshitz, *Fluid mechanics*, Pergamon Press, London, 1959.

[78] P. Lavallée, J.P. Boon, and A. Noullez, *Boundaries in lattice gas flows*, Physica D: Nonlinear Phenomena **47** (1991), 233.

[79] S.-H. Lee and D.G. Grier, *One-dimensional optical thermal ratchets*, Journal of Physics: Condensed Matter **17** (2005), 3685.

[80] S.-H. Lee, K. Ladavac, M. Polin, and D.G. Grier, *Observation of flux reversal in a symmetric optical thermal ratchet*, Phys Rev Lett **94** (2005), 110601.

[81] P. Lenz, J.-F. Joanny, F. Jülicher, and J. Prost, *Membranes with rotating motors*, Phys Rev Lett **91** (2003), 108104.

[82] Z. Li and G. Drazer, *Separation of suspended particles by arrays of obstacles in microfluidic devices*, Phys Rev Lett **98** (2007), 050602.

[83] R. Lipowsky, *Universal aspects of the chemomechanical coupling for molecular motors*, Phys Rev Lett **85** (2000), 4401.

[84] R. Lipowsky and T. Harms, *Molecular motors and nonuniform ratchets*, Eur Biophys J **29** (2000), 542.

[85] B.J. Lopez, N.J. Kuwada, E.M. Craig, B.R. Long, and H. Linke, *Realization of a feedback controlled flashing ratchet*, Phys Rev Lett **101** (2008), 220601.

[86] J Luczka, R Bartussek, and P Hänggi, *White-noise-induced transport in periodic structures*, Europhysics Letters (EPL) **31** (1995), 431.

[87] C. Lutz, M. Reichert, H. Stark, and C. Bechinger, *Surmounting barriers: The benefit of hydrodynamic interactions*, Europhysics Letters **74** (2006), 719.

[88] M.O. Magnasco, *Forced thermal ratchets*, Phys Rev Lett **71** (1993), 1477.

[89] S.E. Mangioni, R.R. Deza, and H. S. Wio, *Transition from anomalous to normal hysteresis in a system of coupled brownian motors: A mean-field approach*, Physical Review E **63** (2001), 41115.

[90] S. Martin, M. Reichert, H. Stark, and T. Gisler, *Direct observation of hydrodynamic rotation-translation coupling between two colloidal spheres*, Phys Rev Lett **97** (2006), 248301.

[91] J. Mateos, *Chaotic transport and current reversal in deterministic ratchets*, Phys Rev Lett **84** (2000), 258.

[92] S. Matthias and F. Müller, *Asymmetric pores in a silicon membrane acting as massively parallel brownian ratchets*, Nature **424** (2003), 53.

[93] P. Mazur, *On the motion and brownian motion of n spheres in a viscous fluid*, Physica A **110** (1982), 128.

[94] J.-C. Meiners and S.R. Quake, *Direct measurement of hydrodynamic cross correlations between two particles in an external potential*, Phys Rev Lett **82** (1999), 2211.

[95] M.J.I. Müller, S. Klumpp, and R. Lipowsky, *Tug-of-war as a cooperative mechanism for bidirectional cargo transport by molecular motors*, Proc Natl Acad Sci USA **105** (2008), 4609.

[96] G. Nägele, *On the dynamics and structure of charge-stabilized suspensions*, Physics Reports **272** (1996), 215.

[97] T. Niedermayer, B. Eckhardt, and P. Lenz, *Synchronization, phase locking, and metachronal wave formation in ciliary chains*, Chaos **18** (2008), 7128.

[98] N. Pamme, *Continuous flow separations in microfluidic devices*, Lab Chip **7** (2007), 1644.

[99] C.M. Pooley, G.P. Alexander, and J.M. Yeomans, *Hydrodynamic interaction between two swimmers at low reynolds number*, Phys Rev Lett **99** (2007), no. 22, 228103.

[100] W.H. Press, B.P. Flannery, S.A. Teukolsky, and W.T. Vetterling, *Numerical recipes in C: the art of scientific computing*, Cambridge University Press, Cambridge, 1992.

[101] J. Prost, J.-F. Chauwin, L. Peliti, and A. Ajdari, *Asymmetric pumping of particles*, Phys Rev Lett **72** (1994), 2652.

[102] Y.-H. Qian and Y. Zhou, *Higher-order dynamics in lattice-based models using the chapman-enskog method*, Physical Review E **61** (2000), 2103.

[103] M. Reichert and H. Stark, *Circling particles and drafting in optical vortices*, Journal of Physics: Condensed Matter **16** (2004), 4085.

[104] M. Reichert and H. Stark, *Hydrodynamic coupling of two rotating spheres trapped in harmonic potentials*, Physical Review E **69** (2004), 31407.

[105] M. Reichert and H. Stark, *Synchronization of rotating helices by hydrodynamic interactions*, Eur Phys J E Soft Matter **17** (2005), 493.

[106] P. Reimann, *Brownian motors: noisy transport far from equilibrium*, Physics Reports **361** (2002), 57.

[107] P. Reimann and M. Evstigneev, *Pulsating potential ratchet*, Europhysics Letters **78** (2007), 50004.

[108] P. Reimann, R. Kawai, C. Van den Broeck, and P. Hänggi, *Coupled brownian motors: Anomalous hysteresis and zero-bias negative conductance*, Europhysics Letters **45** (1999), 545.

[109] J. Rousselet, L. Salome, A. Ajdari, and J. Prost, *Directional motion of brownian particles induced by a periodic asymmetric potential*, Nature **370** (1994), 446.

[110] F. Schwabl, *Statistical mechanics*, Springer, Berlin, 2006.

[111] I.K. Snook, K.M. Briggs, and E.R. Smith, *Hydrodynamic interactions and some new periodic structures in three particle sediments*, Physica A **240** (1997), 547.

[112] S. Succi, *The lattice boltzmann equation for fluid dynamics and beyond*, Oxford University Press, New York, 2001.

[113] N. Uchida and R. Golestanian, *Synchronization and collective dynamics in a carpet of microfluidic rotors*, Phys Rev Lett **104** (2010), 178103.

[114] J.R.C. van der Maarel, *Introduction to biopolymer physics*, World Scientific, Singapore, 2008.

[115] A. van Oudenaarden and S.G. Boxer, *Brownian ratchets: molecular separations in lipid bilayers supported on patterned arrays*, Science **285** (1999), 1046.

[116] A. Vilfan and F. Jülicher, *Hydrodynamic flow patterns and synchronization of beating cilia*, Phys Rev Lett **96** (2006), 058102.

[117] M.B. Wan, C.J.O. Reichhardt, Z. Nussinov, and C. Reichhardt, *Rectification of swimming bacteria and self-driven particle systems by arrays of asymmetric barriers*, Phys Rev Lett **101** (2008), 18102.

[118] Z. Wang, M. Feng, W. Zheng, and D. Fan, *Kinesin is an evolutionarily fine-tuned molecular ratchet-and-pawl device of decisively locked direction*, Biophys J **93** (2007), 3363.

[119] Q. Wei, C. Bechinger, and P. Leiderer, *Single-file diffusion of colloids in one-dimensional channels*, Science **287** (2000), 625.

[120] J. Zhang and D.Y. Kwok, *Pressure boundary condition of the lattice boltzmann method for fully developed periodic flows*, Physical review E **73** (2006), 047702.